Dissertation zum Erlangen des akademischen Grades *Doktor der Naturwissenschaften* der Fakultät für Physik der Ludwig-Maximilians-Universität München

Cosmological Hydrodynamics: Thermal Conduction and Cosmic Rays

vorgelegt von Martin Jubelgas aus München

München, 19.12.2007

Dissertation der Fakultät für Physik der
Ludwig-Maximilians-Universität München

Martin Jubelgas:
Cosmological Hydrodynamics: Thermal Conduction and Cosmic Rays
Dissertation der Fakultät für Physik der Ludwig-Maximilians Universität München
ausgeführt am Max-Planck-Institut für Astrophysik

Vorsitzender:	Prof. Dr. Erwin Frey
1. Gutachter:	Prof. Dr. Simon White
2. Gutachter:	Prof. Dr. Andreas Burkert
Weiterer Prüfer:	Prof. Dr. Roland Kersting
Tag der mündlichen Prüfung:	19. März 2007

Contents

In the space of one hundred and seventy-six years the Mississippi has shortened itself two hundred and forty-two miles. Therefore ... in the Old Silurian Period the Mississippi River was upward of one million three hundred thousand miles long ... seven hundred and forty-two years from now the Mississippi will be only a mile and three-quarters long. ... There is something fascinating about science. One gets such wholesome returns of conjecture out of such a trifling investment of fact.

Mark Twain

1 Introduction

While working on this thesis, I was often asked: "Cosmology? What is it good for?". Perhaps understandably, it was often people focused on practical applications of science that asked the question. For me, however, this was never a concern, because personally I consider cosmology to be one of the most fascinating fields of physics. As it deals with the beginning of the universe and with the forces that drove cosmic evolution from the earliest times to what we observe today, cosmology addresses fundamental human questions of "how did it all start" and "how will it all end". Cosmology tries to give reliable scientific answers to questions that have always inspired mysticism, religion and the arts. Even in modern times, astronomical questions are a strong cultural driver, apparent by the widespread belief in the foretellings of astrology. Given the role of ancient mysticism revolving around the sky and the celestial objects, astronomy and cosmology might be considered the oldest branches of science, yet still offer some of its greatest puzzles. The beauty of the sky and the of the visible planets, stars and remote galaxies, observed by the naked eye or telescopes, has always amazed people and spurred their imagination. Touching people emotionally like this, it is not surprising that there is a strong interest in this discipline of science in spite of a lack of direct economical motivations.

Astrophysics is a field of science that draws on expertise from many different branches of physics, including classic and comparatively well-understood processes like gravitation and basic hydrodynamics, as well as modern fields of research like relativistic hydrodynamics and high-energy particle physics. This diversity results in a uniquely comprehensive synopsis of different physical effects and their combined action in an often highly complex network of interactions, typically in environments and physical conditions that span many orders of magnitudes in physical length-, density- or temperature-scales. The universe presents itself as a laboratory that allows us to study processes in ranges of physical parameters that could hardly ever be generated on earth. Also, the sheer size of the universe gives us the chance to

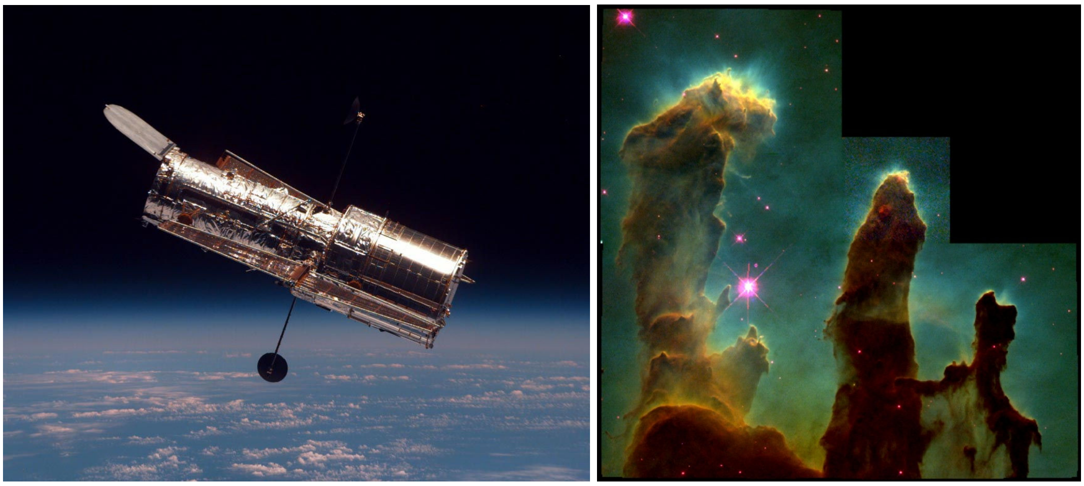

Figure 1.1.: The deployment of high-resolution instruments like the Space Telescope (HST, left panel) in space has made it possible to observe an unprecedented level of detail in distant objects, e.g. the Eagle Nebula, a young open cluster in the Serpens Cauda constellation. (Souce: NASA)

study rare events that occur among the large number of individual objects in this huge volume. Astronomical observations also play an important role for particle physics, as they can be used to constrain some of the fundamental parameters in high-energy physics, for example the masses of neutrinos.

What can be percieved on one hand as a blessing for astrophysics, can, on the other hand be called one of its biggest handicaps. Since these systems are far out of human reach and cannot be analyed in laboratory conditions, the only means of studying most of the objects of interest in astrophysics is to observe their optical and other electromagnetic radiation imprinted on the sky. The typically extremely faint flux data from such objects can only be detected with sophisticated telescope instrumentation and needs to be processed through many steps to yield the desired data, which is then subject to the limitations and errors of the measuring procedure. Angular resolution, detector sensitivity and atmospheric distortions, the so called "seeing", set severe limits on the size and faintness of objects that can be resolved, and thus on the distance of objects we can observe in detail. Despite these limitations, gradually more sophisticated models of the universe have been developed.

The second half of the last century has seen cosmology advancing at a tremendous rate that has changed its face completely. Space flight has the deployment of telescopes outside Earth's atmosphere possible, which gather data in ever higher resolution and sensitivity, but also opening up new ways of observations in the infrared, X-ray and gamma-ray regimes that were formerly blocked from observation by Earth's atmosphere. High-performance computers help researchers distill the collected vast amounts of data into useful information. These computers have also become increasingly powerful as a tool to calculate the non-linear evolution of astrophysical objects. Such simulations have in fact become indispensable in modern cosmological research, and will be a focal point of the research presented in this thesis.

The real-time processing abilities of modern computers have also allowed the recent development of telescopes that use adaptive optics to eliminate the atmospheric disturbances (the afore mentioned *seeing*) and improve the sharpness and resolution of ground-based telescopes, enabling them to compete even with the Hubble Space Telescope (HST). Improved means of communications and information exchange via the internet have brought the research community closer together than ever before. This facilitates international collaboration and accelerates the pace of global scientific advancement. Cosmology is a blooming science these days, where a lot of exciting progress is taking place. Computer technology is an important driver of this progress, playing a key role in modern astronomical observations, in daily scientific work, as well as in theoretical astrophysics, where direct computer simulations allow ever more detailed research. As a result, computational cosmology can now be viewed as a third pillar of astrophysics, shoulder to shoulder with the traditional fields of pure observation and theory.

In the rest of this introduction to my thesis, I will briefly discuss a few basic aspects of the historic development of cosmology and of its modern state. This is only meant to set the stage for the later work, and to give it some context in the broader picture of astrophysics. Note that a comprehensive introduction to cosmology is beyond the scope of this thesis, but can be found in a number of excellent textbooks on the subject (e.g. Peacock 1999).

1.1. (How) did it all start?

The very concept of a "start" of the universe has not been around at all times. The antique cosmologies (which admittedly were a lot closer to mythology still) mostly considered the world to be either static, or at least cyclic on small scales. World views at these times mostly considered Earth to be the center of the universe and philosophers like the Greek Claudius Ptolemy developed complex models to explain the observed motion of the sun and the observed trajectories of the planets on the sky. Although theories suggesting a heliocentric system had existed since the 4th century BC, they did not overcome the resistance based on human self-understanding, which was still very much influenced by mythic and religious understandings.

Even when in the 16th century, after a long phase of suppressed research in the dark ages (the ‘dark ages’ in European history, as opposed to the ‘cosmic dark ages’ before the formation of the first luminous objects), Nicolaus Kopernicus’ writings introduced a revolutionary theory that got rid of Earth’s special status in our solar system, the idea of a static and eternal universe was still hardly questioned.

Early in the 20th century, Albert Einstein formulated his general theory of relativity in the firm belief of a static universe. When he realized that his theory did, in fact, not allow a static solution, he introduced a cosmological expansion constant Λ into his work, which could prevent a collapse of a static universe under the influence of gravitation. It is a remarkably funny and ironic twist of scientific history that although Einstein himself labeled this cosmological constant his "biggest blunder" for a while, it became an important part of modern cosmology after the accelerated expansion of the universe was discovered.

The foundation for the “Big Bang” theory that is widely accepted nowadays was laid by the observations of Hubble Hubble (1929) and Lemaitre (1930) who discovered that distant “nebulae” (galaxies), were receding from the Milky Way, with a larger velocity for larger distance. This served as proof for an ongoing expansion of the universe, and gave rise to the idea of a beginning of the universe in the "explosion" of a "primeval atom", which would later be referred to as the Big Bang. Hubble found that the speed of recession of distant objects appears to be proportional to their distance. This relation,

$$\boldsymbol{v} = H\boldsymbol{r} = 100\,h\,\frac{\mathrm{km}}{\mathrm{s\ Mpc}}\boldsymbol{r} \tag{1.1}$$

defines the Hubble constant H, or its dimensionless counterpart h. The Hubble constant is of fundamental importance to modern cosmology, for it indicates the current expansion rate of the universe. The age of the universe can roughly be estimated to be of order $1/H$, one so-called "Hubble time".

The expansion of the universe can be understood physically in terms of solutions of Einstein’s field equations under the assumption of an isotropic and homogeneous universe. This yields the Friedman equations, which describe the expansion of space as a function of time, and give rise to different classes of basic cosmological models. In these models, the ultimate fate of the universe that start out with a Big Bang strongly depends on the amount of matter contained in the universe. The gravitational attraction of matter counteracts the global expansion of the universe and slows it down. The mean density required to bring the expansion to a halt asymptotically is called the *critical density* ρ_{crit}. For a long time, one of the greatest questions of cosmology was whether the real mean density would be lower, equal to or perhaps even larger than this critical density. Correspondingly, this was interpreted as implying that the universe would expand forever, come to an asymptotic halt, or eventually contract again and die in a “big crunch”. One of the great surprises of modern cosmology was the discovery that besides gravitating matter, there appears to be also some sort of “dark energy field” which *accelerates* the expansion of the universe. Whether the influence posed by gravity or the influence posed by dark energy is larger, can change with time, complicating possible expansion histories of the universe.

Most of modern cosmological surveys presently agree that the matter density and the dark energy density together just reach the critical density, which gives the universe a "flat" space-time geometry, i.e. the curvature vanishes and time-slices are like Euclidian space. In numbers, the energy density of the universe is presently made up by $\sim$ 4% normal matter (atoms like hydrogen or helium), $\sim$ 26% dark matter (probably an unidentified elementary particle), while the remaining $\sim$ 70% are due to the mysterious dark energy field (Seljak et al. 2005, Spergel et al. 2006). While cosmology still cannot offer answers to the question what the dark matter or dark energy really is, it convincingly demonstrates that this mysterious entities must be there.

1.2. The early universe and the cosmic microwave background

In the early universe after the "Big Bang", temperatures were extremely high. Combined with the very high densities, the photon opacity of the primordial, highly ionized cosmic matter was so high that matter

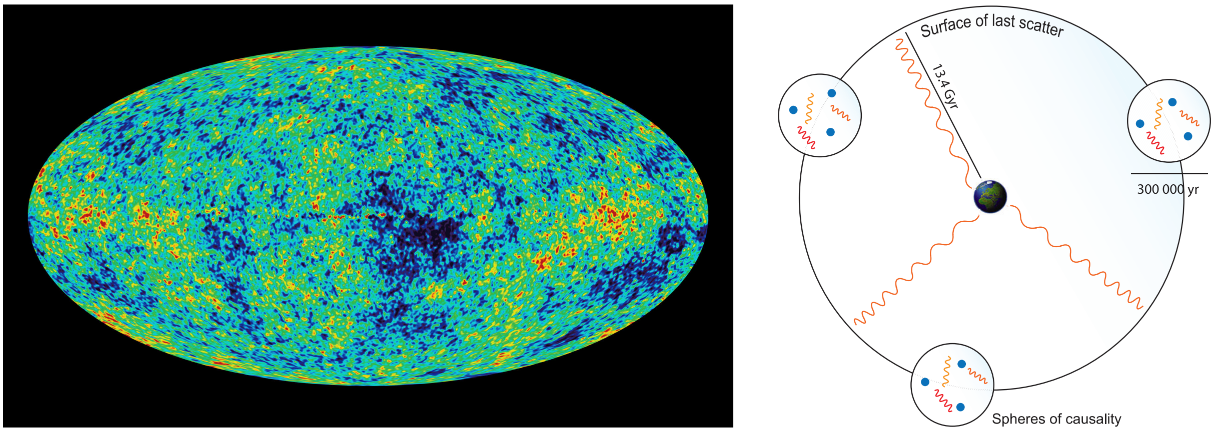

Figure 1.2.: The cosmic microwave background shows remarkably little variation over the entire sky (left panel: map of the CMB taken by the WMAP satellite; Souce: NASA). It is remarkable that the variations on the CMB even on large scales are extremely small. The distances between different parts of the last scattering surface are are larger by far than the maximum volume that would allow allow for a causal contact in a "normal" explosion scenario (right panel).

and radiation were tightly coupled. It took almost 400′000 years for temperatures to drop sufficiently so that protons and helium nuclei could finally capture electrons and form atoms. The formerly opaque plasma became neutral and transparent to radiation; photons could traverse space freely, carrying information about their last scattering event in the dense primordial plasma. The radiation cooled down as the universe expanded, and is still present today. It now forms the Cosmic Microwave Background that we can observe as a thermal relic of the Big Bang at a temperature of 2.275 K.

This kind of afterglow of the Big Bang in the form of low-temperature radiation had been first predicted in the 1940's by Gamow, Alpher and Hermann (Alpher et al. 1948, Alpher & Herman 1953), in their research about the early universe. Experimental proof of the cosmic radiation background was provided in 1964. Arno Penzias and Robert Woodrow Wilson constructed a horn antenna, to detect radio waves bounced off echo balloons. After many futile efforts to eliminate instrumental noise in their antenna, they still encountered residual noise of an unknown origin. This "noise" was not related to any special celestial object, but seemed evenly spread all over the sky. Lacking any spatial structure (which was due to the relative insensitivity of their instrument, from today's point of view), they together with Dicke and Peebles eventually concluded that the radiation must originate extra-galactically. They were thus able to bring together theory and experiment and explain this background noise as being the afterglow of the Big Bang.

Due to atmospheric shielding, well resolved Earth-based observations of the cosmic microwave background (CMB) proved to be difficult, so subsequent measurements of the CMB were mostly performed with balloon-borne instruments, until in 1989, NASA deployed COBE (Cosmic Background Explorer), the first satellite to survey the CMB's full-sky structure. During its seven years of operation, it gathered data on the cosmic background. This data revealed for the first time fluctuations in the radio-radiation over the whole sky. Although tiny, typically less than 100 μK, these fluctuations proved to be invaluable for cosmology. They are an imprint of density fluctuations at the time of last scattering, which are the seed perturbations for structure formation in the almost uniform state of the universe more than 10 Gyr ago.

It is remarkable that, despite of the immense volume probed with the CMB radiation, fluctuations on large scales are as small as observed. Assuming a "classical" expansion model where the evolution of the expansion rate depends only on the mean mass density of the universe, some of the different volume elements that emit CMB radiation cannot have been in causal contact, yet their temperature is remarkably similar. Therefore, seeing a nearly exact match of the emission levels of the different patches on the sky is hard to explain in a simple Friedman model for the expansion of the universe.

This so-called "horizon problem" is one of the observational indications that inspired ideas that led to the theory of *Inflation*. It assumes that at a very early point in time, roughly at 10^{-35} seconds after the Big Bang, there was an epoch during which the universe expanded exponentially by many orders of magnitude within a short time. In this way, all points of the observable universe have in fact been causally connected in the very beginning, but were brought out of casual contact by inflation later on."Blowing up" space like the surface of a balloon that is inflated also results in a suppression of perturbations in the growing universe, and helps explaining the lack of sizable curvature of space. Without the process of inflation, it is hard to argue why Ω, the ratio of the total energy density to the critical energy density, equals unity with a deviation of only 10^{-15} in the early universe, which is required to reproduce the universe as we know it today.

1.3. Structure formation

The small density fluctuations that left their imprint in the CMB seeded the cosmological structure we see today. The recent high-resolution precision measurements of the CMB power spectrum, obtained for example by the WMAP satellite, have given an accurate account of this feeble spatial structure in the very early universe, and at the same time supported the overall cosmological paradigm. These fluctuations are also the starting point for attempts to model the processes that lead to today's observed cosmic structure, using either analytic or numerical methods. The CMB fluctuations provide the initial conditions for structure formation.

The observed fluctuations in the CMB temperature maps are very small compared to the mean temperature, and correspond to equally small seed perturbations in the cosmic density field. Commonly, the density fluctuations are described in terms of the so-called *overdensity* δ, defined as

$$1 + \delta(\boldsymbol{x}) = \frac{\rho(\boldsymbol{x})}{\langle\rho\rangle}. \tag{1.2}$$

Adopting this notation, the small fluctuation regime is described by $\delta \ll 1$. By applying perturbation theory, growth of structure can be treated by expanding the evolutionary equations in powers of δ, but in practice it is hard to do much better than linear theory where only terms proportional to δ are kept. The great strength of direct simulation approaches to solving the evolutionary equations is that they do not face this restriction. Instead, they can be advanced well into the highly non-linear regime of gravitational clustering.

Despite the overall rapid expansion of space at early times, it can be shown that small overdensities grow with time in the matter-dominated regime and become ever more pronounced. For $\Omega \simeq 1$, it can be shown that $\delta(t)$ scales as $\delta(t) \propto t^{2/3}$. At later times, the evolution becomes more complicated when the density contrast grows to a size of order unity and the assumptions of linear perturbation theory become invalid.

While an initial perturbation grows in amplitude in the linear phase, is is still stretched in spatial extent by the expansion of space. However, after passing though a certain overdensity threshold, the self-gravity of the matter perturbation has reached a high enough level to halt further expansion of the perturbation, decoupling itself from the general expansion of the background. It no longer grows along in physical size with the universal expansion, but instead "turns around" and collapses onto itself. These decoupled overdensities do not collapse into singularities, however. Instead, the gravitational energy of the infalling matter, which is dominated in mass by collisionless dark matter, is released into a random motion of particles. The dark matter virializes and forms a long-lived quasi-equilibrium system (White & Narayan 1987), which is commonly called a "halo". The collapsed structure of a halo can increase its mass by merging with other collapsed overdensities, or by accreting diffuse matter.

The non-linear formation of virialized halos can only be treated analytically under quite restrictive assumptions, for example that of spherical symmetry. However, the cosmic perturbation spectrum has a complex geometry and produces halos that are highly non-spherical, and grow hierarchically, undergoing many merger events. This complexity can be accurately described only by direct numerical simulations, which have therefore become a highly valuable tool for investigating cosmic structure formation in this non-linear regime. To use this technique, a matter distribution is represented by a discrete set of mass elements. For simulations of the gas component, a volume discretization, i.e. of a grid, can be used. The numerical model can then be evolved forward in time by integrating the equations of self-gravity and hydrodynamic interactions. With the immense increase in the performance of computers and numerical algorithms in recent years, cosmologists were able to perform simulations of structure formation in ever greater detail, such that forming structures and galaxies can be studied in computer models with ever higher fidelity to the real physics.

Most simulations of cosmic large-scale structure are restricted to gravitational dynamics of the dark matter alone, which makes up more than 85% of the mass content of our universe. While the true nature of this dominant contribution to the matter content is still unknown, the success of the cold dark matter model suggests that dark matter does not show other sizable interactions than gravity in the low-redshift universe, i.e. the dark matter particles are at most weakly interacting. Processes like dark matter annihilation might exist (e.g. Rudaz & Stecker 1988, Ullio et al. 2002, Stoehr et al. 2003), but appear to be weak enough to make the gravity-only model a good approximation. Gravitation, being a long-range interaction, is numerically expensive to evaluate, but its simple, scale-independent nature make it generally a very well-behaved and straight-forward process to simulate. Simulations of dark matter models hence do not require a large number of additional assumptions to be made and are arguably the best understood element in the chain of processes that explain structure formation. While dark matter-only

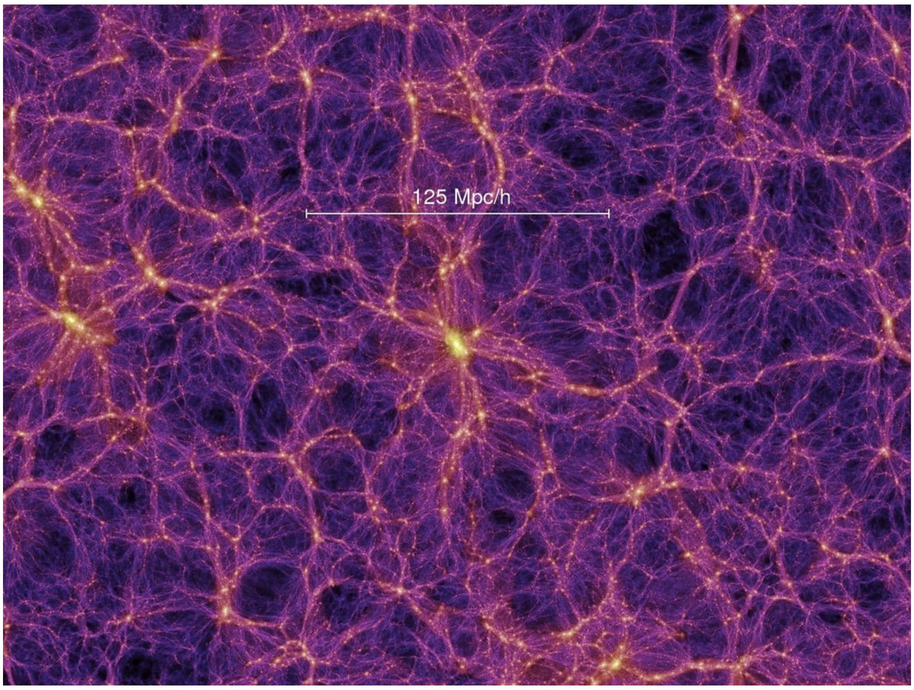

Figure 1.3.: Zoom into a small region of the volume evaluated in the Millennium Simulation (Springel et al. 2005b). The total simulation volume spans over several billion parsec along each side of a periodic box populated with more than 10^{10} simulation particles to represent individual mass elements during the structure formation process. At 350'000 CPU hours on a Power4 regatta supercomputer, it is the largest cosmological simulation performed so far.

simulations certainly do not give a complete picture of the physics that govern cosmic structure formation, they nevertheless are very successful when it comes to reproducing basic properties of galaxies and large-scale structures. The abundance of halos of given mass and their spatial correlations can be extracted from simulations very accurately, and there is broad agreement with corresponding observational inferences under plausible assumptions for the distribution of galaxies in these halos. What remains to be demonstrated is whether the same model is also able to account in detail for all the observed properties of galaxies once the baryons are included as well.

1.4. Galaxy formation

In order to understand the formation of the stellar populations of galaxies and clusters of galaxies in detail, dark-matter-only simulations are not sufficient. The baryonic matter that is responsible for producing the luminous objects that we see interacts in a much more complex manner than the collisionless dark matter. Unlike dark matter, the effective cross-section of gas particles for particle-particle interactions is large, leading to the collisional thermalization of particle momenta and the macroscopic behavior of the baryons as a gas, which can be described with thermodynamic properties like temperature and pressure.

Gas fluid elements cannot move freely through each other like it is assumed for dark matter, but rather produce shock fronts in colliding flows where kinetic energy of the bulk motion is transformed into unordered microscopic thermal motion. The virialization of the gas during the gravitational collapse of a forming halo proceeds through such shocks, resulting in a hydrodynamic pressure support against further gravitational contraction. Note also that the thermodynamic gas pressure is isotropic, but the support of the dark matter through random motions can also be anisotropic.

In order to collapse further into structures of much higher density than is reached in virialized dark matter halos, the baryonic gas must first lose part of its pressure support gained during halo formation. The most important process to do so is radiative cooling, either as Bremsstrahlung from free electrons or as line emission from atoms. The efficiency of the radiative dissipation strongly depends on gas temperature and density, and becomes quite inefficient for temperatures below 10^4 K, where the gas becomes neutral. Cooling below this temperature can only be mediated by much slower molecular cooling processes.

On the other hand, the gas is also prone to heating by photon absorption. When the first generations of massive stars and quasars formed, they emitted hard UV radiation that was eventually able to re-ionize the neutral gas that had cooled down after the Big Bang to a few tens on the Kelvin scale. It is still unclear what sources exactly caused this re-ionization, but we know that it must have happened, as the present universe is highly ionized and filled with a bath of ionizing UV radiation (e.g. Ciardi & Ferrara 2005,and references therein). For an efficient condensation within a host dark matter halo, the energetic input by this radiation must be overcome by a stronger thermal cooling. Effectively, in very small halos with virial temperatures below a few times 10^4 K, the gas cannot lose its pressure support anymore due to this UV heating and the low cooling rates in this regime. Only in larger halos, it can cool and gather in the halo center to form a rotationally supported disk, as a result of the conservation of angular momentum in the gas created by tidal torquing during halo formation. Within the disk, the gas can then further fragment into dense molecular clouds, where it eventually reaches the densities required to trigger the formation of stars.

The exact physical conditions in these cradles of star formation, where the condensation of matter under its own weight leads to densities that cause the ignition of fusion-burning in the hearts of protostars, are the result of a complex interplay of different processes, far from being understood in detail. Our knowledge concerning the efficiency of the process is particularly poor. What we however know is that there appears to be some "feedback mechanism" that regulates star formation so that in most cases not all of the gas in the clouds turns into stars all at once. Most likely, a large part of this feedback is driven by the radiation emitted by newly formed stars, and the energetic shocks powered by the supernova explosions of massive stars in their final phases of evolution. Important channels of feedback could also arise from magnetic fields or relativistic particle components, so-called cosmic rays. As a result of feedback, the interstellar medium is heated, condensing cold clouds are evaporated and cooling is counteracted. The cumulative effects of a multitude of supernovae could also lead to the ejection of interstellar matter from protogalactic disks in the form of a wind. Indeed, in many observed systems, large amounts of gas are thrown out of the dense gas disk and into the halo, apparently carrying a load of metal-rich matter out of the gravitational well of the galactic halo and into the intergalactic medium, forming a galactic superwind (Bland-Hawthorn 1995, Heckman et al. 1995, Dahlem et al. 1997, Heckman et al. 2000).

Luminous galaxies exist in various shapes. In 1964, Edwin Hubble created a scheme to classify observed galaxies by their morphology, known as the Hubble sequence. He created a useful classification scheme that features a seamless transition between the different types of galaxies, ranging from elliptical galaxies on the one end to spirals and barred spirals on the other end. While the Hubble sequence provides a useful order for the variety of galaxy types, modern theories of hierarchical galaxy formation have shown that the actual evolution of galaxies does not simply follow the Hubble sequence.

According to these models, baryons tend to settle into large gaseous disks around the rotation axis of halos that have picked up a sizable amount of angular momentum during their formation. In the dense matter of these proto-galactic disks, stars are created that then build up rotationally supported *spiral galaxies*. Our own galaxy, the Milky Way, belongs to this class of galaxies. The spiral arms of bright stars are most likely related to the structure of the gaseous content of the disk that due to gravitational instabilities forms a spiral pattern. In the high-density spiral arms, star formation is most efficient, and bright, short-lived stars are abundant. It has been argued that when spiral galaxies have depleted their interstellar medium gas, they may lose their distinct spiral arms and turn into *lenticular galaxies*. If a disk is small and massive enough, it can also develop a central bar due to gravitational disk instabilities. In any case, in the modern hierarchical theories of galaxy formation, disk galaxies are the outcome of the primary mode of star formation which is governed by the joint action of radiative cooling and angular momentum conservation.

The second major group, the *elliptical galaxies*, are considered to be the product of galaxy interactions, which occur frequently in the hierarchical CDM model. In particular, according to the merger hypothesis, many massive ellipticals form from the major mergers of spiral galaxies, where two galaxies of comparable size approach and meet each other due to their mutual gravitative pull. The strong tidal forces on the gaseous and stellar components of the galaxies during the merger disrupts the disk structure. Stars are flung into eccentric, elliptic orbits around the newly forming merger core, such that the final remnant is supported by random velocity in the stars, which is characteristic for elliptical galaxies. A large fraction of the gas present in the merging galaxies is driven to the center by the tidal forces, producing a large starburst during the collision. If the angular momentum of the merging system is sufficiently large and provided that enough gas is left over from the starburst, the remaining gas may quickly form a new disk around the remnant. In this case, a new stellar disk can be formed around the spheroidal system of progenitor stars, which then becomes the bulge of a new spiral galaxy. Similarly, secondary infall of gas at later times can regrow a disk around the elliptical galaxy. In this way, mixed morphological types with different bulge-to-disk ratios can be produced, explaining the population of galaxies along the Hubble sequence.

Mergers do not always lead to the total disruption of existing galaxies, especially when the masses of merging systems are very different. At later times, extremely massive dark matter halos form that pull hundreds to thousands of the surrounding galaxies into their potential well. The dynamical timescales within these immense mass concentrations are too long to disrupt the galaxies in a short time, and the difference of size between the smaller galaxies and the large halo is too large to have a devastating effect

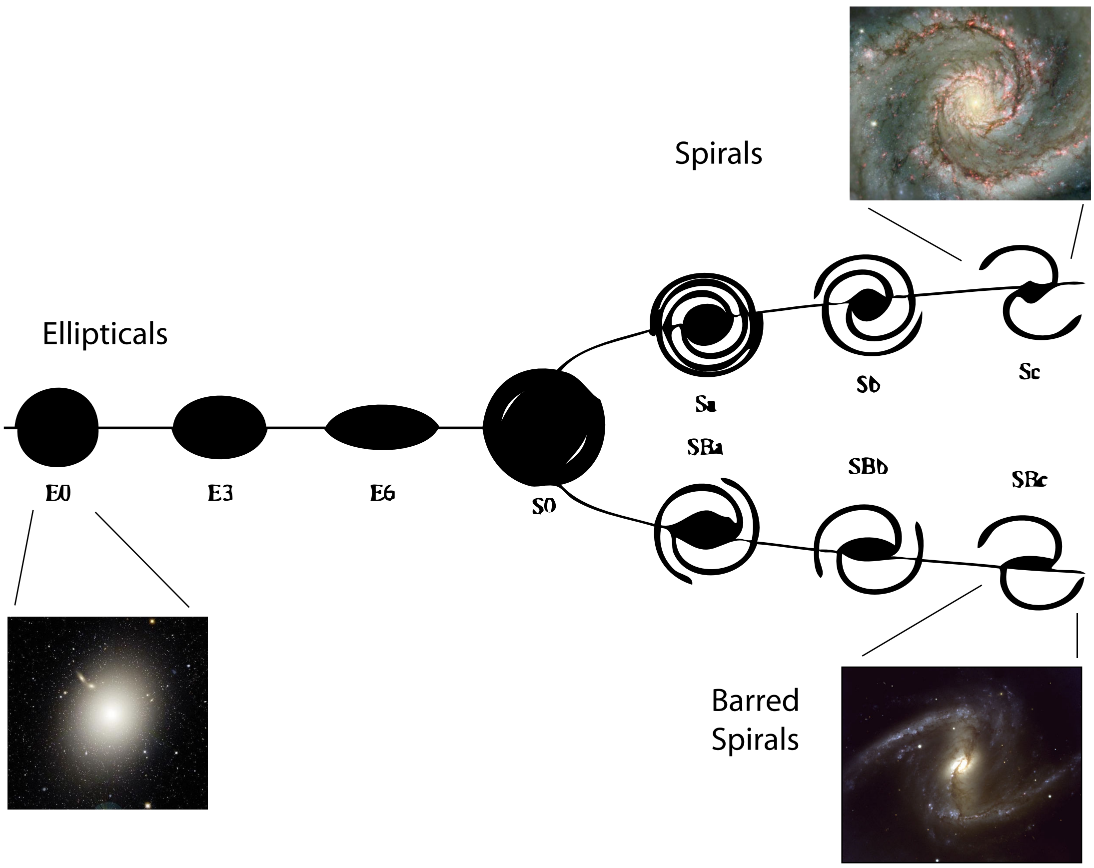

Figure 1.4.: The Hubble Sequence of galaxy morphology, also called the *tuning-fork diagram*. It allows the classification of galaxies into a seamless scheme, ranging from elliptical galaxies on the one end to wide open spirals and barred spirals on the other (Images: NASA).

on the internal structure of the galaxies. The galaxies therefore survive destruction, at least for a while, resulting in groups or clusters of galaxies with tens to thousands of galaxies in a common enveloping halo. The cluster galaxies orbit each other, bound by their common dark matter halo and in the center of a cluster, an extremely massive *cD-galaxy* is often found.

A serious problem of modern simulations of galaxy formation is that the processes of star formation and feedback occur at length scales far below the resolvable scales, yet they nevertheless influence the structure of the whole galaxy, so that they cannot simply be ignored. The diameter of the central star of our solar system, the Sun, measures about 1.39×10^9 m. This is absolutely tiny compared with the typical length scales of galaxies, which measure several kiloparsecs (kpc, where $1\,\mathrm{pc} = 3.085 \times 10^{16}$ m), more than ten orders of magnitude larger. A comprehensive, fully self-consistent modeling of star formation from first principles inside whole galaxies therefore cannot be obtained in the foreseeable future, even if the involved physics were understood much better. Most studies therefore treat star formation as a statistical process in a phenomenological fashion, assuming star formation to be a function of local gas parameters like temperature, density and velocity divergence (e.g. Springel & Hernquist 2003a). Newly

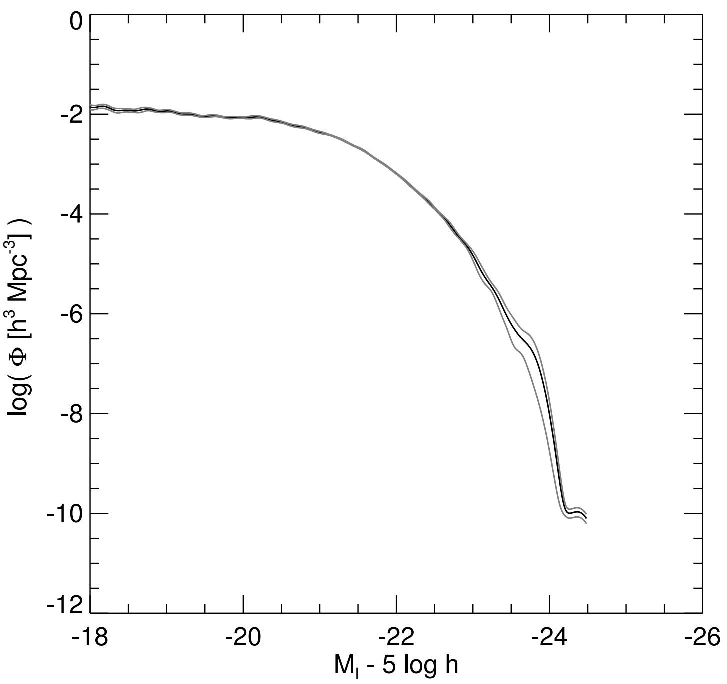

Figure 1.5.: Galaxy luminosity function in the I-band at a redshift of $z = 0.1$ by Blanton et al. (2003), using data gathered by the Sloan Digital Sky Survey (SDSS, York et al. 2000). The gray lines indicate the range of confidence.

formed stellar populations are commonly considered to follow a fixed mass distribution, the *Initial Mass Function* (IMF).

While there are empirical relations between gas density and star formation rates from observations (Kennicutt 1989), the actual modeling of star formation and feedback processes in sub-resolution models is a field with a lot of active work, both in full-blown hydrodynamic simulations (e.g. Katz et al. 1996, Kay et al. 2002, Springel & Hernquist 2003a) as well as in semi-analytic modeling (e.g. White & Rees 1978, Kauffmann et al. 1993, van den Bosch 2002), where dark-matter halos are populated with galaxies by evolving a simplified model for the physics of galaxy formation that represent our today's knowledge of structure formation based on simulations and observations.

It is evident, however, that current prescriptions of star formation and especially feedback lack some important physical factors. Full hydrodynamic simulations still over-predict star formation in dwarf galaxies by a large factor (Murali et al. 2002, Nagamine et al. 2004). Observations suggest that the efficiency of stellar birth in these small objects must be very low, because otherwise the mismatch between the predicted abundance of low-mass dark matter halos and the nearly flat faint-end of the observed galaxy luminosity function cannot be understood (see figure 1.5). A too high rate of star formation in small galaxies not only causes mismatches of the simulated luminosity function with observations, but due to the hierarchical nature of the structure formation process, these errors in crucial building blocks of galaxy growth carry over to later stages in the hierarchy where more massive galaxies are formed. A too efficient cooling of the gas in small galaxies is also thought to produce an early loss of angular momentum of the gas to the dark matter, resulting in too small protogalactic gas disks. This may explain why simulations typically produce stellar disks that are far too small in radial extent compared with observations. The challenge in solving these problems is that it is not yet fully understood how the small-scale processes in the center of galaxies regulate star formation to the levels we observe.

There are different attempts to address this issue. Complex models of chemical enrichment attempt to model the influence of metals in the gas on the condensation of baryons during galaxy formation, arising from the sensitive dependence of cooling rates on metallicity. Other studies deal with the influence of galactic winds ejected from star-forming regions as a result of the cumulative effect of supernova explosions. Such winds could also help to explain the enrichment of the originally pristine intergalactic medium with heavy elements, as observed in absorption spectra to distant quasars (Cowie et al. 1995, Ellison et al. 1999). There is also the idea that additional physical effects that are usually neglected play a crucial part in the feedback cycle. For example, magnetic fields and relativistic cosmic ray particles are known to contribute a significant fraction to the energy density in the interstellar medium of our own galaxy. Despite this, they are typically ignored for simplicity, even though they could in principle play a key role in the regulation of star formation.

On the massive end of the halo mass scale, we face yet another puzzling problem. Given the density and temperature profiles of the diffuse gas in rich clusters of galaxies, one would expect that gas cooling in their central regions should be highly efficient, yielding massive flows of gas sinking down into the center at rates of $1000\,\mathrm{M}_\odot\,\mathrm{yr}^{-1}$ and more (e.g. Peterson et al. 2001). This gas should either fuel star formation at high rates in the central galaxy or be visible as large amounts of accumulated cool gas. However, observations of these objects reveal little evidence for "cluster cooling flows" at these high rates, despite the copious X-ray emission of clusters at a rate consistent with the inferred thermodynamic profiles. This indicates that there must be some process of heating of the central intracluster medium that offsets the radiative energy losses, yet its nature remains unclear.

One plausible way to stop a strong inflow of gas into the cluster center could be in the form of bubbles of hot gas inflated by an active galactic nucleus (AGN), an accreting, super-massive black hole in the central cD-galaxy (Tabor & Binney 1993, Churazov et al. 2001, Enßlin & Heinz 2001, Dalla Vecchia et al. 2004). The energy fed into the intracluster medium (ICM) by sound and shock waves and the heating from the kinematics of the buoyant gas bubbles can be sufficient to cancel out the radiative energy losses in the cluster gas, while leaving the overall structure of the cluster profiles largely unchanged.

Another, more recent idea is to provide the heating of the central intracluster medium by a conductive energy transport (Narayan & Medvedev 2001) from the hotter outer parts of a cluster to its inner parts. Due to the high temperatures of the ICM and the high ionization state of the gas, thermal conduction by electrons becomes in principle large enough to potentially play a crucial role in the evolution of the intracluster temperature structure, and provided the conductivity is high enough, thermal conduction could tap the reservoir of thermal energy in the outer parts of the cluster to prevent a strong cooling flow. However, thermal conduction can be strongly suppressed by magnetic fields, which restrict the motion of electrons to the direction along the magnetic field lines. Still, in the turbulent conditions that are expected in the ICM, this suppression mechanism may effectively become comparatively weak, such that there is room for a profound influence of conduction on the temperature and mass profiles of clusters.

In this work, I report on my work to include the effects of thermal conduction in the hot intracluster gas into an existing cosmological TreeSPH simulation code. I outline how the numerical problems that go along with attempts to solve diffusive problems in SPH can be avoided. I discuss ways to enhance the discretization scheme such that a numerically stable and well-behaved method results that are able to reproduce analytical solutions with good accuracy while keeping both the numerical noise and the computational cost within reasonable bounds. I show how the equilibrium-state of massive galaxy clusters (Zakamska & Narayan 2003) evolves over time under the joint action of radiative cooling and thermal conduction. Using full-blown hydrodynamic simulations of structure formation, I present first results of the study of the effects of thermal conduction on the formation of rich clusters of galaxies.

In the second major part, I show the results of my studies on the influence of cosmic rays on structure formation in hydrodynamical simulations. Dealing with a mix of thermal gas, quasi-relativistic and relativistic particles is by nature a complex endeavor, and hard to tackle within a reasonable amount of computer time. In a collaboration with Torsten Enßlin, Volker Springel, and Christoph Pfrommer, we manage to reduce the computational cost for our studies by using a simplified model for the cosmic ray population. In this model, the spectral representation of the cosmic ray population is approximated as an isotropic distribution with a power-law and a low-energy cut-off in momentum space. We argue that this approach, while not giving a very detailed description of the spectral distribution of the cosmic ray population in every fluid element, can account for the basic hydrodynamical kinematic effects of cosmic rays with suitable accuracy. In that part of this work, I describe the necessary steps I took to include an in-situ computation of the influence of relativistic CR particles during structure formation in the parallel TreeSPH code GADGET in a way that should be adaptable to other SPH implementations conveniently. After demonstrating the validity of the cosmic ray model in some test problems, I show first results from my studies of the cosmic ray modified hydrodynamics in galactic objects, both in models for isolated galaxies and galaxy clusters. These simulations allow for detailed high-resolution studies in a well controlled and clean simulation set-up. I then show and discuss results for self-consistent simulations I carried out, based on cosmological initial conditions that allow to study the impact of cosmic rays on the intergalactic medium and the statistical influence on the halo and galaxy populations.

All models are wrong.
Some are useful.

George E. P. Box

2
The simulation code

During the last twenty years, numerical methods have gained an important role in cosmology. They allow the accurate calculation of predictions of theories of structure formation and have become an indispensable tool for the verification and testing of these theories. The power of numerical simulations unfolds especially in geometrically complex scenarios and in regimes of non-linear dynamics. Here, analytical methods become intractable and the interplay between a multitude of physical processes can only be solved by direct integration. Both computational technology as well as numerical algorithms have significantly advanced since the first cosmological simulations were carried out that dealt with the motion of only a handful of independently calculated mass points. Modern, sophisticated simulation codes are able to track the evolution of a model universe with more than ten billion mutually interacting, gravitating mass elements (Springel et al. 2005b).

Simulations on this scale have only become possible due to the development of sophisticated code frameworks that offer a much better performance than the direct summation approach to self-gravity, with its prohibitive $\mathcal{O}(N^2)$ scaling for large particle number. Rather than looking at each particle-particle pair individually, the employed algorithms reduce the number of calculations by considering interactions between spatially separated groups of particles with other particles.

There are two basic approaches to do force computations based on such a particle-group scheme. Particle-mesh (PM) methods (Klypin & Shandarin 1983) divide the simulated volume into individual cells and compute the resulting gravitational field in Fourier space. This method is both very fast and scales very well on modern computing clusters, provided the communication overhead between the different processors remains small enough. However, PM codes tend to heavily suppress gravitational forces on scales comparable to the mesh size and smaller, which poses a serious restriction on the attainable spatial dynamic range. Possibilities to circumvent this shortcoming include the direct force summation on small scales, or using an adaptive sub-mesh scheme that helps to increase the resolution in regions of interest, or where strong spatial variations of physical properties exist.

The second basic method of computing the effects of gravitation in a particle-group scheme lies in hierarchical tree methods, following the ideas of (Barnes & Hut 1986,BH in further reference). In this scheme, every tree cell that contains more than a single simulation particle stores information on the multipole moments of the mass distribution it contains. Depending on the distance of an interaction partner, forces exerted by the mass inside the tree cell can then either be evaluated by a multipole evaluation using the pre-computed values, or, for particles at closer distances, the tree cell is opened and its smaller child-cells are used for the force evaluation instead. Due to dynamical updating of the tree structure, the spatial resolution of simulations performed using tree-codes automatically increases in regions with large number densities of simulation particles. This dynamic resolution adjustment comes at the price of varying evaluation costs for certain regions of space, making it difficult in parallel simulation codes to distribute the computational load evenly onto a large number of processors.

Especially in simulations that directly attempt to follow the formation of luminous galaxies, the impact of hydrodynamic interactions on the dynamics of the baryonic matter content of the universe is of high importance. While being of a simpler short-range nature, the hydrodynamics of a gas leads to particularly reach dynamical phenomena, including shock waves and turbulence, which are difficult to treat accurately in numerical codes. Similar to gravitation, there are different methods for computing numerical hydrodynamics, but here the conceptual differences between the two main approaches are much larger.

Eulerian mesh-based hydrodynamics codes discretize the volume of the fluid. This gives them good accuracy for spatial derivatives and shock-capturing, but they are severely challenged by the high dynamic range posed by the cosmological structure formation problem, because they cannot resolve structures below the typical cell size. The other big group of methods is formed by Lagrangian codes, which discretize the mass of the fluid, for example by partitioning it into fluid particles. The great advantage of Lagrangian techniques is that their spatial resolution can adapt to the local properties of the gas. If a gravitational collapse takes place, the small-scale kinematics in a forming halo or galaxy can then still be followed. Also, Lagrangian techniques are Galilean invariant and have no problems in dealing with the large bulk velocities that occur in cosmological applications.

Amongst the Lagrangian simulation methods, Smooth Particle Hydrodynamics (SPH, Lucy 1977, Gingold & Monaghan 1977) has found widespread use in cosmological applications. Here, fluid elements are represented by simulation particles which are modeled to have their gas content smoothly distributed over a finite volume, according to a given kernel function. In simulations that additionally include collisionless dark matter particles (dark matter can only be treated with the N-body method) , the approach allows for a uniform methodology for computing the gravitational forces on different kinds of matter, which is an important advantage given that cosmic structure formation is primarily driven by gravity.

The simulation code used for the present work is the TreeSPH code GADGET-2 (Springel 2005) that was recently released to the public in a basic version. It has the new capability of evaluating forces in a TreePM method that combines the speed of traditional mesh based codes with the adaptive spatial resolution and the short-range precision of a hierarchical BH tree algorithm. The simulation code splits gravitational forces into short-range and long-range components, and uses a sophisticated tree code to evaluate the former, and a particle-mesh method for the latter. A further speedup is obtained by distinguishing the two force components by their temporal variation as well, i.e. long-range force can be integrated on larger timesteps than short range forces because changes in the mass distribution on large scales typically evolve more slowly.

When considering the additional requirement of SPH codes for a fast neighbor search, the hierarchical oct-tree employed in the force computations reveals another advantage. The performance of the evaluation of hydrodynamical forces in SPH heavily depends on the ability to carry out a nearest-neighbor search in a highly optimized fashion. Reusing the BH tree structure in a range-searching algorithm, the important neighbor-search can be performed with an $O(N \log N)$ scaling behavior.

In the physical scenarios we investigate in this work, SPH codes show a number of advantages compared to mesh-based codes. Cosmological simulations feature a large diversity of different physical conditions. Gas temperatures and densities in particular can span multiple decades, and so can characteristic length scales of the simulated objects. The matter-tracing nature of N-body codes combined with the automatically adaptive spatial resolution of SPH that makes SPH an ideal tool for studies on structure formation. Also, the Lagrangian nature of SPH simplifies the implementation of certain physical processes and makes the results straightforward to interpret. This is especially true for advection, which does not need to be treated explicitly, because this is an intrinsic part of the hydrodynamical scheme. There are no diffusive losses of physical quantities associated with the fluid particles.

In the following, we give an overview of the range of physical processes covered in the current version of the simulation code we used to obtain the results presented in this work. Compared to the public version of GADGET-2, the version we use features a much wider set of physical processes, including models for star formation and supernova feedback. This chapter is intended to provide a basic description of the numerical approaches taken to represent the different physics in the code. This background is required in order to understand how the new processes we will introduce later interact with the existing system.

2.1. Collisionless dynamics and gravitation

One of the most important features of the mass-dominating dark matter is its low cross-section for particle-particle interactions. Particles move therefore independently in the collective gravitational potential. Stellar systems like galaxies and clusters of galaxies show a similar behavior, they interact only by their mean gravitational field, while the compact nature of individual stars makes physical collisions between them very rare. For time scales of the order of the age of the universe, the impact of gravitational two-body scattering between stars can therefore be safely neglected in galaxies*.

In the continuum limit, for a phase space distribution $f(\boldsymbol{v}, \boldsymbol{p}, \boldsymbol{t})$, collisionless types of matter (i.e. dark matter or stars in galaxies) fulfill the collisionless Boltzmann equation (also known as Vlasov equation)

$$\frac{\mathrm{d}f}{\mathrm{d}t} = \frac{\partial f}{\partial t} + \frac{\boldsymbol{p}}{m}\frac{\partial f}{\partial \boldsymbol{r}} - \frac{\partial \Phi}{\partial \boldsymbol{r}}\frac{\partial f}{\partial \boldsymbol{p}} = 0, \tag{2.1}$$

where the gravitational potential $\Phi(\boldsymbol{r}, t)$ is the solution of the Poisson equation

$$\Delta\Phi(\boldsymbol{r}, t) = 4\pi G \int f(\boldsymbol{r}, \boldsymbol{p}, t)\, \mathrm{d}\boldsymbol{p}. \tag{2.2}$$

The high-dimensionality of these equations, requiring to not only to sample data in three dimension of space, but rather the full six dimensions of phase-space, makes this problem cumbersome to solve with a classical mesh code with an adequate resolution. The most practical method capable of dealing with the collisionless matter is therefore the Lagrangian N-body method, which samples the phase-space distribution of the matter distribution with a large, but finite number of tracer particles.

A system with a finite number of mass points under gravitational interactions can be fully described by a Hamiltonian

$$H_{\mathrm{grav}} = \sum_i \frac{\boldsymbol{p}_i^2}{2m_i} + \frac{1}{2}\sum_{i,j} m_i m_j\, \varphi(\boldsymbol{r}_j - \boldsymbol{r}_i), \tag{2.3}$$

where $\varphi(\boldsymbol{r})$ describes the interaction potential. Note that we have here formulated the equation in physical coordinates. Cosmological codes commonly use comoving coordinate vectors $\boldsymbol{x} = a(t)\boldsymbol{r}$ instead, which take care of the expansion of space in a numerically convenient form. The corresponding canonical momenta are then $\boldsymbol{p}_{i,\mathrm{com}} = a(t)^2 m_i \dot{\boldsymbol{x}}$. Since a transcription to comoving coordinates is straightforward, we restrict ourselves to the use of physical quantities for easier readability in this short introduction to our simulation technique. The particle-particle gravitational potential $\varphi(\boldsymbol{r}_{ij})$ is the solution of the Poisson equation

$$\Delta\varphi(\boldsymbol{r}_{ij}) = 4\pi G\, \tilde{\delta}(\boldsymbol{r}_{ij}). \tag{2.4}$$

With vacuum boundary conditions, this reduces to the familiar Newtonian potential, but for the more commonly employed periodic boundary conditions, the solution has a more complicated form. We make use of a normalized distribution function $\tilde{\delta}(\boldsymbol{r}_{ij}) = W(|\boldsymbol{r}_{ij}|, f\epsilon)$ (see section 2.2.1 for closer considerations) with a finite gravitational softening length for represent a point-mass particle. This softens the gravitational force law at small separations, which is necessary to prevent the formation of hard binaries when only a small number of bodies is used to approximate a physical system. The parameter f is set in a way that ensures that the gravitational potential at zero lag, $\varphi(\mathbf{0}) = -Gm/\epsilon$, has the same value as found for a smoothing length of ϵ in a Plummer potential. This simplifies comparison with the the softening method employed in many gravitational simulations on GRAPE hardware accelerated machines (Fukushige et al. 1991, Makino et al. 1997, Hut & Makino 1999, Kawai et al. 2000, Makino 2000). Note that for parti-

*This is different in globular star clusters, where the relaxation time can become smaller than the Hubble time.

cle separations larger than the finite extent of the smoothing kernel function W, the formulation of the smoothed gravitational potential reduces exactly to the Newtonian form.

2.2. Hydrodynamics

2.2.1. Basic SPH concepts

The key concept of the SPH method used in the simulation code GADGET-2 is the idea that any spatial function can be represented by an interpolated field generated from a disordered set of sampling points. The latter correspond to tracer particles that follow the mass flow in the simulation. The interpolation is evaluated using a kernel function $W(\boldsymbol{r}-\boldsymbol{r}', h)$, which has a spatial extent characterized by the smoothing length h. The kernel is normalized so that

$$\int W(\boldsymbol{r}' - \boldsymbol{r}, h)\,\mathrm{d}\boldsymbol{r}' = 1. \tag{2.5}$$

The shape of the kernel function itself can take different forms in principle, and can have a profound influence on the quality of the simulation. The original implementations of SPH (Lucy 1977, Gingold & Monaghan 1977) used a Gaussian kernel function and claimed that only this form can be considered to result in physically meaningful interpretations, but more recent works mostly made use of spline-based kernels (Monaghan & Lattanzio 1985) which drop to zero for $|\boldsymbol{r}-\boldsymbol{r}'| > h$. They prove to be computationally more efficient and can be motivated by the theory of spline interpolation. Usually, the kernel function is chosen to be spherically symmetric, avoiding any preference of certain spatial directions, although a different choice is possible in principle (e.g Shapiro et al. 1996,who adjusted the kernel shape to local properties of the flow). In the following, we limit ourselves to symmetric kernels, and wherever possible abbreviate them by

$$W_{ij}(h) = W(|\boldsymbol{r}_j - \boldsymbol{r}_i|, h). \tag{2.6}$$

In the case of an infinitely dense sampling with fluid points and an infinitesimal small smoothing, the kernel interpolation reduces to an identify:

$$X_{\mathrm{SPH}}(\boldsymbol{r}) = \int X(\boldsymbol{r}')W(|\boldsymbol{r}' - \boldsymbol{r}|, h)\mathrm{d}\boldsymbol{r}' \overset{h\to 0}{=} \int X(\boldsymbol{r}')\delta(|\boldsymbol{r}' - \boldsymbol{r}|)\mathrm{d}\boldsymbol{r}' = X(\boldsymbol{r}) \tag{2.7}$$

However, when we employ the interpolation scheme in real numerical simulations with a finite number of fluid particles, the integral is translated into a sum over a finite number of indexed particles with masses m_i and densities of ρ_i. The typical volume element taken by a particle is given by m_i/ρ_i, and the integral in equation (2.7) turns into

$$X_{\mathrm{SPH}}(\boldsymbol{r}) = \sum_i \frac{X_i m_i}{\rho_i} W(|\boldsymbol{r}' - \boldsymbol{r}|, h), \tag{2.8}$$

This sum has to be evaluated over all particles i with $W > 0$. Kernel functions with a finite support have an advantage here since they allow the spatial region of summation to be reduced strongly, thereby reducing the number of neighboring particles they overlap with. This speeds up the computations significantly.

A key advantage of this form of discretization and interpolation becomes obvious when we consider the problem of obtaining spatial derivatives of the SPH-interpolated quantities. Using a continuously differentiable kernel function, we can obtain the derivative by an ordinary differentiation of the kernel interpolant itself. Neither a finite difference method is required, nor any knowledge on the actual distribution at the points of interest. Like all linear operations on the SPH interpolant, it reduces to applying the operation to the kernel function, which is the only quantity with a spatial variation. Derivatives of the kernel can hence be obtained in a very inexpensive and robust way for analytically differentiable kernel functions:

$$\frac{\partial}{\partial \boldsymbol{r}} X_{\rm SPH}(\boldsymbol{r}) = \sum_i \frac{X_i m_i}{\rho_i} \frac{\partial}{\partial \boldsymbol{r}} W(\boldsymbol{r}_i - \boldsymbol{r}, h). \tag{2.9}$$

The value of the density for an individual particle, obviously one of the most important quantities delivered by SPH methods, can be obtained in different ways. In SPH schemes with a fixed smoothing length, equation (2.8) can be used, using ρ in place of X to obtain

$$\rho_i = \sum_j m_j W_{ij}(h). \tag{2.10}$$

Leaving the kernel length (referred to as "smoothing length") constant for all particles as a function of time forfeits one of SPH's biggest benefits, however, because this ignores the spatial adaptivity offered by Lagrangian methods. When introducing instead a smoothing length that automatically adapts to local particle density, SPH simulations can trace hydrodynamics over a large dynamic range in densities and spatial scales, which is especially advantageous in collapse problems. A common method to adjust the smoothings lengths is to choose the kernel length so that a sphere with a radius of h includes a fixed number of SPH particles. The code GADGET-2 uses a similar approach, but rather than requiring a fixed number of particles, the criterion adopted here is that the kernel volume should contain a fixed gas mass, computed self-consistently based on the density estimate for ρ_i itself, namely

$$M_{\rm smooth} = \frac{4\pi}{3} \rho_i h_i^3. \tag{2.11}$$

The main benefit of this criterion is that it allows a formulation of SPH where both energy and entropy are manifestly conserved, despite the use of fully adaptive smoothing lengths. This will be discussed more at a later point.

With the discretization recipes introduced above, it is already possible to construct a solving scheme for adiabatic hydrodynamics. Consider an ideal fluid made up of a number of gas mass elements denoted by an index i, its dynamics is then described by the Euler equation

$$\frac{\mathrm{d}\boldsymbol{v}}{\mathrm{d}t} = -\frac{\boldsymbol{\nabla} P}{\rho}, \tag{2.12}$$

where $\mathrm{d}/\mathrm{d}t = \partial/\partial t + \boldsymbol{v} \cdot \partial/\partial \boldsymbol{r}$ is the convective derivative. The hydrodynamic pressure P is given by the equation of state of an ideal gas $P = (\gamma - 1)\rho u$, and

$$\frac{\mathrm{d}u}{\mathrm{d}t} = -\frac{P}{\rho}\boldsymbol{\nabla}\boldsymbol{v}. \tag{2.13}$$

describes the evolution of the thermal energy u per unit mass. Perhaps the simplest form of an SPH discretization that we can obtain from the Euler equation is

$$\frac{\mathrm{d}\boldsymbol{v}_i}{\mathrm{d}t} = -\sum_j \frac{m_j P_j}{\rho_i \rho_j}\boldsymbol{\nabla}_i W_{ij}. \tag{2.14}$$

This equation, although obtained by simply applying the basic prescriptions of SPH, has the disadvantage that it does not conserve linear and angular momentum exactly, only in the rarely encountered case of constant pressure. This is because pair interactions do not obey the physical principle of action and reaction.

It is therefore better to symmetrize the equation using the identity

$$\frac{\boldsymbol{\nabla}P}{\rho} = \boldsymbol{\nabla}\left(\frac{P}{\rho}\right) + \frac{P}{\rho^2}\boldsymbol{\nabla}\rho, \tag{2.15}$$

obtaining

$$\frac{\mathrm{d}\boldsymbol{v}_i}{\mathrm{d}t} = -\sum_j m_j \left[\frac{P_j}{\rho_j^2} + \frac{P_i}{\rho_i^2}\right] \frac{\partial}{\partial \boldsymbol{r}_i} W_{ij}(h_i). \tag{2.16}$$

Upon a first look, it might seem as if a factor of $1/2$ is missing in this symmetrized form. However, the real effect of the second pressure term on the right hand side is a geometrical correction for an unbalanced particle distribution and for uniform particle distributions is entirely canceled out by the symmetry of W_{ij}.

Similar techniques can also be used to symmetrize the energy term. In this way, momentum is manifestly conserved in a scheme with a global-timestep. If particles are advanced in an asynchronous way by means of an individual timestepping method, as is done in many modern simulation codes (including GADGET-2), the conservation is however no longer explicit.

2.2.2. The entropy equation

It is important to note that the above formulation does not conserve entropy explicitely, although modeled around adiabatic hydrodynamics. In the past, there have been two complementary approaches to SPH simulation codes, one designed to manifestly conserve entropy (e.g. Hernquist 1993), and the other to explicitely conserve energy, as shown in the example of an SPH discretization above (Couchman et al. 1995, Davé et al. 1997, Springel et al. 2001).

There is however a way to obtain a set of equations that explicitely conserves both, energy and entropy, as pointed out by Springel & Hernquist (2002). The approach suggested requires that the smoothing lengths are constrained as stated in equation (2.11), and is most conveniently formulated in terms of an entropic function.

For a simple, ideal gas undergoing an adiabatic compression or expansion, the gas density and pressure are related by

$$\frac{P}{\rho^{\gamma}} = A(s) = \text{const.} \tag{2.17}$$

The constant coefficient for in the relation, $A(s)$, is an exclusive function of the thermodynamic entropy s and can therefore be used as an adiabatic invariant of hydrodynamics. The Hamiltonian of gas dynamics becomes especially simple when expressed using this variable. $A(s)$ is sometimes called the *entropic function*, but due to its direct one-to-one relation with thermodynamic entropy, we will simply call it *entropy* for simplicity.

This entropic function is used as the fundamental quantity to describe the thermodynamic state of a mass element represented by a simulation particle. Wherever the actual energetic content of a gas element is required, it can be inferred from

$$u = \frac{A(s)\,\rho^{\gamma-1}}{\gamma - 1}. \tag{2.18}$$

Using this entropic function, the Hamiltonian of the hydrodynamic system is given as

$$H = \sum_i \left(\frac{\boldsymbol{p}_i^2}{2m_i} + \frac{m_i A_i \rho_i^{(\gamma-1)}}{\gamma - 1} \right). \tag{2.19}$$

This formulation is valid for an ideal gas with a constant adiabatic index γ. Compounds of different gas components of different nature and different behavior under compression need to be included as separate sub-components, each contributing its own energy term. For small changes, it is however possible to adopt the form of equation (2.19), choosing an effective adiabatic index for the described compound gas in its current state, and adjusting the entropic function A_i to one that mimics the gas behavior. It is clear, though, that when extending the formalism in this way, one effectively gives up the explicit entropy conservation in favor of an extended scope of the simulated physical effects.

In the above, the density ρ_i may appear as an independent variable, but actually it is determined according to the descriptions for estimating smoothing lengths and densities self-consistently, and hence is only a function of all particle positions, $\rho_i = \rho_i(\boldsymbol{r}_1, \ldots, \boldsymbol{r}_N, h_i)$. While the dependence of the SPH density on particle smoothing lengths is implementation-dependent, it is possible to eliminate them from the overall equation by using a restrained Hamiltonian. Here, the functions that define the individual smoothing length parameters are added to the original Hamiltonian using Lagrange multipliers λ_j.

The new representation of the hydrodynamical system in its smoothing-length constrained form is

$$H' = H + \sum_j \lambda_j \left(M_{\text{smooth}} - \frac{4\pi\rho_j h_j^3}{3} \right). \tag{2.20}$$

The Hamiltonian presented above is describing an evolution that manifestly conserves entropy and energy of an adiabatically moving hydrodynamic system. The additional constraints make sure that the thermal energy depends only on the entropy per unit mass and the particle positions, but not on the SPH smoothing lengths. The extended Hamiltonian automatically pays respect to those requirements at all orders of variations of the smoothings lengths.

To derive equations of motion from this Hamiltonian, the first step is a determination of the Lagrange multipliers λ_j. The simulated system should not react to small changes of the particles' smoothing lengths. As mentioned, the energy of the system should not depend on the choice of smoothing lengths or their evolution through the time integration process. This demand,

$$\frac{\partial H'}{\partial h_j} = 0, \tag{2.21}$$

allows the determination of the Lagrange multipliers as

$$\lambda_j = \frac{3 m_j A_j \rho_j^{\gamma-2}}{4\pi h_j^3} \left[1 + \frac{3\rho_j}{h_j} \left(\frac{\partial \rho_j}{\partial h_j} \right)^{-1} \right]^{-1}. \tag{2.22}$$

Using these factors in equation (2.20), the constrained Hamiltonian can be directly evaluated, and then yields the equations of adiabatic motion for the system of gas mass elements as

$$m_i \frac{\mathrm{d}\boldsymbol{v}_i}{\mathrm{d}t} = \frac{\mathrm{d}\boldsymbol{p}_i}{\mathrm{d}t} = \frac{\partial}{\partial \boldsymbol{r}_i} H' = -\sum_j m_j A_j \rho_j^{\gamma-2} f_j \frac{\partial}{\partial \boldsymbol{r}_i} \rho_j. \tag{2.23}$$

The term f_j is a factor that results from the spatial variation of SPH smoothing lengths in the system, and is given by

$$f_j = \left[1 + \frac{h_j}{3\rho_j} \frac{\partial \rho_j}{\partial h_j} \right]^{-1} \tag{2.24}$$

The spatial derivative of density on the right hand side is translated according to the SPH formalism described above. Note that, differently from before, the derivation is performed with respect to a specially denoted variable that not necessarily all kernel functions depend on. Therefore, this derivative becomes

$$\begin{aligned} \frac{\partial}{\partial \boldsymbol{r}_i} \rho_j &= \sum_k m_k \frac{\partial}{\partial \boldsymbol{r}_i} W_{jk}(h_k) = (\delta_{ik} + \delta_{ij}) \sum_k m_k \frac{\partial}{\partial \boldsymbol{r}_i} W_{jk}(h_j) \\ &= m_i \frac{\partial}{\partial \boldsymbol{r}_i} W_{ji}(h_j) + \delta_{ij} \sum_k m_k \frac{\partial}{\partial \boldsymbol{r}_i} W_{ik}(h_i). \end{aligned} \tag{2.25}$$

Interestingly, the final equation of adiabatic motion,

$$\frac{\mathrm{d}\boldsymbol{v}_i}{\mathrm{d}t} = -\sum_j m_j \left[f_i \frac{P_i}{\rho_i^2} \frac{\partial}{\partial \boldsymbol{r}_i} W_{ij}(h_i) + f_j \frac{P_j}{\rho_j^2} \frac{\partial}{\partial \boldsymbol{r}_i} W_{ij}(h_j) \right], \tag{2.26}$$

which directly results from the Hamiltonian created according to the principles of entropy and energy conservation, features a symmetric form already, without any further modifications. Note also that when choosing fixed values of unity for both f_i and f_j, the equation of motion reduces to one that has been used before in the literature (e.g Thomas & Couchman 1992), where it was motivated by a direct discretization of the Euler equations. However, only when the terms due to the variation of the smoothing lengths, encoded by the f-factors, are included as well, a manifestly conservative behavior of the system for the entropy as well as the energy is obtained.

2.2.3. Shocks and viscosity

The formalism presented above is able to describe the physics of adiabatic compression and expansion in a way that preserves both thermal energy and entropy. In reality, flows of gases easily and often develop discontinuities and shocks, where particle-interactions on microphysical scales dissipate kinetic energy into unordered, thermal motion, and generate entropy. Mesh-based codes trace discontinuities with sophisticated Riemann solvers. For SPH codes, taking a similar approach is hard to accomplish, due to the fundamentally different modeling of hydrodynamics. The common method to mimic the non-adiabatic behavior at shock fronts is the introduce a viscous force

$$\left.\frac{\mathrm{d}\boldsymbol{v}_i}{\mathrm{d}t}\right|_{\mathrm{visc}} = -\sum_j m_j \Pi_{ij} \frac{\partial}{\partial \boldsymbol{r}_i} \tilde{W}_{ij} \tag{2.27}$$

into the simulation formalism, where Π_{ij} is an artificial viscosity tensor that creates a non-vanishing force when particles rapidly approach each other. The kinetic energy taken from particles in this way is transformed into a growth of the entropy (and hence thermal energy) at a rate of

$$\left.\frac{\mathrm{d}A_i}{\mathrm{d}t}\right|_{\mathrm{visc}} = \frac{1}{2}\frac{\gamma-1}{\rho_i^{\gamma-1}} \sum_j m_j \Pi_{ij} \boldsymbol{v}_{ij} \frac{\partial}{\partial \boldsymbol{r}_i} \tilde{W}_{ij}. \tag{2.28}$$

In most SPH codes, the Monaghan-Balsara (Monaghan & Gingold 1983, Balsara 1995) artificial viscosity

$$\Pi_{ij} = \begin{cases} [-\alpha\, c_{ij}\, \mu_{ij} + \beta_{ij}\, \mu_{ij}^2]/\rho_{ij} & \text{for } \boldsymbol{v}_{ij} \cdot \boldsymbol{r}_{ij} < 0 \\ 0 & \text{otherwise} \end{cases} \tag{2.29}$$

is employed, where μ_{ij} is the particle approach velocity projected on their connecting line, divided by the relative distance in units of the particle smoothing length.

$$\mu_{ij} = \frac{h_{ij} \boldsymbol{v}_{ij} \cdot \boldsymbol{r}_{ij}}{\left|\boldsymbol{r}_{ij}\right|^2}. \tag{2.30}$$

The variables h_{ij}, ρ_{ij} and c_{ij} with two indices here denote the arithmetic means of the corresponding properties of the two particles i and j. The parameters α and β are used to adjust the strength of the viscosity. The sound velocity of a particle, c_i is

$$c_i = \sqrt{\frac{\gamma P_i}{\rho_i}}. \tag{2.31}$$

The current version of the GADGET-2 code uses a more recently proposed parameterization of the viscosity by Monaghan (1997). In analogy with Riemann problems, it is based on a signal velocity v_{ij}^{sig} between two particles and formulates the viscosity term as

$$\Pi_{ij} = -\frac{\alpha}{2}\frac{w_{ij}\, v_{ij}^{\mathrm{sig}}}{\rho_{ij}} \tag{2.32}$$

where $w_{ij} = \max(\boldsymbol{v}_{ij} \cdot \boldsymbol{r}_{ij}/|\boldsymbol{r}_{ij}|, 0)$ is the relative velocity of the particle approach, projected onto the connecting line between the two particles and ρ_{ij} is the mean density of the two. When using a simple estimate of the signal velocity, like

$$v_{ij}^{\mathrm{sig}} = c_i + c_j - 3w_{ij}, \tag{2.33}$$

the viscosity term evaluates to

$$\Pi_{ij} = -\frac{\alpha}{2}\frac{[c_i + c_j - 3w_{ij}]w_{ij}}{\rho_{ij}}. \tag{2.34}$$

Compared to the Monaghan-Balsara formulation, this parameterization of the artificial viscosity is less steeply peaked towards particle separations significantly smaller than one softening length. Also, the effective pressure generated by the Monaghan viscosity has no explicit dependency on particle separations or softening lengths, fitting perhaps better into the overall formulation where one typically tries to eliminate effects due to numerically motivated parameters such as softening lengths.

There is still one further adjustment that is often made to the viscosity modelling. In the presence of shear flows, the angular momentum transport due to the artificial viscosity, which takes place at some level even without shocks, can be considerably above the analytically expected vanishingly low value for an ideal gas. This can be alleviated by introducing a viscosity-limiter based on a local estimate of the shear strength. This is usually done based on the quantity

$$f_i = \frac{|\boldsymbol{\nabla} \times \boldsymbol{v}|_i}{|\boldsymbol{\nabla} \cdot \boldsymbol{v}|_i + |\boldsymbol{\nabla} \times \boldsymbol{v}|_i}, \tag{2.35}$$

which provides a relative measure of the strength of the shear component. In practice, the viscosity tensor is simply multiplied by a factor $(f_i + f_j)/2$ in order to reduce it in the presence of strong local shear. The estimates of divergence and curl required here are performed with the standard equations of the SPH formalisms discussed in section 2.2.1.

The physical processes described above are well understood and their modeling is done in a way that is based on well established numerical experience. Unfortunately, this is not really the case for all components of the physics that describe the formation of luminous galaxies. While in many cases we know and understand some the basic parts of these processes, precise and reliable physical models are sometimes either not available or would require enormous amounts of computational time when solved in a brute-force fashion. We will therefore have to invoke strong simplifications where necessary.

In the following, we describe these physical ingredients and explain our approaches to model them. We also explain our simplifying assumptions where they are made, and the models we invoke to describe certain sub-grid physics in a statistical fashion.

2.3. Radiative heating and cooling

The ability to interact with radiation is a fundamentally important property of baryonic matter. Without radiative processes, above all the dissipation of thermal energy by radiative cooling, cosmic gas could not have collapsed to the highly overdense structures that ultimately form the billions of stars that make up the luminous parts of galaxies. Of course, without radiative processes, stars could not work either. While virialized dark matter systems remain in a quasi-static state, hot gas in contrast can lose its pressure support by emission of energy in the form of photons, and can this way flow into the halo center.

This emission of photons in the thin astrophysical plasma inside halos can be the result of line transitions within atoms that get excited in collisions, or be caused by a free-bound process where a formerly unbound electron settles down into a bound state with a proton. The most intense form of cooling, especially at high temperatures is the loss of kinetic energy of electrons moving through plasma, emitting bremsstrahlung when they experience strong accelerations in the Coulomb field of nuclei. It is obvious that the actual cooling rates and the shape of the cooling function heavily depend on the composition of the gas under consideration. Gas containing heavy elements features more atomic transitions between bound states of high energy. This results in a strongly enhanced cooling rate via line transitions in metal-enriched gas compared to the pristine primordial mix of helium and hydrogen generated during big bang nucleosynthesis.

The GADGET-2 simulation code in the form we use it here neglects the influence of metallicity on the cooling efficiency and instead assumes a constant composition of gas equal to the primordial mix of 24% helium and 76% hydrogen by mass. For this composition, the temperature and density dependent gas cooling rate is evaluated using the chemical network and rate equations described by Katz et al. (1996), under the assumption of collisional ionization equilibrium. Here, a large range of possible radiative processes is combined, relying on reaction rates taken from Black (1981) with modifications by Cen (1992).

For convenience, the summed reaction rates (i.e. the net cooling or heating rate) for a given composition of hydrogen and helium can be expressed as a function of temperature alone, to be multiplied with the square of density to introduce the density dependence as an independent variable. The shape of this function, $\Lambda(T)$ is shown in figure 2.1. The actual loss of thermal energy by radiative cooling per unit mass is given by

$$\left.\frac{\mathrm{d}u}{\mathrm{d}t}\right|_{\mathrm{cooling}} = -\frac{\Lambda_{\mathrm{cool}}}{\rho} \tag{2.36}$$

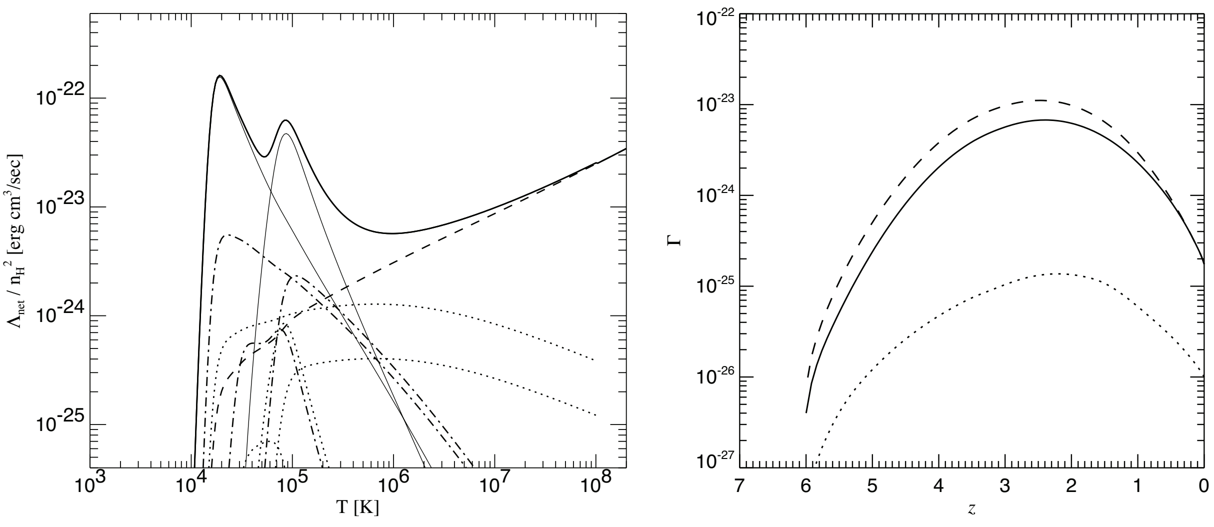

Figure 2.1.: Left panel: Cooling rates as a function of temperature for a primordial mix of helium and hydrogen. The thick solid line shows the total cooling rate. Partial contributions are indicated for Bremsstrahlung (dashed), excitation (thin lines), ionization (dot-dashed) and recombination processes (dotted). At temperatures below 10^4 K, the gas is mostly neutral, and molecular cooling effects would take over. Right panel: Heating rate by ionizing radiation as a function of redshift.

In the real universe, photon emission and absorption processes together work as radiative energy transport, relocating thermal energy from high density regions, where emission processes increase effectivity like ρ^2 into space. Solving this radiative transport of energy in full generality is a very complex task, however, at present still beyond the capabilities of a self-consistent treatment within a simulation code. Solving the radiative transfer equation is particularly difficult due to the high dimensionality of the problem, involving a six-dimensional transport equation (three dimensions of space and velocity each, minus one for the constraint of velocity to the speed of light, plus one dimension of frequency). For this reason, GADGET-2 does not try to model radiative transfer and assumes that cooling radiation is lost from the system altogether.

Nevertheless, the simulation code still allows for a global, spatially uniform UV background radiation, which is imposed with a prescribed amplitude as a function of time. In this way, the build-up of an ionizing background that eventually reads to reionization of the universe is accounted for. The ultimate origin of this ionizing flux of energetic photons is still a matter of active research. The plausible candidates for the sources include a first generation of metal-free stars that are not hosted in ordinary galaxies (referred to as population III stars), ordinary stellar populations in galaxies, and quasars or mini-quasars. It is thought that such sources of hard radiation first reionize a bubble around them, As more and more photons are produced by the source, they bubbles grow in size and eventually overlap, until the whole universe is reionized and the radiation fields of the sources combine to form a ubiquitous, nearly homogeneous and isotropic UV background radiation field.

For an atom of species i in a radiation field with a flux density of $J(\nu)$ at a frequency of ν, the rate of photo-ionization is defined by

$$\Gamma_{\gamma i} = \int_{\nu_i}^{\infty} \frac{4\pi J(\nu)}{h\nu} \sigma_i(\nu)\, \mathrm{d}\nu \tag{2.37}$$

where ν_i is the frequency threshold for ionization, and $\sigma_i(\nu)$ is the cross section for photoionization of this particle species at a given frequency. The rate of heating by photoionization for the given species is

$$\epsilon_i = \int_{\nu_i}^{\infty} \frac{4\pi J(\nu)}{h\nu} \sigma_i(\nu)\, (h\nu - h\nu_i)\, \mathrm{d}\nu \tag{2.38}$$

The heating associated with the reionizing radiation has a profound impact on the formation of baryonic structures in small halos, since it can heat gas that already had lost its virial pressure support and was on the verge of collapsing. However, this effect will only operate efficiently in halos with very small virial temperature, just above the threshold of 10^4 K for atomic line cooling to a few times this temperature. While this will make these small halos very inefficient sites of star formation after the epoch of reionization, it is clear that large systems will be hardly affected, i.e. for them other feedback processes are needed to understand their (low) efficiencies of star formation.

The ionizing UV background radiation first comes into play at around $z \approx 6$ in our simulations and reionizes the universe at this epoch, roughly at the time when the first massive, luminous galaxies form. The right panel of figure 2.1 shows the time-dependent rates of photo-ionization applied in this work. This model is based on a parameterization by Haardt & Madau in a slightly updated form by Davé et al. (1999). The model assumes that quasars are responsible for the dominant part of the UV background flux that reionizes the universe.

2.4. Star formation and feedback

The treatment of star formation in a fully resolved and self-consistent manner is far beyond the scope of modern simulations, and will most likely be for a long time still. Microphysical effects play a crucial role in the creation of the luminous components of galaxies, and it is clear that individual stars are many orders of magnitudes smaller than the typical length scales resolvable in cosmological numerical simulations. Star formation can therefore only be addressed with an approximative treatment in our simulations.

In the simulation method we employ for this work, star formation is treated in a statistical way using a subresolution model (Springel & Hernquist 2003a), where the interstellar medium is pictured as a compound fluid of cold condensed clouds in a hot ambient medium at pressure equilibrium. The mass of the simulation gas particle that samples the matter distribution is imagined to be split into two components, considering hot and cold matter separately ($\rho = \rho_{\mathrm{hot}} + \rho_{\mathrm{clouds}}$).

The formation of the cold clouds is facilitated by the shape of the cooling function, where below temperatures of $T < 10^6$ K, there is a trend for runaway cooling and thermal instability. A small volume element of gas with a temperature slightly below that of the surrounding medium will increase this difference due to its more efficient cooling, and ultimately collapse under its own gravitational pull to a dense molecular cloud that is the possible site for the birth of new stars. The rate of mass transfer from the hot ambient gas phase into cold clouds is therefore modeled to occur on a typical cooling time scale and is

$$\left(\frac{\mathrm{d}\rho_{\mathrm{clouds}}}{\mathrm{d}t}\right)_{\mathrm{cool}} = -\left(\frac{\mathrm{d}\rho_{\mathrm{hot}}}{\mathrm{d}t}\right)_{\mathrm{cool}} = \rho_{\mathrm{hot}}\frac{\left(\frac{\mathrm{d}u_{\mathrm{hot}}}{\mathrm{d}t}\right)_{\mathrm{cool}}}{\Delta u} = \frac{(1-f)\,\Lambda_{\mathrm{net}}(\rho_{\mathrm{hot}}, u_{\mathrm{hot}})}{u_{\mathrm{hot}} - u_{\mathrm{clouds}}}. \tag{2.39}$$

The factor f is used to limit the formation of clouds to the thermally unstable conditions for the gas. In thermally unstable conditions, it is set to a value of 0, enabling the condensation to its full extent. Stable regions where no cloud formation is expected will feature $f = 1$, which effectively disables the condensation into cold gas clouds in this equation.

These cold clouds are assumed to form stars on a characteristic star formation time scale, so that the transfer of cold cloud matter into stellar objects is

$$\left(\frac{\mathrm{d}\rho_{\star}}{\mathrm{d}t}\right)_{\mathrm{SF}} = -\left(\frac{\mathrm{d}\rho_{\mathrm{cold}}}{\mathrm{d}t}\right)_{\mathrm{SF}} = \frac{\rho_{\mathrm{cold}}}{t_{\star}}. \tag{2.40}$$

A crucial point in the star formation and feedback model in this approach is that a fixed fraction β_{SN} of the newly generated stellar mass is assumed to form massive stars that after rapid stellar evolution on a time scale of $\approx 3 \times 10^7$ yr end their lives in an explosion as energetic core collapse supernova. For the model employed here, it is assumed that the supernova explosions occur immediately, with no time delay. The exact size of the supernova fraction β_{SN} depends on the Initial Mass Function (IMF) assumed for star formation. If the IMF is top-heavy, more energy would be available.

The stars that explode as supernovae are assumed to propel their entire gas mass back into the hot phase of the gas, neglecting the mass that stays bound in compact remnants of the former stars, which can be neutron stars or even black holes, depending on the masses of the original stars. In addition to the transfer of mass into the hot gas phase, the supernovae deploy a large amount of energy that is thermalized as the shock front of the explosion runs through the ISM. This energy feedback is captured in the model by assuming an average energy u_{SN} per stellar mass unit to be fed back into the hot gas phase.

Further, it is assumed that cold clouds of gas are evaporated by the bubbles of hot matter created in the supernova explosions. The model estimates the mass of evaporated cold clouds to be proportional by a factor of A_{SN} to the mass of supernovae themselves, with a dependence of A_{SN} given by the theoretical model of McKee & Ostriker (1977).

Adding up all the effects of the assumed supernova feedback model, the partial densities of the two gas components evolve like

$$\left(\frac{\mathrm{d}\rho_{\mathrm{clouds}}}{\mathrm{d}t}\right)_{\mathrm{SN}} = -A_{\mathrm{SN}}\,\beta_{\mathrm{SN}}\,\frac{\rho_{\mathrm{clouds}}}{t_{\star}} \tag{2.41}$$

and

$$\left(\frac{\mathrm{d}\rho_{\mathrm{hot}}}{\mathrm{d}t}\right)_{\mathrm{SN}} = -\left(\frac{\mathrm{d}\rho_{\star}}{\mathrm{d}t}\right)_{\mathrm{SN}} = \beta_{\mathrm{SN}}\,\frac{\rho_{\mathrm{clouds}}}{t_{\star}}. \tag{2.42}$$

$$\left(\frac{\mathrm{d}(u_{\mathrm{hot}}\rho_{\mathrm{hot}})}{\mathrm{d}t}\right)_{\mathrm{SN}} = u_{\mathrm{SN}}\,\beta_{\mathrm{SN}}\,\frac{\rho_{\mathrm{clouds}}}{t_\star}, \tag{2.43}$$

Collecting all the different evolution equations originating from this network of processes results in evolution equations for the different density components, namely

$$\frac{\mathrm{d}\rho_{\mathrm{clouds}}}{\mathrm{d}t} = -(1 + A_{\mathrm{SN}}\beta_{\mathrm{SN}})\,\frac{\rho_{\mathrm{clouds}}}{t_\star} + \frac{1-f}{u_{\mathrm{hot}} - u_{\mathrm{clouds}}}\Lambda_{\mathrm{net}}(\rho_{\mathrm{hot}}, u_{\mathrm{hot}}), \tag{2.44}$$

$$\frac{\mathrm{d}\rho_{\mathrm{hot}}}{\mathrm{d}t} = (1 + A_{\mathrm{SN}})\beta_{\mathrm{SN}}\,\frac{\rho_{\mathrm{clouds}}}{t_\star} - \frac{1-f}{u_{\mathrm{hot}} - u_{\mathrm{clouds}}}\Lambda_{\mathrm{net}}(\rho_{\mathrm{hot}}, u_{\mathrm{hot}}) \tag{2.45}$$

and

$$\frac{\mathrm{d}\rho_\star}{\mathrm{d}t} = (1 - \beta_{\mathrm{SN}})\,\frac{\rho_{\mathrm{clouds}}}{t_\star}.. \tag{2.46}$$

The total energy budget of the considered compound gas volume adds up to

$$\frac{\mathrm{d}}{\mathrm{d}t}(\rho_{\mathrm{hot}}u_{\mathrm{hot}} + \rho_{\mathrm{clouds}}u_{\mathrm{clouds}}) = -\Lambda_{\mathrm{net}}(\rho_{\mathrm{hot}}, u_{\mathrm{hot}}) + \beta_{\mathrm{SN}}\,u_{\mathrm{SN}}\,\frac{\rho_{\mathrm{clouds}}}{t_\star} - (1-\beta_{\mathrm{SN}})\,u_{\mathrm{clouds}}\,\frac{\rho_{\mathrm{clouds}}}{t_\star} \tag{2.47}$$

It can be shown that for a constant u_{clouds}, this equation can be reduced to a term that describes the evolution of the hot phase temperature over time. This equation is also integrated in the simulation framework, considering it as an evolution of the hot phase entropic function rather than in its energy form of

$$\rho_{\mathrm{hot}}\frac{\mathrm{d}u_{\mathrm{hot}}}{\mathrm{d}t} = \beta_{\mathrm{SN}}\frac{\rho_{\mathrm{clouds}}}{t_\star}(u_{\mathrm{SN}} + u_{\mathrm{clouds}} - u_{\mathrm{hot}}) - A_{\mathrm{SN}}\beta_{\mathrm{SN}}\frac{\rho_{\mathrm{clouds}}}{t_\star}(u_{\mathrm{hot}} - u_{\mathrm{clouds}}) - f\Lambda_{\mathrm{net}}(\rho_{\mathrm{hot}}, u_{\mathrm{hot}}) \tag{2.48}$$

Equations (2.44)-(2.46) and (2.48) form the basic description of the multiphase model for the sub-resolution statistical treatment of cold clouds in a hot, ambient gas, as described by Springel & Hernquist (2003a). By selecting appropriate values for the parameters f, β_{SN}, u_{SN} , A_{SN} and $t_\star$, this model framework can be tuned to accommodate different IMFs and different descriptions of the energy and mass deposition from core-collapse supernovae.

In the following, the parameter choices for our simulations with star formation are explained. All simulations presented later in this work rely on this choice of settings, unless explicitly stated otherwise. As described above, the parameter f can be used to switch between thermally stable and unstable states of the simulated gas volume corresponding to possible star formation or its suppression, or even to a smooth transition between these two states. Gas at temperatures where cooling rates are an increasing function of temperature will not feature the thermally unstable behavior that this model is based on. Looking at the cooling efficiency function in Figure 2.1, it is obvious that the thermal instability mostly occurs in ambient gas with temperature in the range of $10^5 - 10^6$ K. Metal-enriched gas will, due to the increased emissivity at low temperatures by the larger number of possible line emission processes, feature the minimum of the cooling rate at somewhat higher temperatures, up to 10^7 K. In the simulation code, this knowledge is used to disable the thermal instability term for "hot" ambient gas below temperatures of

10^5 K. Further, a density threshold $\rho_{\rm th}$ for the instable collapse into cold clouds is introduced, motivated by the observed threshold density for star formation (Kennicutt 1989).

This density threshold is also used to define a reference point for the scaling of the relations used to describe further behavior of physics on the multiphase system. Most prominently, the star formation time scale has been chosen as a Schmidt-type law, linking the star formation time-scale of clouds to the dynamical time of gas. With

$$t_\star = t_\star^0 \left(\frac{\rho}{\rho_{\rm th}}\right)^{-1/2}, \tag{2.49}$$

a new parameter for the star formation efficiency, $t_\star^0$ is used, along with the threshold density for star formation $\rho_{\rm th}$. In the simulations shown later in this work, this star formation time scale is set to a value of $t_*^0 = 2.1$ Gyr, in concordance with the findings of Kennicutt (1998) for star forming disks.

Springel & Hernquist (2003a) show that the threshold density for this model treatment can be obtained based on the assumption that the effective pressure of the multiphase gas is continuous at the onset of the self-regulating star formation process. As discussed in their work in detail, for an effective gas temperature of 10^4 K at the threshold density, corresponding to a specific energy u_4, the defining equations of this model require the threshold density to be equal to

$$\rho_{\rm th} = \frac{x_{\rm th}}{(1-x_{\rm th})^2} \frac{\beta_{\rm SN} u_{\rm SN} - (1-\beta_{\rm SN}) u_{\rm c}}{t_*^0 \Lambda \frac{u_{\rm SN}}{A_0}}. \tag{2.50}$$

Here, $x_{\rm th} \approx 1 - A_0 u_4 / u_{\rm SN}$ is the mass fraction of gas contained in cold clouds at the density threshold, and $\Lambda = \Lambda_{\rm net}(\rho, u)\rho^{-2}$ is a density independent cooling efficiency of the gas.

For the statistical description of star formation, a fixed Salpeter IMF is used that is neither a function of time or redshift, nor of the physical parameters of the star forming gas clouds or their surroundings. For this IMF, a fraction of $\beta_{\rm SN} \simeq 0.10$ of the total created stellar matter is formed in stars more massive than $8 M_\odot$. These massive stars are assumed to run through stellar evolution rapidly in a negligibly small time interval, such that their mass is instantly returned into the gas phase. Along with the mass, a typical energy output of 10^{51} erg per supernova is assumed to be fed back into the surrounding medium to offset cooling and regulate the star formation rate. With the assumed shape of the initial mass function, this yields

$$u_{\rm SN} = 4 \times 10^{48}\,{\rm erg}\,M_\odot^{-1}\,(1-\beta_{\rm SN})\beta_{\rm SN}. \tag{2.51}$$

The rate of cloud evaporation by supernova explosions, A, is also modeled with a simple power-law dependence, following the arguments of McKee & Ostriker (1977). Again using the threshold density as a reference point, the cloud mass evaporated per supernova unit mass equals

$$A(\rho) = A_0 \left(\frac{\rho}{\rho_{\rm th}}\right)^{-4/5}. \tag{2.52}$$

The parameter A_0 closely corresponds to the temperature of the hot, ambient medium. For a choice of $A_0 \approx 1000$, equation (2.48) will evolve the specific internal energy $u_{\rm hot}$ towards a value that corresponds

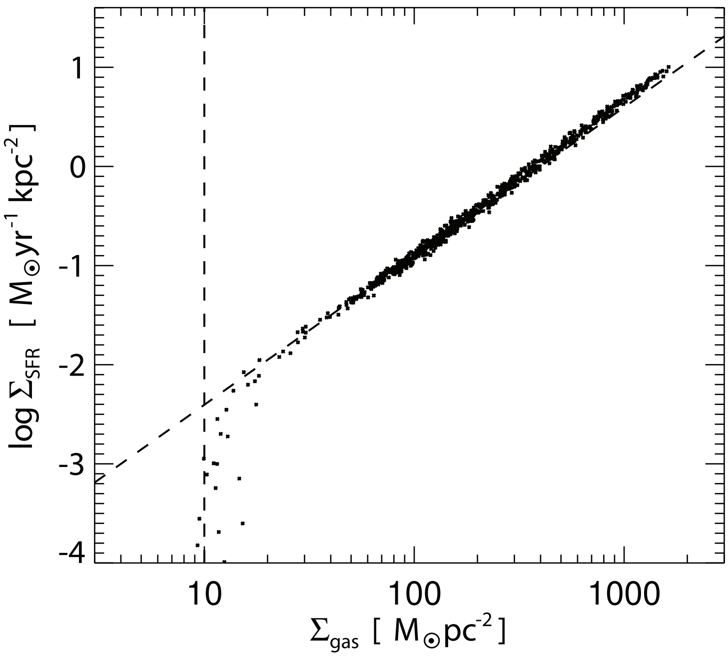

Figure 2.2.: Star formation rate per unit area as a function of gas surface density, measured in a simulation using the multiphase gas model with a fiducial choice of the star formation time scale $t_*^0 = 2.1\,\mathrm{Gyr}$ (dots), compared to the observed global Schmidt-law found by Kennicutt (1998). (Source: Springel & Hernquist (2003a)).

to $T_{\mathrm{hot}} > \frac{u_{\mathrm{SN}}}{A_0} = 10^5\,\mathrm{K}$, thus making sure that the temperature of the hot gas phase is within the regime where the thermal instability is supposed to be effective.

While some of the parameters of this multiphase model are chosen rather arbitrarily based on plausibility arguments and simplifying assumptions, the results it produces are a good match for known observational data on the correlation of gas density with star formation rate. Such data is for example found in Kennicutt (1998), where, based on a large sample of disk galaxies, a 'global Schmidt law' for the correlation between gas surface density and the star formation rate per unit area was found, taking the form

$$\Sigma_{\mathrm{SFR}} = (2.5 \pm 0.7) \times 10^{-4} \left(\frac{\Sigma_{\mathrm{gas}}}{\mathrm{M}_\odot\,\mathrm{pc}^2} \right)^{1.4\pm0.15} \frac{\mathrm{M}_\odot}{\mathrm{yr\,kpc}^2}. \qquad (2.53)$$

Figure 2.2 shows a comparison of this observational finding with measurements acquired from a numerical simulation of a compound galaxy consisting of a dark halo and a star-forming gaseous disk, with the model parameters chosen as described above, taken from Springel & Hernquist (2003a). The multiphase model gives a good match in amplitude and slope to the observations, and at the same time reproduces the cut-off for low gas surface densities very well, validating that the multiphase model seems an appropriate model for the description of star formation.

Note that the multiphase model by itself includes no kinetic feedback of star formation and does not produce galactic outflows. Yet, galactic super-winds and outflows are observed in many starbursting galaxies (Bland-Hawthorn 1995, Dahlem et al. 1997, Frye et al. 2002), and have been the subject of intense theoretical studies in recent years (Mac Low & Ferrara 1999, Scannapieco et al. 2001). The processes that lead to the galactic winds and outflows are still not well understood. It is plausible that the ejection of gas from the galactic disks is the cumulative result of many coeval supernovae that create a hot bubble of gas that can break out of the dense interstellar medium and spew its contents into the halo. The simulation code optionally tries to model these galactic winds in a phenomenological way that is directly motivated by the observations of Martin (1999), who found that the mass-loss rates in winds from galactic disks is of the order of the star formation rates, with no clear dependence of the wind speed on the size of the galaxy.

It therefore is plausible first order approximation to assume that for a given mass of cold gas turning into stellar matter, a fixed multiple η_{w} of the latter is ejected from the disk as galactic winds. The energy that this wind material carries is supplied by the supernova explosions, so can be taken to be proportional to the feedback energy computed in the multiphase model by a factor of χ_{w}. Springel & Hernquist (2003a) show that using this recipe, one obtains an outflow from the disk with

$$\dot{M}_{\mathrm{wind}} = \eta_{\mathrm{w}}\, \dot{M}_{*} \tag{2.54}$$

and a velocity of

$$v_{\mathrm{wind}} = \sqrt{\frac{2\beta_{\mathrm{SN}}\,\chi_{\mathrm{w}}\, u_{\mathrm{SN}}}{\eta_{\mathrm{SN}}(1-\beta_{\mathrm{SN}})}}. \tag{2.55}$$

In massive galaxies, these winds can give rise to a “galactic fountain”, where an axial outflow from the disk eventually falls back to the disk in a planar inflow, because the initial wind speed at the base is too low to escape from the dark matter potential well. For low-mass halos, where the wind velocity exceeds the halo escape velocity, the wind model will instead lead to a galactic outflow. Here, metals are transported from the dense, star forming regions where they are created into intergalactic space, leading to a metal “pollution” of the formerly pristine intergalactic medium. At the same time, the loss of baryons to the wind will reduce the long-term star formation rate of the galaxy substantially.

2.5. Summary

As emphasized earlier, the range of physical processes that play an important role in structure formation, and especially in the formation of luminous objects like galaxies and clusters of galaxies, is very wide and complex. Our simulation code tries to model the most important and potentially most influential parts of the relevant physics. In fact, the GADGET-2 code is currently one of the most widely employed tools for simulating cosmological structure formation. But it is important to not fall victim to the illusion of a complete understanding. Even though the GADGET-2 code is already sophisticated and advanced, the physical processes described in its presented implementation are still rather restricted, and perhaps more importantly, form only a partial selection of the all the physics that may be of crucial importance in galaxy formation.

Intense research efforts are therefore being directed towards developing ever better simulation methods that cover more physics, both in GADGET-2 as well as in other cosmological codes. Examples for such attempts include the self-consistent inclusion of magnetic fields (Dolag et al. 2005) or the strong energetic feedback that is supposed to originate from active galactic nuclei, i.e. from super-massive black holes at the center of galaxies that are in the process of accretion. Energy liberated by active quasars and AGN could have a crucial influence on the dynamics of the intracluster medium in clusters of galaxies, or merger events that build up the massive elliptical galaxies that we see today and at high redshift (Springel et al. 2005a).

My own work in this thesis is very much in line with this general effort to make simulation codes more faithful in their modelling of astrophysical reality. In the following sections of this work, I will present my work to simulate the effects of thermal conduction and cosmic ray physics on structure formation, building up on the simulation prescriptions as presented above. As we will see, these physical processes have a number of highly interesting effects on galaxy and galaxy cluster formation in the cosmological context.

I believe there is no philosophical high-road in science, with epistemological signposts. No, we are in a jungle and find our way by trial and error, building our road behind us as we proceed.

Max Born

3

Thermal conduction in cosmological SPH simulations

3.1. Introduction

Clusters of galaxies provide a unique laboratory to study structure formation and the material content of the Universe, because they are not only the largest virialized systems but are also believed to contain a fair mixture of cosmic matter. Among the many interesting aspects of cluster physics, their X-ray emission takes a particularly prominent role. It provides direct information on the thermodynamic state of the diffuse intracluster gas, which makes up for most of the baryons in clusters.

While the bulk properties of this gas are well understood in terms of the canonical ΛCDM model for structure formation, there are a number of discrepancies between observations and the results of present hydrodynamical simulations. A long standing problem is to understand in detail the scaling relations of observed clusters, which deviate significantly from simple self-similar predictions. In particular, poor clusters of galaxies seem to contain gas of higher entropy in their centres than expected (Ponman et al. 1999, Lloyd-Davies et al. 2000). This has been interpreted either to be evidence for an entropy injection due to non-gravitational processes (Loewenstein 2000, Wu et al. 2000, Metzler & Evrard 1994), or as a sign of the selective removal of low-entropy gas by gas cooling (Voit et al. 2002, Wu & Xue 2002). Both processes combined could influence the thermodynamic properties of the ICM in a complex interplay (Tornatore et al. 2003, Borgani et al. 2004).

Another interesting problem occurs for the radial temperature profiles of clusters. Most observed clusters show a nearly isothermal temperature profile, often with a smooth decline in their central parts

(Allen et al. 2001, Johnstone et al. 2002, Ettori et al. 2002). Nearly isothermal profiles are also obtained in adiabatic simulations of cluster formation (e.g. Frenk et al. 1999). However, clusters in simulations that include dissipation typically show temperature profiles that increase towards the centre (e.g. Lewis et al. 2000), different from what is observed.

Perhaps the biggest puzzle is that spectroscopic X-ray observations of the centres of clusters of galaxies have revealed little evidence for cooling of substantial amounts of gas out of the intracluster medium (e.g. David et al. 2001), even though this would be expected based on their bolometric X-ray luminosity alone (Fabian 1994). The apparent absence of strong cooling flows in clusters hence indicates the presence of some heating source for the central intracluster medium. Among the proposed sources are AGN, buoyant radio bubbles (Churazov et al. 2001, Enßlin & Heinz 2001), feedback processes from star formation (Bower et al. 2001, Menci & Cavaliere 2000), or acoustic waves (Fujita et al. 2004).

Recently, Narayan & Medvedev (2001) have proposed that thermal conduction may play an important role for the cooling processes in clusters. The highly ionised hot plasma making up the ICM in rich clusters of galaxies should be efficient in transporting thermal energy, unless heat diffusion is inhibited by magnetic fields. If conduction is efficient, then cooling losses in the central part could be offset by a conductive heat flow from hotter outer parts of clusters, which forms the basis of the conduction idea.

Indeed, using simple hydrostatic cluster models where cooling and conductive heating are assumed to be locally in equilibrium, Zakamska & Narayan (2003, ZN henceforth) have shown that the central temperature profiles of a number of clusters can be well reproduced in models with conduction (see also Fabian et al. 2002, Voigt et al. 2002, Brüggen 2003, Voigt & Fabian 2004). The required conductivities are typically sub-Spitzer (Medvedev et al. 2003). This suggests that thermal conduction may play an important role for the thermodynamic properties of the ICM.

On the other hand, it has been frequently argued (Chandran & Cowley 1998, Malyshkin & Kulsrud 2001) that magnetic fields in clusters most likely suppress the effective conductivity to values well below the Spitzer value for an unmagnetised gas. Note that rotation measurements show that magnetic fields *do exist* in clusters (e.g. Vogt & Enßlin 2003). However, little is known about the small-scale field configuration, so that there is room for models with chaotically tangled magnetic fields (Narayan & Medvedev 2001), which may leave a substantial fraction of the Spitzer conductivity intact. The survival of sharp temperature gradients along cold fronts, as observed by Chandra in several clusters (Markevitch et al. 2000, Vikhlinin et al. 2001, Ettori & Fabian 2000), may require an ordered magnetic field to suppress conduction. For a more complete review of the effects of magnetic fields on galactic clusters, see Carilli & Taylor (2002) and references therein.

It is clearly of substantial interest to understand in detail the effects conduction may have on the formation and structure of galaxy clusters. In particular, it is far from clear whether the temperature profile required for a local balance between cooling and conduction can naturally arise during hierarchical formation of clusters in the ΛCDM cosmology. This question is best addressed with cosmological hydrodynamical simulations that fully account for the coupled non-linear dynamics of the gas subject to radiative cooling and thermal conduction.

In this chapter, I present the work I did in collaboration with Volker Springel and Klaus Dolag to develop a new numerical implementation of conduction and include it in a modern TreeSPH code for structure formation. The final formulation we propose is robust and explicitly conserves thermal energy, even when individual timesteps for each particle are used.

After examining idealised test problems to validate our implementation of conduction, we apply our code to realizations of the static cluster models of ZN, investigating in particular, to what degree conduction may balance cooling in these clusters, and for how long this approximate equilibrium can be maintained. We also discuss results for a first set of cosmological simulations of cluster formation. We here compare simulations that follow only adiabatic gas dynamics, or only cooling and star formation, with corresponding ones that also include conduction. As we will see, thermal conduction can lead to a substantial modification of the final thermodynamic properties of rich clusters.

The outline of this chapter is as follows. In Section 2, we discuss the basics of the conduction equation, and our numerical approach for discretising it in SPH. In Section 3, we show first test runs of conducting slabs, which we also use to illustrate various issues of numerical stability. We consider isolated clusers in Section 4, constructed with an initial equilibrium model, while in Section 5 we present a comparison of results obtained in cosmological simulations of cluster formation. Finally, Setion 6 summarizes and discusses our findings in this interesting topic.

3.2. Thermal conduction in SPH

3.2.1. The conduction equation

Heat conduction is a transport process for thermal energy, driven by temperature gradients in the conducting medium. Provided the mean free path of particles is small compared to the scale length of the temperature variation, the local heat flux can be described by

$$\boldsymbol{j} = -\kappa \boldsymbol{\nabla} T, \tag{3.1}$$

where $T(\boldsymbol{r})$ gives the temperature field, and κ is the heat conduction coefficient, which may depend on local properties of the medium. For example, in the case of an astrophysical plasma, we encounter a strong dependence of κ on the temperature itself.

The rate of temperature change induced by conduction can simply be obtained from conservation of energy, viz.

$$\rho \frac{\mathrm{d}u}{\mathrm{d}t} = -\boldsymbol{\nabla} \cdot \boldsymbol{j}, \tag{3.2}$$

where u is the thermal energy per unit mass, and ρ denotes gas density. Eliminating the heat flux, this can also be written directly in terms of u, giving the heat conduction equation in the form

$$\frac{\mathrm{d}u}{\mathrm{d}t} = \frac{1}{\rho} \boldsymbol{\nabla} \cdot (\kappa \boldsymbol{\nabla} T). \tag{3.3}$$

Note that the temperature is typically simply proportional to u, unless the mean particle weight changes in the relevant temperature regime, for example as a result of a phase transition from neutral gas to ionised plasma. In the thin astrophysical plasmas we are interested in, the strong temperature dependence of the Spitzer conductivity (see below) suppresses conduction in low-temperature gas heavily. For all practical purposes we can set $u = k_{\rm B}T/[(\gamma - 1)\mu] = c_v T$, where $\mu = 0.588\, m_{\rm p}$ is the mean molecular weight of a fully ionised gas with the primordial mix of helium and hydrogen, and c_v is the heat capacity per unit mass.

3.2.2. Spitzer conductivity

Spitzer (1962) derived the classical result for the heat conductivity due to electrons in an ionised plasma. It is given by

$$\kappa_{\rm sp} = 1.31\, n_e \lambda_e k_{\rm B} \left(\frac{k_{\rm B} T_e}{m_e} \right)^{1/2}, \tag{3.4}$$

where n_e is the electron density, and λ_e the electron mean free path. Interestingly, the product $n_e\lambda_e$ depends only on the electron temperature T_e,

$$\lambda_e n_e = \frac{3^{3/2}(k_{\rm B}T_e)^2}{4\sqrt{\pi} e^4 \ln \Lambda}, \tag{3.5}$$

provided we neglect the very weak logarithmic dependence of the Coulomb logarithm Λ on electron density and temperature, which is a good approximation for clusters. We will set $\ln \Lambda = 37.8$, appropriate for the plasma in clusters of galaxies (Sarazin 1988). The Spitzer conductivity then shows only a strong temperature dependence, $\kappa_{\rm sp} \propto T^{5/2}$, and has the value

$$\kappa_{\rm sp} = 8.2 \times 10^{20} \left(\frac{k_{\rm B} T}{10\,{\rm keV}} \right)^{5/2} \frac{\rm erg}{\rm cm\ s\ keV}. \tag{3.6}$$

Note that the presence of magnetic fields can in principle strongly alter the conductivity. Depending on the field configuration, it can be suppressed in certain directions, or even in all directions in cases of certain tangled fields. The field configuration in clusters is not well understood, and it is currently debated to what degree magnetic fields suppress conduction. We will assume that the modification of the conductivity can be expressed in terms of an effective conductivity, which we parameterise as a fraction of the Spitzer conductivity.

Even in the absence of magnetic fields, the Spitzer conductivity can not be expected to apply down to arbitrarily low plasma densities. Eventually, the scale length of the temperature gradient will become comparable or smaller than the electron mean free path, at which point the heat flux will saturate, with no further increase when the temperature gradient is increased (Cowie & McKee 1977). This maximum heat flux $j_{\rm sat}$ is given by

$$j_{\rm sat} \simeq 0.4\, n_{\rm e} k_{\rm B} T \left(\frac{2 k_{\rm B} T}{\pi m_{\rm e}} \right)^{1/2}. \tag{3.7}$$

In order to have a smooth transition between the Spitzer regime and the saturated regime, we limit the conductive heat flux by defining an effective conductivity (Sarazin 1988) in the form

$$\kappa_{\rm eff} = \frac{\kappa_{\rm sp}}{1 + 4.2\,\lambda_{\rm e}/l_T}. \tag{3.8}$$

Here $l_T \equiv T/|\nabla T|$ is the characteristic length-scale of the temperature gradient.

3.2.3. SPH formulation of conduction

At first sight, equation (3.3) appears to be comparatively easy to solve numerically. After all, the time evolution generated by the diffusion equation smoothes out initial temperature variations, suggesting that it should be quite 'forgiving' to noise in the discretisation scheme, which should simply also be smoothed out.

In practice, however, there are two problems that make it surprisingly difficult to obtain stable and robust implementations of the conduction equation in cosmological codes. The first has to do with the presence of second derivatives in equation (3.3), which in standard SPH kernel-interpolants can be noisy and sensitive to particle disorder, as mentioned earlier. The second is that an explicit time integration method can easily lead to an unstable integration if large local gradients arise due to noise. We will discuss our approaches to solve these two problems in turn.

A simple discretisation of the conduction equation in SPH can be obtained by first estimating the heat flux for each particle applying standard kernel interpolation methods, and then estimating the divergence in a second step. However, this method has been shown to be quite sensitive to particle disorder (Brookshaw 1985), which can be traced to the effective double-differentiation of the SPH-kernel. In addition, this method has the practical disadvantage that an intermediate result, the heat flux vectors, need to be computed and stored in a separate SPH-loop.

It is hence advantageous to use a simpler SPH discretisation of the Laplace operator, which should ideally involve only first order derivatives of the smoothing kernel. Such a discretisation has been proposed before (Brookshaw 1985, Monaghan 1992), and we here give a brief derivation of it in three dimensions.

For a well-behaved field $Y(\boldsymbol{x})$, we can consider a Taylor-series approximation for $Y(\boldsymbol{x}_j)$ in the proximity of $Y(\boldsymbol{x}_i)$, e.g.

$$\begin{aligned} Y(\boldsymbol{x}_j) - Y(\boldsymbol{x}_i) \;=\; & \nabla Y\Big|_{\boldsymbol{x}_i} \cdot (\boldsymbol{x}_j - \boldsymbol{x}_i) + \\ & \frac{1}{2}\sum_{sk} \frac{\partial^2 Y}{\partial x_s \partial x_k}\Big|_{\boldsymbol{x}_i} (\boldsymbol{x}_j - \boldsymbol{x}_i)_s (\boldsymbol{x}_j - \boldsymbol{x}_i)_k + \\ & O(\boldsymbol{x}_j - \boldsymbol{x}_i)^3. \end{aligned} \tag{3.9}$$

Neglecting terms of third and higher orders, we multiply this with

$$\frac{(\boldsymbol{x}_j - \boldsymbol{x}_i)\boldsymbol{\nabla}_i W(\boldsymbol{x}_j - \boldsymbol{x}_i)}{|\boldsymbol{x}_j - \boldsymbol{x}_i|^2}, \tag{3.10}$$

where $W(\boldsymbol{x}) = W(|\boldsymbol{x}|)$ is the SPH smoothing kernel. Note that we choose this kernel to be spherically symmetric and normalised to unity. The expression in equation (3.10) is well behaved for $\boldsymbol{x}_j \to \boldsymbol{x}_i$ under these conditions. Introducing the notations $\boldsymbol{x}_{ij} = \boldsymbol{x}_j - \boldsymbol{x}_i$ and $W_{ij} = W(\boldsymbol{x}_j - \boldsymbol{x}_i)$, we integrate over all $\boldsymbol{x}_j$ and note that

$$\int \boldsymbol{x}_{ij} \frac{\boldsymbol{x}_{ij}\boldsymbol{\nabla}_i W_{ij}}{|\boldsymbol{x}_{ij}|^2} d^3\boldsymbol{x}_j = 0, \tag{3.11}$$

$$\int (\boldsymbol{x}_{ij})_s (\boldsymbol{x}_{ij})_k \frac{\boldsymbol{x}_{ij}\boldsymbol{\nabla}_i W_{ij}}{|\boldsymbol{x}_{ij}|^2} d^3\boldsymbol{x}_j = \delta_{sk}. \tag{3.12}$$

So the term linear in $\boldsymbol{\nabla} Y$ drops out, and the terms involving off-diagonal elements of the Hesse matrix of Y vanish, so that the sum over the second order term simply reduces to $\boldsymbol{\nabla}^2 Y$. We hence end up with

$$\boldsymbol{\nabla}^2 Y\bigg|_{\boldsymbol{x}_i} = -2 \int \frac{Y(\boldsymbol{x}_j) - Y(\boldsymbol{x}_i)}{|\boldsymbol{x}_{ij}|^2} \boldsymbol{x}_{ij}\boldsymbol{\nabla}_i W_{ij}\, \mathrm{d}^3\boldsymbol{x}_j. \tag{3.13}$$

This analytical approximation of the Laplacian can be easily translated into an SPH kernel interpolant. To this end, we can replace the integral by a sum over all particles indexed by j, and substitute the volume element $\mathrm{d}^3\boldsymbol{x}_j$ by its discrete SPH analogue m_j/ρ_j. The values of the field $Y(\boldsymbol{x})$ at the particle coordinates can be either taken as the value of the intrinsic particle property that is evolved, $Y(\boldsymbol{x}_i) = Y_i$, or as a kernel interpolant of these values, $Y(\boldsymbol{x}_i) = \langle Y_i \rangle$, where for example

$$\langle Y_i \rangle = \sum_j Y_j \frac{m_j}{\rho_j} W(\boldsymbol{x}_{ij}). \tag{3.14}$$

We then end up with a discrete SPH approximation of the Laplace operator in the form

$$\boldsymbol{\nabla}^2 Y\bigg|_i = -2 \sum_j \frac{m_j}{\rho_j} \frac{Y_j - Y_i}{|\boldsymbol{x}_{ij}|^2} \boldsymbol{x}_{ij}\boldsymbol{\nabla}_i W_{ij}. \tag{3.15}$$

We now consider how this can be applied to the thermal conduction problem, where the conductivity may also show a spatial variation. Using the identity

$$\boldsymbol{\nabla}(\kappa \boldsymbol{\nabla} T) = \frac{1}{2}\left[\boldsymbol{\nabla}^2(\kappa T) - T\boldsymbol{\nabla}^2\kappa + \kappa\boldsymbol{\nabla}^2 T\right], \tag{3.16}$$

we can use our result from equation (3.15) to write down a discretised form of equation (3.3):

$$\frac{\mathrm{d}u_i}{\mathrm{d}t} = \sum_j \frac{m_j}{\rho_i\rho_j} \frac{(\kappa_j + \kappa_i)(T_j - T_i)}{|\boldsymbol{x}_{ij}|^2} \boldsymbol{x}_{ij}\boldsymbol{\nabla}_i W_{ij}. \tag{3.17}$$

This form is antisymmetric in the particles i and j, and the energy exchange is always balanced on a pairwise basis, i.e. conservation of thermal energy is manifest. Also, it is easy to see that the total entropy can only increase, and that heat always flows from higher to lower temperature.

The conductivities κ_i and κ_j in equation (3.17) are effectively arithmetically averaged. As proposed by Cleary & Monaghan (1999), the numerical behaviour of the conduction can be improved by replacing this arithmetic mean the harmonic mean.

$$\frac{\kappa_i + \kappa_j}{2} \quad \mapsto \quad \kappa_{ij} = \frac{2\kappa_i \kappa_j}{\kappa_i + \kappa_j} \tag{3.18}$$

They showed that this ensures a continuous heat flux even in cases when the heat conductivity exhibits a discontinuity, as for example along the interface between different phases. It is clear then that this modification should also behave better when the conductivity changes extremely rapidly on small scales, as it can happen for example in ICM gas when cool particles get into direct contact with comparatively hot neighbours. Indeed, we found this symmetrisation to give numerically more robust behaviour, particularly in simulations that in addition to heat conduction also were subject to radiative cooling. Note that since we have $\min(\kappa_i, \kappa_j) \leq 2\kappa_i\kappa_j/(\kappa_i + \kappa_j) \leq 2\min(\kappa_i, \kappa_j)$, the Cleary & Monaghan average stays always close to the smaller of the two conductivities involved, to within a factor of two.

3.2.4. Numerical implementation details

We have implemented heat conduction in a new version of the massively parallel TreeSPH-code GADGET (Springel et al. 2001), which is a general purpose code for cosmological structure formation. As discussed in chapter 2. the present version, GADGET-2, uses the 'entropy formulation' of SPH proposed by Springel & Hernquist (2002) which conserves both energy and entropy (in regions without shocks) for fully adaptive smoothing lengths. In this formulation, an entropic function

$$A = (\gamma - 1)\frac{u}{\rho^{\gamma-1}} \tag{3.19}$$

is evolved as independent variable for each particle, instead of the thermal energy per unit mass.

For consistency with this formalism, we need to express the heat conduction equation in terms of entropy. This is easily accomplished in an isochoric approximation, noting that the temperature can be expressed as $T = \mu/k_B\, A\rho^{\gamma-1}$, where μ is the mean molecular weight. This results in

$$\frac{\mathrm{d}A_i}{\mathrm{d}t} = \frac{2\mu}{k_B}\frac{\gamma-1}{\rho_i^{\gamma-1}} \sum_j \frac{m_j \kappa_{ij}}{\rho_i \rho_j} \left(\frac{A_j}{\rho_j^{1-\gamma}} - \frac{A_i}{\rho_i^{1-\gamma}} \right) \frac{\boldsymbol{x}_{ij} \boldsymbol{\nabla}_i W_{ij}}{|\boldsymbol{x}_{ij}|^2}. \tag{3.20}$$

One problematic aspect of the heat conduction equation is that small-scale numerical noise in the temperature field can generate comparatively large heat flows, simply because this noise can involve small-scale gradients of sizable magnitude. Since we are using an explicit time integration scheme for the hydrodynamical evolution, this immediately raises the danger of instabilities in the integration. Unless extremely small timesteps or an implicit integration scheme are used, the energy exchange between two particles due to a small-scale temperature difference can become so large that the explicit time integration "overshoots", thereby potentially *reversing* the sign of the temperature difference between the two particles in conductive contact. This is not only incorrect, but makes it possible for the temperature differences to grow quickly in an oscillatory fashion, causing an instable behaviour of the integration.

We have found that a good method to avoid this problem is to use a kernel interpolant for the temperature field (or entropy field) in the discretisation of the heat conduction equation (3.20), instead of the individual particle temperature values themselves. The interpolant represents a smoothed version of the noisy sampling of the temperature field provided by the particle values, so that on the scale of the SPH smoothing length, small-scale noise in the heat flux is strongly suppressed. Particles will still try to equilibrate their temperatures even within the smoothing radius of each particle, but this will happen at a damped rate. Heat-conduction due to temperature gradients on larger scales is unaffected however. In a later section of this work, we will explicitly demonstrate how this improves the stability of the time integration, particularly when individual and adaptive timesteps are used.

For definiteness, the interpolant we use is a smoothed version $\overline{A}_i$ of the entropy, defined by

$$\rho_i^\gamma \overline{A}_i = \sum_j m_j \rho_j^{(\gamma-1)} A_j W_{ij}. \tag{3.21}$$

We replace A_i and/or A_j on the right-hand-side of equation (3.20) with the interpolants $\overline{A}_i$ and $\overline{A}_j$. Note that the weighting by $\rho^{(\gamma-1)}$ ensures that we obtain a value of $\overline{A}$ that corresponds to a smoothed temperature field, as required since conduction is driven by gradients in temperature and not entropy. However, the density values need to be already known to evaluate this interpolant. An additional SPH loop is required, causing quite a bit of computational overhead. This could in principle be avoided by dropping the density weighting in equation (3.21) is dropped. According to our tests, this appears to be sufficiently accurate in most situations.

Although we use the SPH interpolant for the entropy values in equation (3.20), we still compute the values for the particle conductivity κ based on the intrinsic particle temperature and not on its smoothed counterpart.

The above formulation manifestly conserves thermal energy, in synchronous time stepping schemes. This property may get lost when individual and adaptive time steps are used, where for a given system step only a subset of the particles is evolved. In this case, having only one particle of an interacting couple active at a given integration step in the simulation could lead to a one-sided head conduction, causing a violation of energy conservation. While most of the resulting energy imbalance will only be a temporary fluctuation that will be compensated as soon as the 'inactive' particle in the pair is evolved, the very strong temperature dependence of the conductivity may produce sizable errors in this situation, particularly when coarse timestepping is used. We therefore decided to implement an explicitly conservative scheme for the heat exchange, even when adaptive and individual timesteps are used.

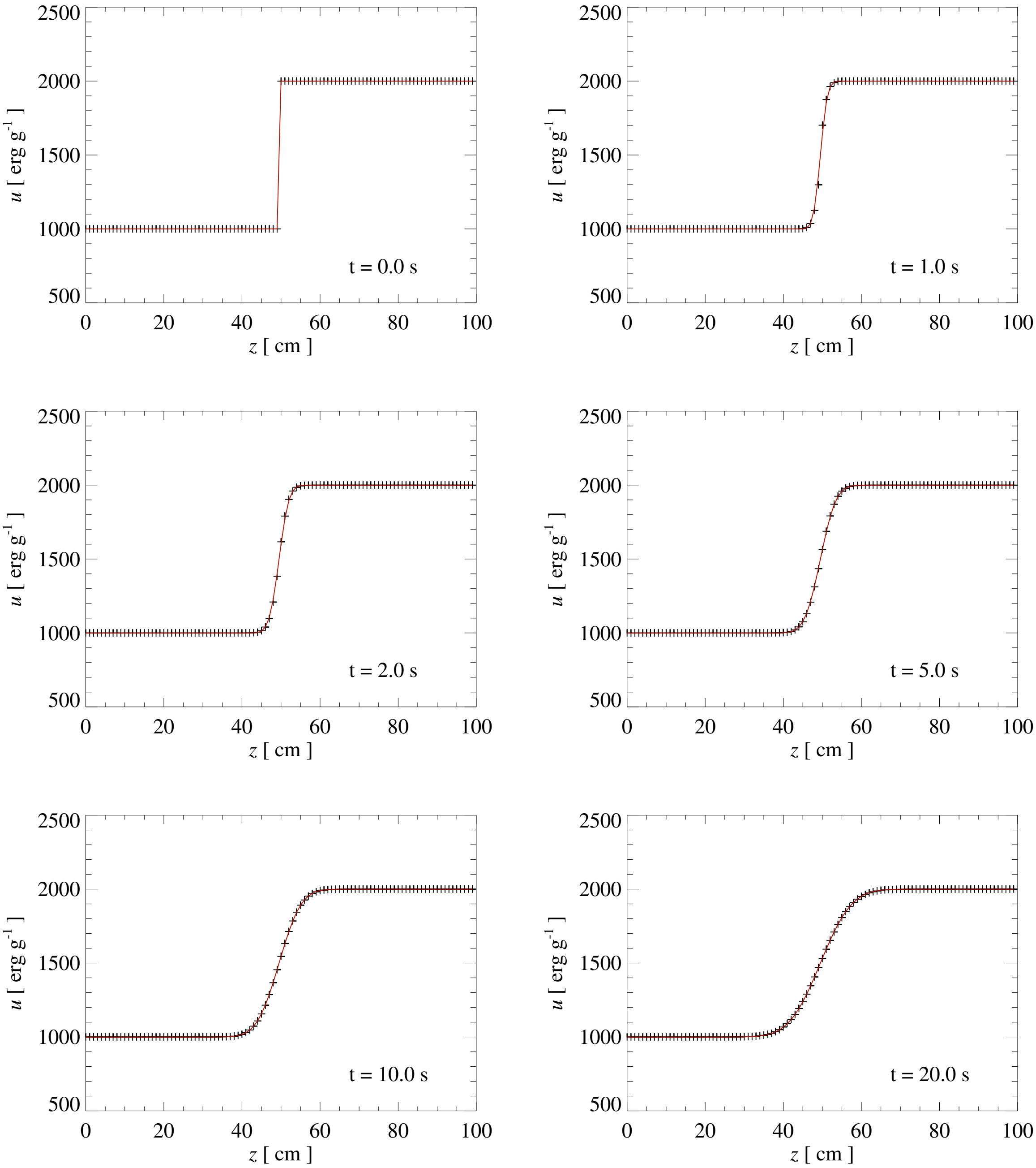

Figure 3.1.: Time evolution of the temperature profile of two slabs of solid material, brought in contact with each other at $t = 0$ along the $z = 50\,\mathrm{cm}$ plane, with an initial difference of thermal energy per unit mass of $\Delta u = 1000\,\mathrm{erg\,g^{-1}}$. Crosses mark numerical results, and the solid line is the analytic solution of the heat conduction equation.

To this end, we define a pairwise exchange of heat energy as

$$E_{ij} \equiv \frac{2\mu}{k_B}\frac{m_i m_j \kappa_{ij}}{\rho_i \rho_j}\left(\frac{A_j}{\rho_j^{1-\gamma}} - \frac{A_i}{\rho_i^{1-\gamma}}\right)\frac{\boldsymbol{x}_{ij}\boldsymbol{\nabla}_i W_{ij}}{|\boldsymbol{x}_{ij}|^2}. \tag{3.22}$$

A simple translation into a finite difference scheme for the time evolution would then be

$$m_i u_i' = m_i u_i + \Delta t_i \sum_j E_{ij}, \tag{3.23}$$

where u_i' and u_i could also be expressed in terms of the corresponding entropy values A_i' and A_i. For individual and variable timesteps, only a subfraction of particles will be 'active' in the current system timestep. These particles have individual timesteps Δt_i, while the 'inactive' particles can be formally assigned $\Delta t_i = 0$ for the step. Equation (3.23) then clearly does not guarantee detailed energy conservation in each system step.

We recover this property in the following way. We update the energy of particles according to

$$m_i u_i' = m_i u_i + \frac{1}{2}\sum_{jk} \Delta t_j (\delta_{ij} - \delta_{ik}) E_{jk} \tag{3.24}$$

in each system step. In practice, the double-sum on the right hand side can be simply computed using the usual SPH loop for active particles. Each interacting pair found in the neighbour search for active particle i is simply used to change the thermal energy of particle i by $\Delta t_i E_{ij}/2$, and that of the neighbouring particle j by $-\Delta t_i E_{ij}/2$ as well. Note that if particle j is active, it carries out a neighbour search itself and will find i itself, so that the total energy change of i due to the presence of j is given by $(\Delta t_i + \Delta t_j)E_{ij}/2$. Energy is conserved by construction in this scheme, independent of the values if individual timesteps of particles. If all particles have equal steps, equation (3.24) is identical to the form of (3.23). As before, in our SPH implementation we convert the final thermal energy change to a corresponding entropy change. These entropy changes are applied instantaneously for all particles at the end of one system step, so that even particles that are inactive at the current system step may have their entropy changed by conduction. The resulting low order of the time integration scheme is sufficient for the diffusion equation.

If conduction is so strong that the timescale of conductive redistribution of thermal energy is short compared to relevant dynamical timescales of the gas, the usual hydrodynamic timestep selected by the code based on the Courant-criterion may become too coarse to follow conduction accurately. We therefore introduce an additional timestep criterion in simulations that follow thermal conduction. To this end, we limit the maximum allowed timestep to some prescribed fraction of the conduction time scale, $A/|\dot{A}_{\rm cond}|$, namely

$$\Delta t_{\rm cond} = \alpha \times \frac{A}{|\dot{A}_{\rm cond}|}, \tag{3.25}$$

where α is a dimensionless accuracy parameter. In our simulations, we typically employed a value of $\alpha = 0.25$, which has provided good enough accuracy at a moderate cost of CPU time.

Finally, in order to account for a possible limitation of conduction by saturation, we compute the gradient of the (smoothed) temperature field in the usual SPH fashion, and then use it to compute l_T and the saturation-limited conductivity based on equation (3.8).

3.3. Illustrative test problems

In this section, we verify our numerical implementation of thermal conduction with a number of simple test problems that have known analytic solutions. We will also investigate the robustness of our formulation with respect to particle disorder, and (initial) noise in the temperature field.

3.3.1. Conduction in a one-dimensional problem

We first consider two solid slabs with different initial temperatures, brought into contact with each other at time $t = 0$. The slabs were realized as a lattice of SPH particles, with dimensions $100 \times 10 \times 10$, and an equidistant particle-spacing of 1 cm. To avoid perturbations of the 1D-symmetry, the simulation volume was taken to be periodic along the two short axes, while kept non-periodic along the long axis, allowing us to study surface effects, if present, on the sides of the slabs that are not in contact. Note that the test was carried out with our 3D code. All particle velocities were set to zero initially, and kept at this value to mimic a solid body. The thermal conductivity was set to a value corresponding to $\alpha = \kappa/(c_v\rho) = 1\ \mathrm{cm}^2\,\mathrm{s}^{-1}$ throughout both materials, independent of temperature.

In Figure 3.1, we compare the time evolution of our numerical results for this test with the analytical solution of the same problem, which is given by

$$u(z,t) = u_0 + \frac{\Delta u}{2}\,\mathrm{erf}\left(\frac{z - z_m}{\sqrt{4\alpha t}}\right), \tag{3.26}$$

where z_m gives the position of the initial difference of size Δu in thermal energy, and u_0 is the mean thermal energy. We see that the numerical solution tracks the analytic result very nicely.

We have also repeated the test for a particle configuration corresponding to a 'glass' (White 1996), with equally good results. For a Poisson distribution of particles, we noted however a small reduction in the speed of conduction when a small number of neighbours of 32 is used. Apparently, here the large density fluctuations due to the Poisson process combined with the smallness of the number of neighbours leads to somewhat poor coupling between the particles. This effect goes away for larger numbers of neighbours, as expected. Note however that in practice, due to the pressure forces in a gas, the typical configuration of tracer particles is much more akin to a glass than to a Poisson distribution.

Next, we examine how robust our formulation is with respect to small-scale noise in the temperature field. To this end, we repeat the above test using the glass configuration, but we perturb the initial thermal energies randomly with fluctuations at an rms-level of $\sigma = 80\ \mathrm{erg\ g}^{-1}$. Further, we increase the maximum timestep allowed for particles to $\Delta t = 1.0$ s.

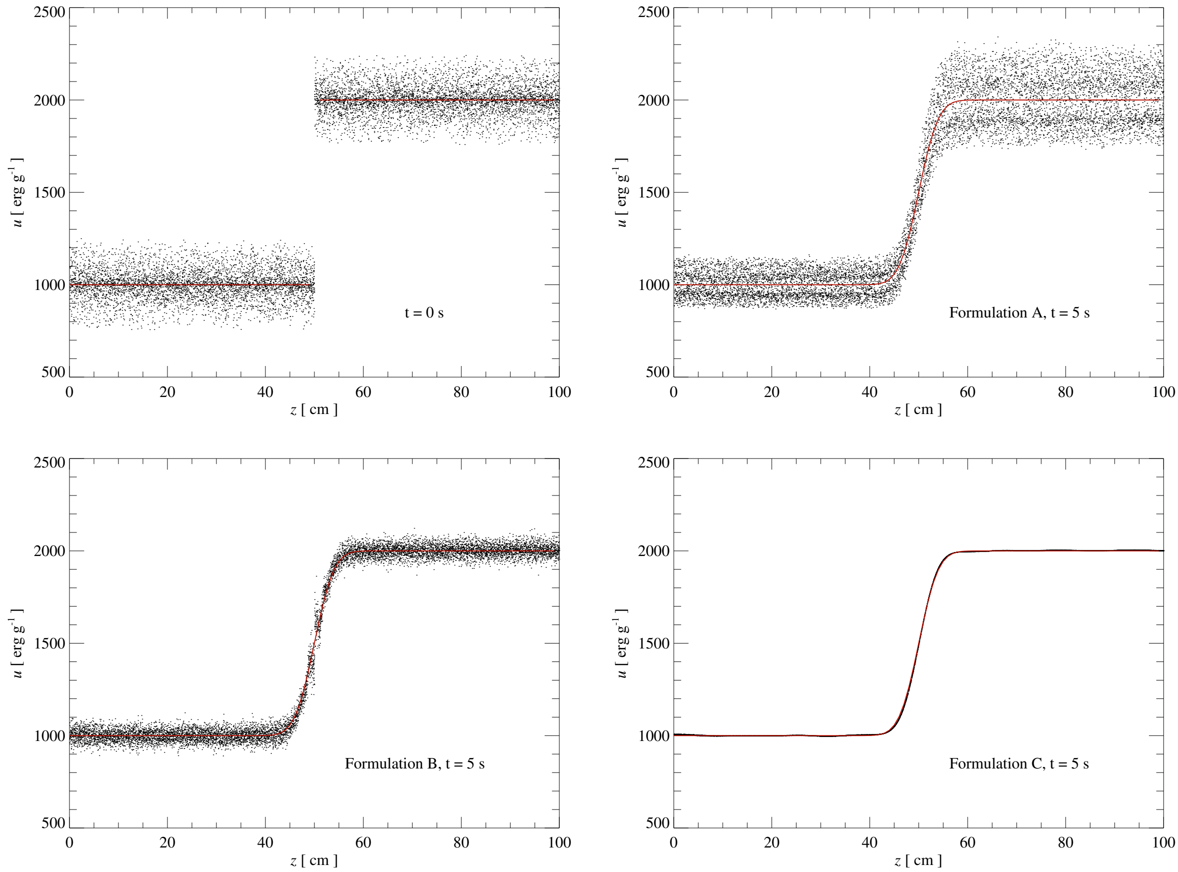

Figure 3.2.: Comparison of the numerical stability of the SPH discretisation scheme when different formulations for the conduction equation (3.22) are used. The top left panel shows the initial conditions for the simple conduction problem considered in Fig. 3.1, but perturbed with artificial Gaussian noise in the temperature field. The top right panel shows the evolved state after 5 sec when formulation (A) is employed, where the individual particle temperatures are used directly. The lower left panel compares this with formulation (B), where the temperatures on the right hand-side of equation (3.22) are taken to be kernel interpolants of the temperature field. Finally, the bottom right panel gives the result for formulation (C), which represents a mixed scheme that uses both the individual temperatures of particles, and the smoothed temperature field. This scheme proves to be the most robust against local noise, which is quickly damped away.

We discussed previously that we can either use the particle values of the temperatures (or entropy) in the right-hand-side of equation (3.22), or kernel interpolants thereof. Here we compare the following different choices with each other:

(A) Basic formulation: Use particle values A_i and A_j.

(B) Smoothed formulation: Use $\overline{A}_i$ and $\overline{A}_j$.

(C) Mixed formulation: Use A_i and $\overline{A}_j$.

The mixed formulation (C) may at first seem problematic, because its pair-wise antisymmetry is not manifest. However, since we use equation (3.24) to exchange heat between particles, conservation of thermal energy is ensured also in this case. When all particles have equal timesteps, formulation (C) would correspond to an arithmetic average of (A) and (B).

In Figure 3.2, we compare the result obtained for these three formulations after a simulation time of 5 sec. The artificially perturbed initial conditions are shown in the top left panel. Interestingly, while all three different formulations are able to recover the analytic solution in the mean, they show qualitatively different behaviour with respect to the imprinted noise. When the intrinsic particle values for the temperatures are used (top right panel), very large pair-wise gradients on small scales occur that induce large heat exchanges. As a result, the particles oscillate around the mean, maintaining a certain rms-scatter which does not reduce with time, i.e. an efficient relaxation to the medium temperature does not occur. Note that the absolute size of the scatter is larger in the hot part of the slab. This is a result of the timestep criterion (3.25), which manages to hedge the rms-noise to something of order $\sim \alpha T$. Reducing the timestep parameter α can thus improve the behaviour, while simultaneously increasing the computational cost significantly. For coarse timestepping (or high conductivities) the integration with this method can easily become unstable.

Formulation (B), which uses the smoothed kernel-interpolated temperature field for both particles in each pair, does significantly better in this respect (bottom left panel). However, the particle temperatures only very slowly approach the local mean value and hence the analytical solution in this case. This is because the smoothing here is quite efficient in eliminating the small-scale noise, meaning that a deviation of an individual particle's temperature from the local mean is decaying only very slowly.

The mixed formulation (C), shown in the bottom right, obviously shows the best behaviour in this test. It suppresses noise quickly, matches the analytical solution very well, and allows the largest timesteps of all schemes we tested. In this formulation, particles which have a large deviation from the local average temperature try to equalise this difference quickly, while a particle that is already close to the mean is not 'pulled away' by neighbours that have large deviations. Apparently, this leads to better behaviour than for schemes (A) and (B), particularly when individual timesteps are used. We hence choose formulation (C) as our default method.

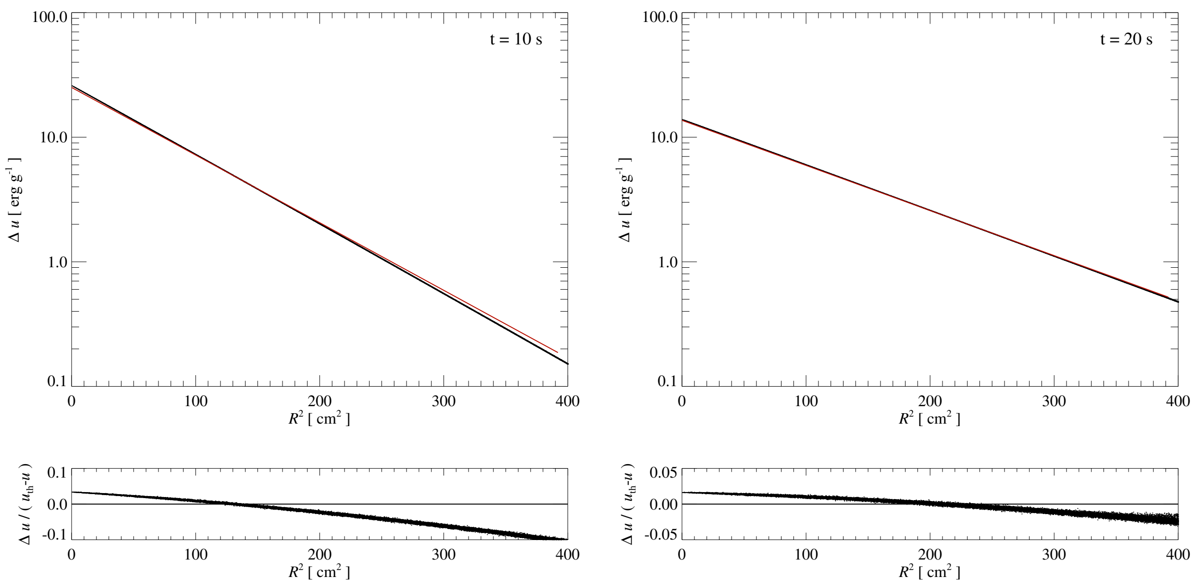

Figure 3.3.: Time evolution of the temperature field in an elementary three-dimensional conduction problem, displayed at two different times. We here consider the spreading of a narrow Gaussian temperature profile, which corresponds to the Green's function of the conduction problem for constant conductivity. Dots show the specific energies of individual simulation particles, while the solid line marks the analytical result. Relative deviations are shown in the lower panels. The numerical result maintains the Gaussian profile very well at all times. At early times, when the profile is sampled with few particles, a small reduction in the effective speed of conduction is seen, which however becomes increasingly unimportant at later times.

3.3.2. Conduction in a three-dimensional problem

As a simple test of conduction in an intrinsically three-dimensional problem, we consider the temporal evolution of a point-like thermal energy perturbation. The time evolution of an initial δ-function is given by the three-dimensional Green's function for the conduction problem,

$$G(x, y, z, t) = \frac{1}{(4\pi\alpha t)^{3/2}} \exp\left(-\frac{x^2 + y^2 + z^2}{4\alpha t}\right), \tag{3.27}$$

where $c_v = u/T$ is the heat capacity. We again consider a solid material, realized with a glass configuration of 50^3 simulation particles with a mass of 1 g each and a mean particle spacing of 1 cm. We choose a conductivity of $\kappa c_v = 1\,\mathrm{cm}^2\,\mathrm{s}^{-1}$, as before. We give the material a specific energy per unit mass of $u_0 = 1000\,\mathrm{erg\ g}^{-1}$, and add a perturbation of 10000.0 erg $\mathrm{cm}^3\,\mathrm{g}^{-1} \times G(x, y, z, t_0 = 10\ \mathrm{sec})$. These initial conditions correspond to a δ-function perturbation that has already evolved for a brief period; this should largely eliminate timing offsets that would arise in the later evolution if we let the intrinsic SPH smoothing wash out a true initial δ-function.

Figure 3.3 shows the specific energy profile after evolving the conduction problem for an additional 10 or 20 seconds, respectively. In the two bottom panels, we show the relative deviation from the analytic solution. Given that quite coarse timestepping was used for this problem (about ~ 32 timesteps for 20 sec), the match between the theoretical and numerical solutions is quite good. Even at a radial distance of 20 cm, where the Gaussian profile has dropped to less than one hundredth of its central amplitude, relative deviations are at around 10 percent for $t = 20$ sec and below 3 percent at $t = 30$ sec. Note however that at all times the numerical solution maintains a nice Gaussian shape so that the deviations can be interpreted as a small modification in the effective conductivity. We then see that at late times, when the temperature gradients are resolved by more particles, the SPH estimate of the conductivity becomes ever more accurate.

3.4. Spherical models for clusters of galaxies

Observed temperature profiles of clusters of galaxies are often characterised by a central decline of temperature, while otherwise appearing fairly isothermal over the measurable radial range. Provided the conductivity is non-negligible, there should hence be a conductive heat flux into the inner parts, which would then counteract central cooling losses. Motivated by this observation, Zakamska & Narayan (2003) (ZN henceforth) have constructed simple analytic models for the structure of clusters, invoking as a key assumption a local equilibrium between conduction and cooling. Combined with the assumption of hydrostatic equilibrium and spherical symmetry, they were able to quite successfully reproduce the temperature profiles of a number of observed clusters.

We here use the model of ZN as a test-bed to check the validity of our conduction modelling in a realistic cosmological situation. In addition, the question for how long the ZN solution can be maintained is of immediate interest, and we address this with our simulations of spherical clusters as well.

For definiteness, we briefly summarise the method of ZN for constructing a cluster equilibrium model. The cluster is assumed to be spherically symmetric, with the gas of density $\rho(r)$ and pressure $P(r)$ being in hydrostatic equilibrium, i.e.

$$\frac{1}{\rho}\frac{\mathrm{d}P}{\mathrm{d}r} = -\frac{\mathrm{d}\Phi}{\mathrm{d}r}, \tag{3.28}$$

where the gravitational potential Φ is given by

$$\frac{1}{r^2}\frac{\mathrm{d}}{\mathrm{d}r}\left(r^2\frac{\mathrm{d}\Phi}{\mathrm{d}r}\right) = 4\pi G\left(\rho_{\mathrm{DM}} + \rho\right). \tag{3.29}$$

The dark matter density $\rho_{\mathrm{DM}}(r)$ is described by a standard NFW (Navarro, Frenk & White 1996) halo, optionally modified by ZN with the introduction of a small softened dark matter core. The structure of the dark halo can then be fully specified by the virial radius r_{200}, defined as the radius enclosing a mean overdensity of 200 with respect to the critical density, and a scale length r_s.

The radial heat flux F due to electron conduction is given by

$$F = -\kappa\frac{\mathrm{d}T}{\mathrm{d}r}, \tag{3.30}$$

where the conductivity κ is taken to be a constant fraction of the Spitzer value. In order to balance local cooling losses, we require

$$\frac{1}{r^2}\frac{\mathrm{d}}{\mathrm{d}r}\left(r^2 F\right) = -j, \tag{3.31}$$

where j is describing the local gas cooling rate. If cooling is dominated by thermal bremsstrahlung, j can be approximated as

$$j = 2.1\times 10^{-27} n_e^2\, T^{1/2}\,\mathrm{ergs\ cm^{-3}s^{-1}}. \tag{3.32}$$

The electron number density n_e herein correlates with the gas density ρ and depends on the hydrogen mass fraction X we assume for the primordial matter. With a proton mass of m_p, it equals $n_e = \rho(X + 1)/(2m_p)$. Following ZN, we use this simplification in setting up our cluster models.

Equations (3.28) to (3.32) form a system of differential equations that can be integrated from inside out once appropriate boundary conditions are specified. We adopt the values for central gas density and temperature, total dark matter mass, and scale radius determined by ZN for the cluster A2390 such that the resulting temperature profile matches the observed one well in the range $0 \leq r \leq R_{\mathrm{out}}$, where R_{out} was taken to be $2\,r_s$.

Integrating the system of equations out to R_{out}, we obtain a result that very well matches that reported by ZN. However, we also need to specify the structure of the cluster in its outer parts in order to be able to simulate it as an isolated system. ZN simply assumed this part to be isothermal at the temperature $T_{\mathrm{out}} = T(R_{\mathrm{out}})$, thereby implicitly assuming that the equilibrium condition between cooling and conduction invoked for the inner parts is not valid any more. It is a bit unclear why such a sudden transition should occur, but the alternative assumption, that equation (3.31) holds out to the virial radius, clearly leads to an unrealistic global temperature profile. In this case, the temperature would have to monotonically increase out to the outermost radius. Also, since the cumulative radiative losses out to a radius r have to

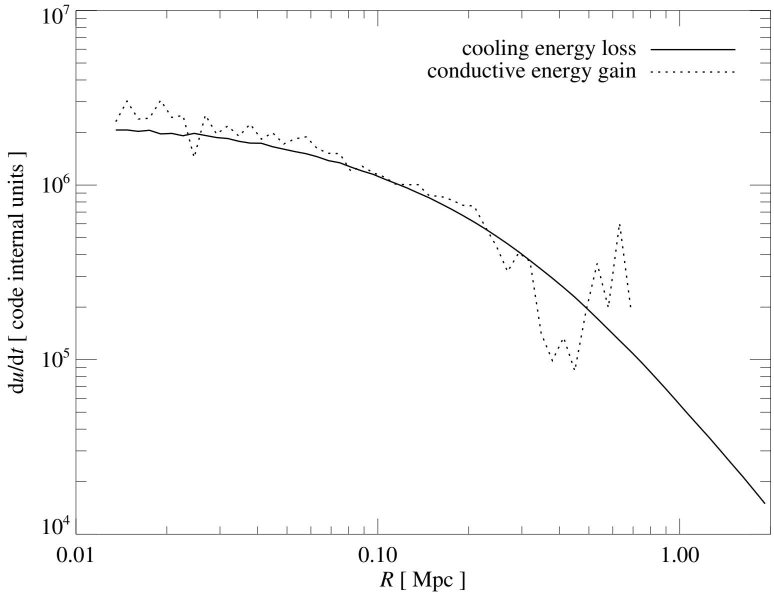

Figure 3.4.: Local cooling (solid line) and conductive heating rates (dotted line) as a function of radius in our model for the cluster A2390, after a time of $t = 0.15$ Gyr. It is seen that both energy transfer rates cancel each other with reasonable accuracy.

be balanced by a conductive heat flux of equal magnitude at that radius, the heat flux also monotonically increases, such that all the energy radiated by the cluster would have to be supplied to the cluster at the virial radius.

We nevertheless examined both approaches, i.e. we construct cluster models where we solve equations (3.28)-(3.32) for the whole cluster out to a radius of r_{200}, and secondly, we construct initial conditions where we follow ZN by truncating the solution at $2\,r_s$, continuing into the outer parts with an isothermal solution that is obtained by dropping equations (3.30) and (3.31). Since conduction may still be important at radii somewhat larger than $2\,r_s$, these two models may hence be viewed as bracketing the expected real behaviour of the cluster in a model where cooling is balanced by conduction.

For the plasma conductivity, we assumed a value of $0.3\,\kappa_{sp}$, as proposed by ZN in their best-fit solution for A2390. Note that this value implies that a certain degree of suppression of conduction by magnetic fields is present, but that this effect is (perhaps optimistically) weak, corresponding to what is expected for chaotically tangled magnetic fields (Narayan & Medvedev 2001).

Having obtained a solution for the static cluster model, we realized it as 3D initial conditions for GADGET. We used 2×10^5 gas particles with a total baryonic mass of around 8.6×10^{14} $M_\odot$. For simplicity, we described the NFW dark matter halo of mass $2.4 \times 10^{15}\,M_\odot$ as a static potential. We then simulated the evolution of the gas subject to self-gravity (with a gravitational softening length of 3 kpc), radiative cooling, and thermal conduction, but without allowing for star formation and associated feedback processes.

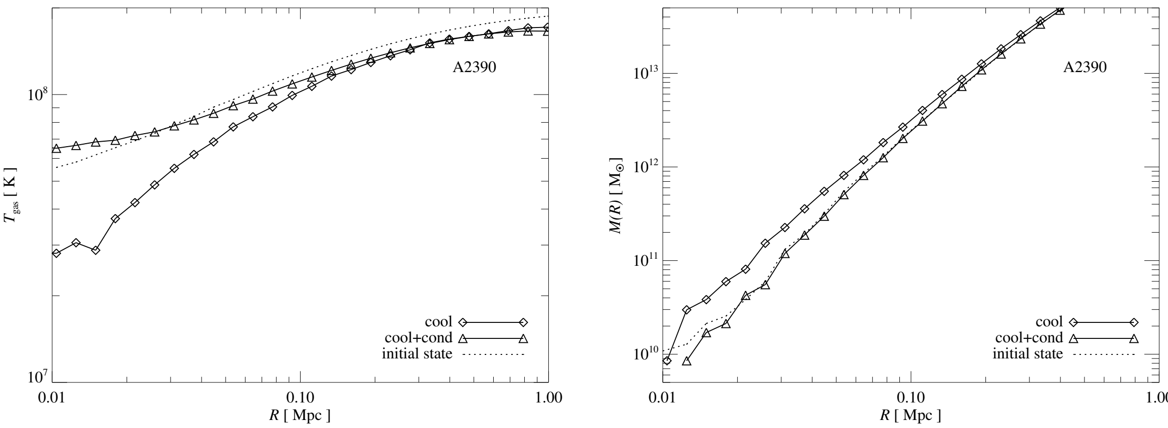

Figure 3.5.: Temperature profile (left) and cumulative mass profile (right) of our model for the cluster A2390, after a simulated time of 0.6 Gyr. We compare simulations with (triangles) and without (diamonds) thermal conduction using a conductivity of $0.3\,\kappa_{\rm sp}$. It is seen that without conduction, the inner regions of the cluster cool down significantly, causing mass to sink towards the centre as central pressure support is partially lost. If thermal conduction is included, the central cooling losses are offset by conductive heating from outer regions, preventing any significant change of the baryonic mass profile. In fact, in this case we even observe a slow secular evolution towards higher temperature in the inner parts.

By construction, we expect that thermal conduction will be able to offset radiative cooling for these initial conditions, at least for some time. This can be verified in Figure 3.4, where we plot the local cooling rate and conductive heating rate as a function of radius. Indeed, at time 0.15 Gyr, after a brief initial relaxation period, the two energy transfer rates exhibit the same magnitude and cancel each other with good accuracy. This represents a nice validation of our numerical implementation of thermal conduction with the temperature-dependent Spitzer-rate.

As the simulation continues, we see that the core temperature of the cluster slowly drifts to somewhat higher temperature. A secular evolution of some kind is probably unavoidable, since the balance between cooling and conductive heating cannot be perfectly static. The cluster of course still loses all the energy it radiates, which eventually must give rise to a slow quasi-static inflow of gas, and a corresponding change of the inner structure of the cluster. Because of the different temperature dependences of cooling and conductive heating, it is also not clear that the balance between cooling and conductive heating represents a stable dynamical state. While a stability analysis by ZN and Kim & Narayan (2003) suggests that thermal instability is sufficiently suppressed in models with conduction, Soker (2003) argues that local perturbations in the cooling flow region will grow to the non-linear regime rather quickly and that a steady solution with a constant heat conduction may therefore not exist.

In any case, it is clear that the inclusion of conduction strongly reduces central mass drop out due to cooling. This is demonstrated explicitly in Figure 3.5, where we show the temperature and cumulative baryonic mass profiles of the cluster after a time of 0.6 Gyr. We compare these profiles also to an identical simulation where conduction was not included. Unlike the conduction run, this cooling-only simulation shows a very substantial modification of its temperature profile in the inner parts, where the core region inside $\sim$ 0.1 Mpc becomes much colder than the initial state. We can also see that the cooling-only simulation has seen substantial baryonic inflow as a result of central mass drop-out. Within 0.6 Gyr, the baryonic mass enclosed in a sphere with radius 50 kpc has increased by 86 percent in this simulation, clearly forming a cooling flow. This contrasts strongly with the run that includes conduction, where beyond a cental distance of $\sim$ 0.02 Mpc, there is no significant difference in the cumulative mass profile between $t = 0$ and $t = 0.6$ Gyr.

We also checked that runs with a reduced conductivity show a likewise reduced effect, suppressing the core cooling and matter inflow to a lesser extent than with our default model with $0.3\,\kappa_{\rm sp}$.

Finally, we note that the results discussed here are quite insensitive to whether we set-up the initial conditions with an isothermal outer part, or whether we continue the equilibrium solution to the virial radius. There is only a small difference in the long term evolution of the solution.

The model presented here helps us to verify the robustness of our conduction implementation when a temperature dependent conductivity is used, but it does not account for the time dependence of conduction expected in the cosmological context. The static, spherically symmetric construction does not reflect the hierarchical growth of clusters that is a central element of currently favoured cosmologies. To be able to make reliable statements about the effects of thermal conduction on galaxy clusters, one therefore has to trace their evolution from high redshift to the present, which is best done in full cosmological simulations. Here, the hierarchical growth of clusters implies that the conductivity is becoming low early on, when the ICM temperature is low, and becomes only large at late times when the cluster forms.

3.5. Cosmological cluster simulations

In this section, we apply our new numerical scheme for the treatment of thermal conduction in fully self-consistent cosmological simulations of cluster formation. We will in particular compare the results of simulations with and without conduction, both for runs that follow only adiabatic gas-dynamics, and runs that also include radiative cooling of gas. While it is beyond the scope of this work to present a comprehensive analysis of the effects of conduction in cosmological simulations, we here want to investigate a set of small fiducial runs in order to further validate the stability of our method for real-world applications, and secondly, to give a first flavour of the expected effects of conduction in simulated clusters. A more detailed analysis of cosmological implications of conduction is presented in a companion study (Dolag et al. 2004a).

We focus on a single cluster, extracted from the 'GIF' simulation (Kauffmann et al. 1999) of the ΛCDM model, and resimulated using the "zoomed initial conditions" technique (Tormen et al. 1997). To this end, the particles that make up the cluster at the present time are traced back to their original coordinates in the initial conditions. The Lagrangian region of the cluster identified in this way is then resampled with particles of smaller mass, and additional small-scale perturbations from the CDM power spectrum

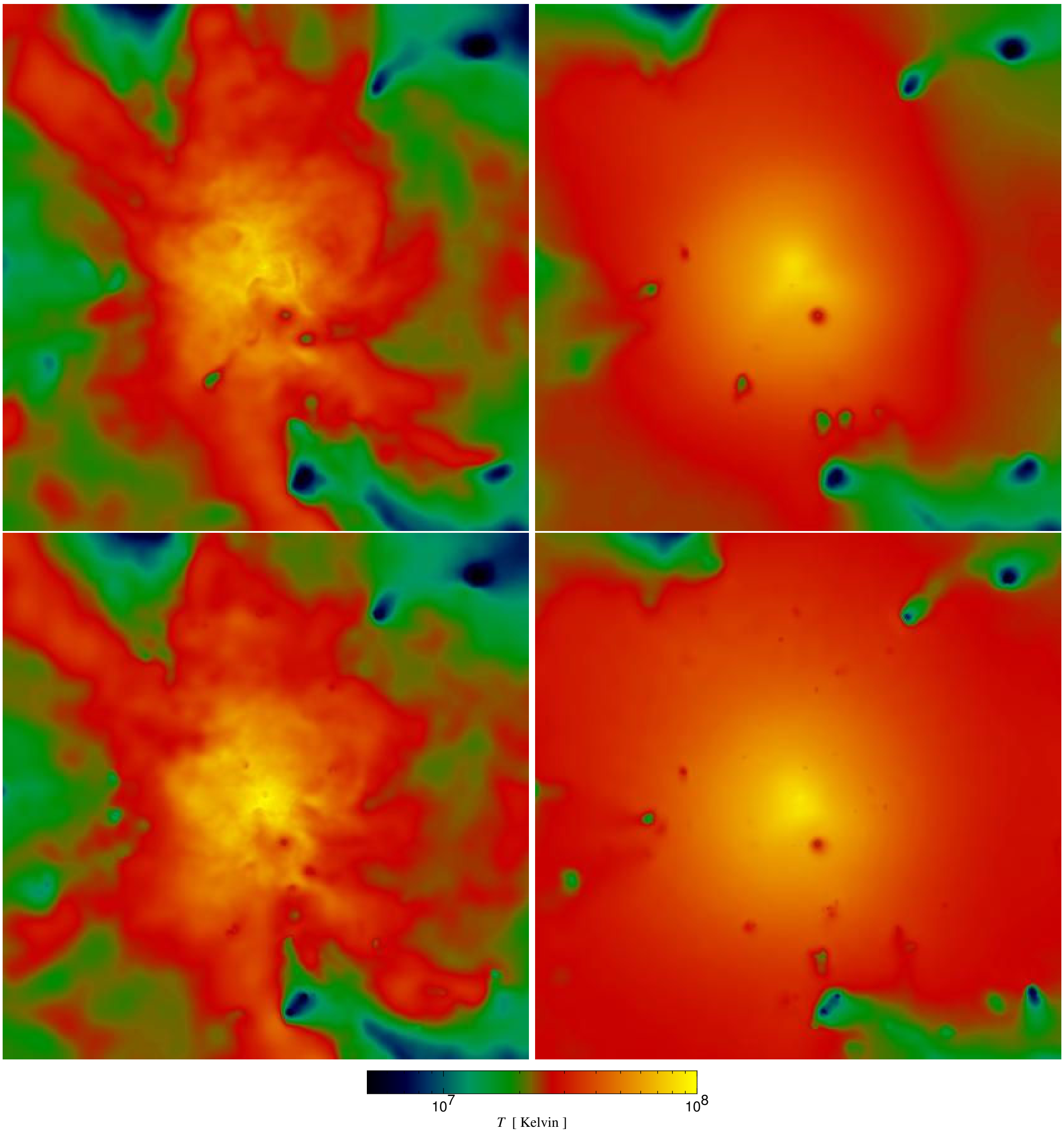

Figure 3.6.: Projections of mass-weighted temperature for our cluster simulations at $z = 0.13$. From the top to the bottom row, we show the same cluster but simulated with different physics: Adiabatic gasdynamics only, adiabatic plus thermal conduction, radiative cooling and star formation, and finally, cooling, star formation and conduction. Each panel displays the gas contained in a box of side-length 8.6 Mpc centred on the cluster. Full Spitzer conductivity was assumed.

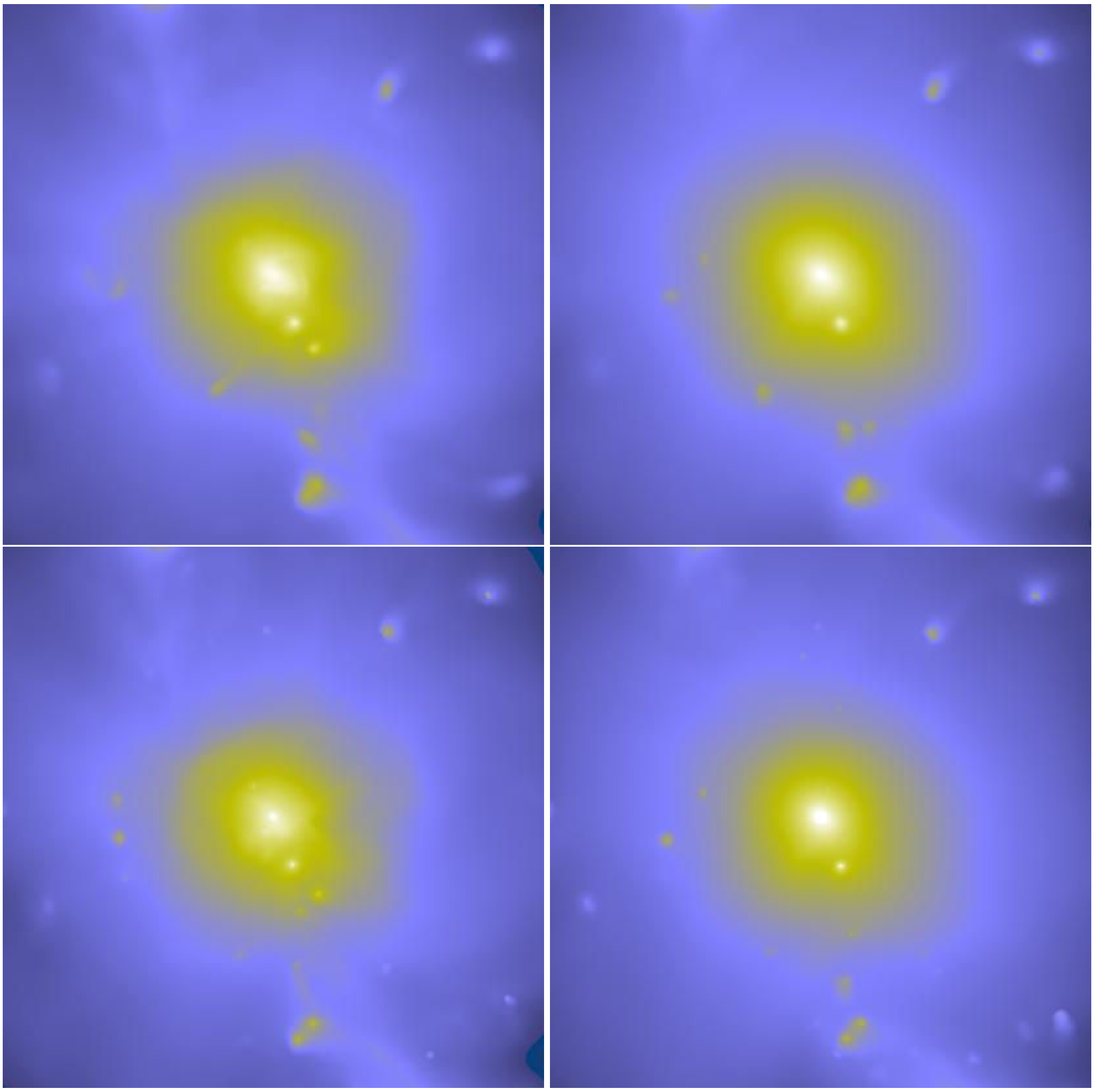

Figure 3.7.: Projections of X-ray emissivity for the cluster simulations presented in figure 3.6.

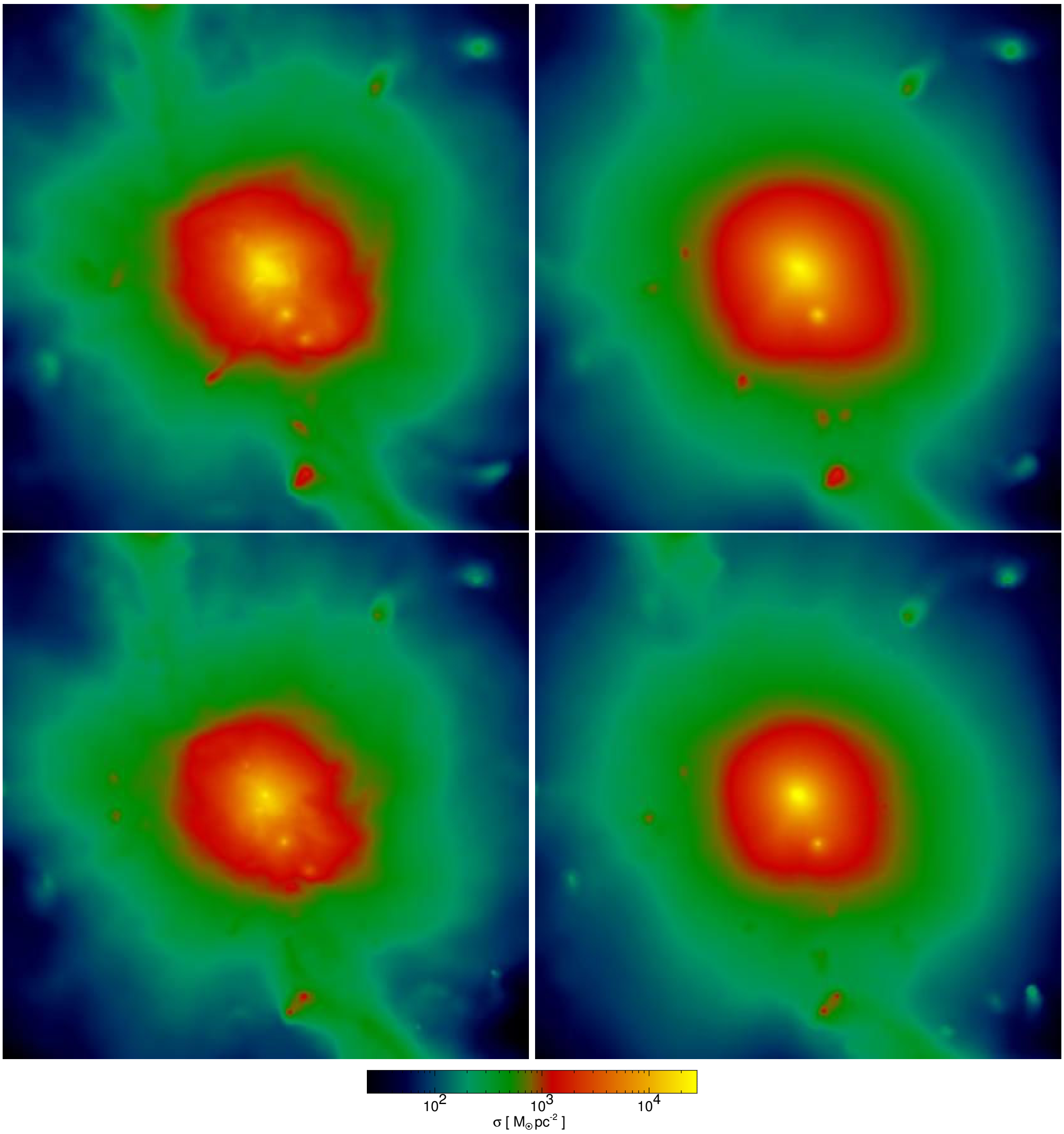

Figure 3.8.: Projections of gas mass density for the cluster simulations presented in figure 3.6.

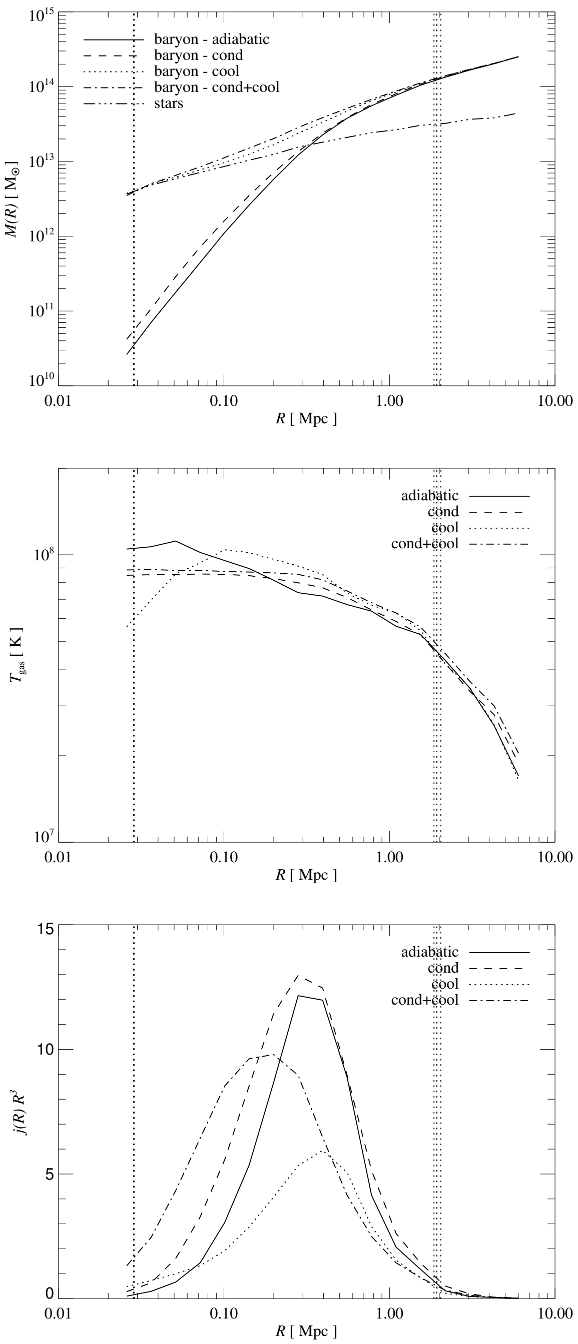

Figure 3.9.: Cumulative baryonic mass profile (top left), temperature profile (top right) and the resulting X-ray emissivity profile (bottom) of the simulated cluster at $z = 0.13$. In each panel, we compare the same cluster simulation run with different physical models for the gas: Adiabatic gasdynamics only, adiabatic plus thermal conduction, radiative cooling and star formation without conduction, and finally, cooling, star formation and conduction. For the models including conduction, full Spitzer conductivity was assumed. Note that the X-ray emissivity is plotted such that the area under the curve is proportional to the total bolometric X-ray luminosity.

are added appropriately. Far away from the cluster, the resolution is progressively degraded by using particles of ever larger mass.

The cluster we selected has a virial mass of $1.1\times10^{15}\,\mathrm{M}_{\odot}$. It is the same cluster considered in the high-resolution study of Springel et al. (2001), with our mass resolution corresponding to their S1 simulation, except that we split each of the ~ 450000 high resolution dark matter particles into a gas and a dark matter particle (assuming $\Omega_b = 0.04$), yielding a gas mass resolution of $8.4\times10^{9}\,\mathrm{M}_{\odot}$. The boundary region was sampled with an additional 3 million dark matter particles. We then evolved the cluster forward in time from a starting redshift $z = 30$ to the present, $z = 0$, using a comoving gravitational softening length of 20 kpc.

We consider 4 different simulations of the cluster, each with different physical models for the gas: (1) Adiabatic gasdynamics only, (2) adiabatic gas and conduction, (3) radiative cooling and star formation without conduction, and finally, (4) radiative cooling, star formation and conduction. The simulations with cooling and star formation use the sub-resolution model of Springel & Hernquist (2003a) for the multi-phase structure of the ISM (without including the optional feedback by galactic winds offered by the model). In the two runs with conduction, we adopt the full Spitzer rate for the conductivity. While this value is unrealistically large for magnetised clusters, it serves our purpose here in highlighting the effects of conduction, given also that our cluster is not particularly hot, so that effects of conductivity can be expected to be weaker than in very rich clusters.

In Figure 3.8, we show projections of the mass-weighted temperature, X-ray emissivity, and gas mass density for all four simulations. Each panel displays the gas contained in a box of side-length 8.6 Mpc centred on the cluster. Comparing the simulations with and without conduction, it is nicely seen how conduction tends to wipe out small-scale temperature fluctuations. It is also seen that the outer parts of the cluster become hotter when conduction is included.

These trends are also borne out quantitatively when studying radial profiles of cluster properties in more detail. In Figure 3.9, we compare the cumulative baryonic mass profile, the temperature profile, and the radial profile of X-ray emission for all four simulations. Note that the innermost bins, for $R < 30\,\mathrm{kpc}$, may be affected by numerical resolution effects. Interestingly, the temperature profiles of the runs with conduction are close to being perfectly isothermal in the inner parts of the cluster. While this does not represent a large change for the adiabatic simulation, which is close to isothermal anyway, the simulation with radiative cooling is changed significantly. Without conduction, the radiative run actually shows a pronounced rise in the temperature profile in the range of $100 - 200\,\mathrm{kpc}$, as a result of compressional heating when gas flows in to replace gas that is cooling out of the ICM in a cooling flow. Only in the innermost regions, where cooling becomes rapid, we see a distinct drop of the temperature. Interestingly, conduction eliminates this feature in the temperature profile, by transporting the corresponding heat energy from the maximum both to parts of the cluster further out and to the innermost parts. The latter effect is probably small, however, because a smooth decline in the temperature profile in the inner parts of the cluster, as present in the ZN model, does not appear in the simulation. As a consequence, a strong conductive heat flow from outside to inside cannot develop.

Conduction may also induce changes in the X-ray emission of the clusters, which we show in the bottom panel of Figure 3.9. Interestingly, the inclusion of conduction in the adiabatic simulation has a negligible effect on the X-ray luminosity. This is because in contrast to previous suggestions (Loeb 2002), the cluster does not lose a significant fraction of its thermal energy content to the outside intergalactic medium, and the changes in the relevant part of the gas and temperature profile are rather modest. We do note however that the redistribution of thermal energy within the cluster leads to a substantial increase of the temperature of the outer parts of the cluster.

For the simulations with cooling, the changes of the X-ray properties are more significant. Interestingly, we find that allowing for thermal conduction leads to a net *increase* of the bolometric luminosity of our simulated cluster. The panel with the cumulative baryon mass profile reveals that conduction is also ineffective in significantly suppressing the condensation of mass in the core regions of the cluster. In fact, it may even lead to the opposite effect. We think this behaviour simply occurs because a temperature profile with a smooth decline towards the centre, which would allow the conductive heating of this part of the cluster, is not forming in the simulation. Instead, the conductive heat flux is pointing primarily from the inside to the outside, which may then be viewed as an additional “cooling” process for the inner cluster regions.

It is interesting to note that in spite of the structural effects that thermal conduction has on the ICM of the cluster, it does not affect its star formation history significantly. In the two simulations that include cooling and star formation, the stellar component of the mass profile (Figure 3.9) does not show any sizeable difference between the run including thermal conduction and the one without it. This does not come as surprise as 90% of the stellar content of the cluster has formed before a redshift of $z = 0.85$. At these early times, the temperature of the gas in the protocluster was much lower, such that conduction was unimportant. In fact, for that reason, the stellar mass profiles for both simulation runs coincide.

In summary, our initial results for this cluster suggest that conduction can be important for the ICM, provided the effective conductivity is a sizable fraction of the Spitzer value. However, the interplay between radiative cooling and conduction is clearly complex, and it is presently unclear whether temperature profiles like those observed can arise in self-consistent cosmological simulations. We caution that one should not infer too much from the single object we examined here. A much larger set of cluster simulations will be required to understand this topic better.

3.6. Conclusions

Hot plasmas like those found in clusters of galaxies are efficiently conducting heat, unless electron thermal conduction is heavily suppressed by magnetic fields. Provided the latter is not the case, heat conduction should therefore be included in hydrodynamical cosmological simulations, given, in particular, that conduction could play a decisive role in moderating cooling flows in clusters of galaxies. Such simulations are then an ideal tool to make reliable predictions of the complex interplay between the nonlinear processes of cooling and conduction during structure formation.

In this study, we have presented a detailed numerical methodology for the treatment of conduction in cosmological SPH simulations. By construction, our method manifestly conserves thermal energy, and we have formulated it such that it is robust against the presence of small-scale temperature noise. We have implemented this method in a modern parallel code, capable of carrying out large, high-resolution cosmological simulations.

Using various test problems, we have demonstrated the accuracy and robustness of our numerical scheme for conduction. We then applied our code to a first set of cosmological cluster formation simulations, comparing in particular simulations with and without conduction. While these results are preliminary, they already hint that the phenomenology of the coupled dynamics of radiative cooling and conduction is complex, and may give rise to results that were perhaps not anticipated by earlier analytic modelling of static cluster configurations.

For example, we found that conduction does not necessarily reduce a central cooling flow in our simulations; the required smoothly declining temperature profile in the inner cluster regions does not readily form in our cosmological simulations. Instead, the profiles we find are either flat, or have a tendency to slightly rise towards the centre, akin to what is seen in the cooling-only simulations. In this situation, conduction may in fact lead to additional cooling in certain situations, by either transporting thermal energy to the outer parts, or by modifying the temperature and density structure in the relevant parts of the cluster such that cooling is enhanced. This can then manifest itself in an increase of the bolometric X-ray luminosity at certain times, which is actually the case for our model cluster at $z = 0$. Interestingly, we do not find that our cluster loses a significant fraction of its thermal heat content by conducting it to the external intergalactic medium.

In a companion study (Dolag et al. 2004a), we analyse a larger set of cosmological cluster simulations, computed with much higher resolution and with more realistic sub-Spitzer conductivities. This set of cluster allows us to investigate, e.g., conduction effects as a function of cluster temperature and the influence of conduction on cluster scaling relations. While our first results of this work suggest that conduction by itself may not resolve the cooling-flow puzzle, it also shows that conduction has a very strong influence on the thermodynamic state of rich clusters if the effective conductivity is a small fraction of the Spitzer value or more. In future work, it will hence be very interesting and important to understand the rich phenomenology of conduction in clusters in more detail.

The work and results presented in this chapter have been published on the Monthly Notices of the Royal Astronomy Society by M. Jubelgas, V. Springel and K. Dolag in 2004, MNRAS 351, p. 423.

It may be true, that as Francis Thompson noted, 'Thou canst not stir a flower without troubling a star', but in computing the motion of stars and planets, the effects of flowers do not loom large. It is the disregarding of the effect of flowers on stars that allows progress in astronomy. Appropriate abstraction is critical to progress in science.

Herman Shugart

4 Cosmic ray feedback in hydrodynamical simulations of galaxy formation

4.1. Introduction

In recent years, the ΛCDM model has emerged as a highly successful 'concordance' model for cosmological structure formation. It conjectures that the dominant mass component in the universe consists of cold dark matter, and that a cosmological constant or dark energy field adds sufficient energy density to yield a spatially flat spacetime. The model is impressively successful in matching observational data on a large range of scales and epochs, including the cosmic microwave background fluctuations (e.g. Spergel et al. 2003), galaxy clustering (e.g. Tegmark et al. 2004, Cole et al. 2005), cosmic flows in the present universe (e.g. Willick et al. 1997, Hudson et al. 2004), and observational data on distant supernovae (Riess et al. 1998, Perlmutter et al. 1999).

The dynamics of dark matter in the ΛCDM model is now well understood and can be followed with high accuracy in numerical simulations (Power et al. 2003, Navarro et al. 2004, Heitmann et al. 2005). However, the baryonic processes that regulate the formation of the luminous components of galaxies are still posing many challenges for our theoretical understanding. Direct hydrodynamical simulations that follow the baryonic gas as well as the dark matter, face a number of 'small-scale' problems. In particular, simulations of this kind are still struggling to properly account for feedback mechanisms related to star formation. They typically suffer from an 'overcooling catastrophe' and tend to produce far too many stars, unless effects like galactic outflows are included in a phenomenological way (e.g. Springel & Hernquist 2003b). Other problems that perhaps run still deeper are that the forming galaxies are too concentrated (e.g. Abadi et al. 2003) and fail to reproduce the observed shape of the luminosity function of galaxies in detail (Murali et al. 2002, Nagamine et al. 2004).

By invoking strong feedback processes, semi-analytic models of galaxy formation can overcome many of these problems and offer explanations for a wide array of galaxy properties (White & Frenk 1991, Kauffmann et al. 1993, Baugh et al. 1998, Somerville & Primack 1999, Cole et al. 2000, Croton et al. 2006). While this supports the notion that feedback is crucial for the regulation of galaxy formation, it is unclear whether the physical nature of the feedback processes is correctly identified in the present semi-analytic models, or whether they merely give a more or less correct account of the consequences of this feedback. Direct hydrodynamic simulations can be used to lift this ambiguity and to offer more direct constraints for the physical processes at work.

Most current models of galaxy formation include feedback effects caused by supernova explosions and a photoionizing background, and more recently have considered quasar and radio activity by AGN as well (e.g. Di Matteo et al. 2005, Sijacki & Springel 2006). However, perhaps surprisingly, magnetic fields and non-thermal pressure components from cosmic rays have received comparatively little attention thus far (with notable exceptions, including Kang et al. 1996, Miniati 2001, Miniati et al. 2001, Miniati 2002, Ryu & Kang 2003, 2004), despite the fact that cosmic rays are known to contribute substantially to the pressure in the ISM of our own Galaxy. This is probably (at least in part) due to the complexity of cosmic ray dynamics, which, when coupled to the process of galaxy formation, is very hard to describe analytically. Even when numerical methods are invoked, the cosmic ray physics is so involved that a number of simplifying approximations is required to make it tractable in a cosmological simulation setting, as we discuss here.

In this study, we introduce the first cosmological code for galaxy formation that treats cosmic rays in a self-consistent way during the structure formation process. The principal approach used for capturing the cosmic ray physics has been laid out in Enßlin et al. (2006), where we introduce a number of approximations to reduce the complexity of the problem. Basically, we model the cosmic ray population of each fluid element as a power law spectrum in particle momentum, characterized by amplitude, momentum cut-off, and a fixed slope. The model accounts for adiabatic advection of cosmic rays, and for injection and loss terms originating from a variety of physical sources. Finally, we also include cosmic ray diffusion. The primary injection mechanisms we consider are those of supernova shocks and diffusive shock acceleration at structure formation shock waves. The efficiency of the latter is a sensitive function of the Mach number of the shock. Therefore we have also developed an on-the-fly shock finder for SPH calculations, described in detail in Pfrommer et al. (2006).

In this study, we use the theoretical cosmic ray model of Enßlin et al. (2006) and cast it into a numerical formulation that we implement in the cosmological TreeSPH code GADGET-2 (Springel et al. 2001, Springel 2005). We discuss our numerical approach in detail, including also various optimizations needed to keep the scheme efficient and robust. Further, we move on to show first results from applications of the model, ranging from isolated galaxies of different sizes, to cosmological simulations of galaxy cluster formation, and of homogeneously sampled boxes. We show that cosmic rays can have a substantial effect on dwarf galaxies, suppressing their star formation considerably. We show that this should leave a noticeable imprint in the luminosity function of galaxies, leading to a shallower faint-end slope.

This chapter is laid out as follows. In Section 2, we give a brief overview over the nature and the properties of the cosmic ray population of the Galaxy, which provides a reference for the basic physical features and effects we are trying to model. We then describe in Section 3 the details of our implementation of cosmic ray physics, based on the SPH simulation framework as introduced in the previous chapters. In Section 4, we discuss the numerical treatment of cosmic ray diffusion. Section 5 discusses a number of test problems, used to verify the validity of results obtained by the code. Further, in Section 6 we describe a first set of simulations of isolated galaxies carried out with the new code. This highlights a number of principal effects found for the model. In Section 7, we extend our analysis to more sophisticated, fully cosmological simulations of structure formation. We consider the formation of both galaxy clusters and dwarf galaxies at high redshift. Finally, Section 8 summarizes our conclusions and gives an outlook for future simulation studies of cosmic ray physics in a cosmological context.

4.2. The nature of cosmic rays

4.2.1. Observations

Cosmic rays, also known as cosmic particles, are relativistic and ultra-relativistic particles originating from outside Earth. Formerly believed to be the result of the decay of radioactive isotopes in the ground, Hess (1912) found that a balloon-mounted detector was measuring an increasing ionizing effect as it climbed to higher altitude, invalidating the existing theory. It could soon be shown that most cosmic ray particles were carrying electric charge, meaning that the measurements are subject to effects from the magnetic field that shields Earth from cosmic rays and the solar wind.

Relativistic protons make up the largest contribution to cosmic rays, but remarkably, the abundances of individual heavy elements can be remarkably high compared to those found in the interstellar medium, up to several orders of magnitude higher for lithium, beryllium and boron (Wiebel-Sooth & Biermann 1999). Also, cosmic ray matter contains elements that are very rare under normal conditions. Isolated neutrons can also appear; their normally quick decay is delayed by a boost of their lifetime due to relativistic time dilatation.

Cosmic ray particles can carry enormous amounts of kinetic energy, often exceeding 10^{20} eV, which is much larger than the proton rest mass of 0.9×10^9 eV. At these energy levels, they are essentially unaffected by gravitational forces, and the only containment they may experience is due to magnetic fields found in galaxies and clusters of galaxies. It has to be noted, however, that at around 3×10^{18} eV, the Larmor radius at which the cosmic ray particles gyrate around magnetic field lines grows too large to trap them inside a galaxy. Cosmic rays in and above this energy regime most likely originate from outside our Galaxy.

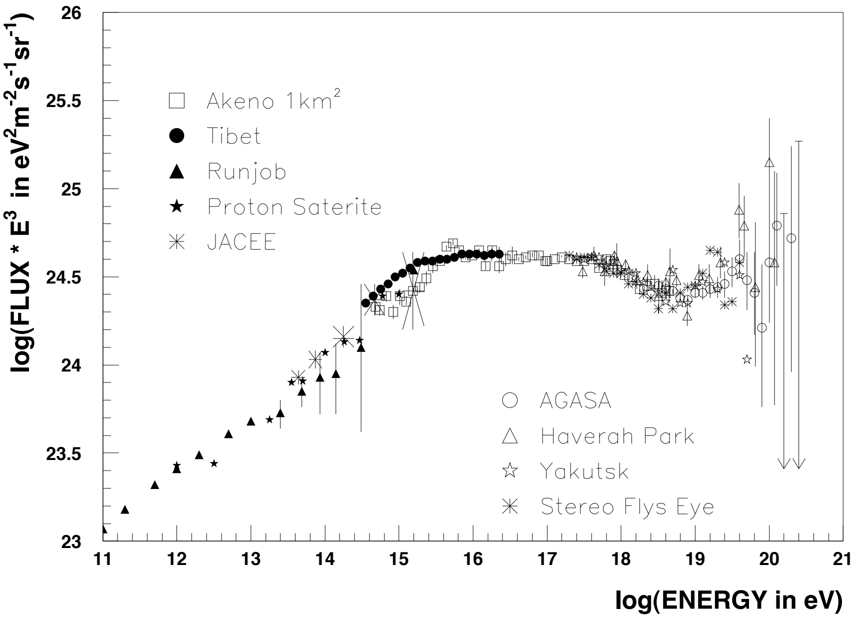

Figure 4.1.: The cosmic ray energy spectrum above 10^{11} eV measured by different experiments. The flux is given in units of events per unit area, time, energy and solid angle and has been multiplied with E^3 to project out the steep gradient and show the "knees" and "ankle" of the spectrum more clearly. (Source: Nagano & Watson (2000))

The energy spectrum of cosmic rays is usually well described by a piecewise power-law and reveals the non-thermal origin of the particles. In measured spectra (see Figure 4.1), it features a spectral index of ~ 2.7 up to the first "knee" at $\sim 5 \times 10^{15}$ eV, then turns to decline at an even steeper rate of ~ 3.1. It is worth noting that both this first knee and a "second knee" that new experiments (Abu-Zayyad et al. 2001) find at $\sim 3 \times 10^{17}$ eV appear to be proportional to the particle charge (Peters 1961) and therefore refer to constant Larmor radii and constant energy levels per nucleon.

At energies above $\sim 5 \times 10^{18}$ eV, Greisen (1966) and Zatsepin & Kuzmin (1966) (usually referred to as GZK) have shown that cosmic rays can be subject to strong losses by inelastic interaction with low energy photons of the CMB. In the rest frame of a cosmic ray proton, these CMB photons carry energies that exceed the rest mass equivalent energy of pions. The production of pions in the collision rest frame is estimated to lead to an energy loss of $\sim 20\%$ every $\simeq 6$ Mpc in the observer frame, and cosmic rays of extragalactic origin in this high energy regime should be strongly suppressed. However, a sizeable fraction of cosmic rays at energies of 10^{20} eV and above (compare Fig. 4.1) is nevertheless found. The explanation for why there is no spectral cutoff observed above the GZK energy threshold is one of today's remaining enigmas related to the nature of cosmic rays.

4.2.2. Physical processes

4.2.2.1. Origin of cosmic rays

The basic mechanism to generate particles at the high energy and momentum levels that are measured for cosmic rays is the acceleration of charged, thermal particles in a strongly shocked plasma (Fermi 1949, 1954), often referred to as Fermi acceleration. Ions and electrons that move faster than the flow in the rest frame of the shock-front can traverse the shock-front repeatedly when they scatter on magnetic irregularities that exist in the stirred plasma on both sides of the shock, and effectively get reflected there. With each passage through the shock compression zone, they gain a fraction of v_{shock}/c in momentum, where v_{shock} is the shock velocity.

Recently, another way of deriving the cosmic ray spectrum generated in shocks has been proposed. In the theory of *diffusive shock acceleration* (Blandford & Ostriker 1978) cosmic ray particles are pictured to be diffusing through the shock front on short time scales, letting them experience multiple iterations of shock acceleration.

In interactions with a turbulent magnetic field, any bulk motion of cosmic ray particles relative to the magnetic field is quickly dispersed, such that the relativistic particles are largely contained by the field. They hence do not travel through space freely, but are instead tightly coupled to the thermal gas by the magnetic field that is frozen to the medium. Hence, despite of their relativistic nature, the influence of cosmic ray particles on gas dynamics can be estimated without having to resort to an explicit treatment of their orbital motion.

Due to the large particle energies, momenta, and their highly relativistic character, cosmic ray particles experience a number of interactions and processes that are either unaccessible or of negligible importance for their thermal counterparts. These processes need to be addressed in any attempt to mimic the effects of cosmic rays on hydrodynamic systems.

4.2.2.2. Synchrotron emission

As pointed out before, cosmic ray particles are subject to the Lorenz-force of the magnetic field encountered in the interstellar and intra-cluster media. Instead of showing the typical Brownian random-walk motion of thermal particles, they gyrate around magnetic field lines at the Larmor radius corresponding to their momentum. Net motions perpendicular to the magnetic field requite a scattering event that triggers a transition to another state in the energy field generated by the magnetic field.

Like with any charged particle, the acceleration that keeps the cosmic ray particles on their helical trajectory also causes the emission of *Bremsstrahlung*. In the case of relativistic particles, the emission of light in the particle rest frame leads to the collimation into radiation coils when observed from the outside. The light inside these coils is subject to a Doppler shift, so the observed photons originally emitted as Bremsstrahlung can carry exceptionally high energies. This observed, relativistically altered form of radiation is commonly referred to as *synchrotron radiation*, deriving from the particle accelerator machine where this kind of radiation has first been observed and analyzed.

In astrophysical observations, synchrotron radiation is found wherever high energy particles interact with magnetic fields, as found in quasars and supernova explosions, for example. For particles moving at near-relativistic velocities, the gyration frequency of a particle in a magnetic field is proportional to its specific charge, and the rate of energy emitted as synchrotron radiation is a function of this gyration frequency. It is obvious that this kind of energy loss process is most effective for relativistic electrons. For heavier charged particles like protons and α particles, it is suppressed.

4.2.2.3. Inverse compton process

In an elastic scattering of an energetic photon on a electron with thermal velocity, the electron can gain energy. The photon, on the other hand, loses energy up to a value that corresponds to a shift in wavelength by the so-called *Compton length* of the scattered particle. This effect, found by Arthur Compton in 1923, served as a ‘smoking gun’ observation that convinced physicists that light could also be pictured as a stream of particles. In the case of a thermal gas, the Compton process leads to a net heating of the gas.

The very same process occurs for cosmic ray particles in their rest frame. They experience scatterings with photons that carry a high energy in this system of reference and receive a momentum transfer accordingly. In the observer’s frame, however, the cosmic ray particle loses energy in the collision, and the interacting photon receives a strong momentum boost in the direction of the cosmic ray particle’s motion. This situation, where the photon is propelled to high energies is called the *inverse Compton process*. It plays a crucial part in generating hard non-thermal radiation observed in high-energy processes.

4.2.2.4. Inelastic collisions

Collisions of particles at sufficiently large energies can result in inelastic events. In the encounter, new particles can be created, either involving a destruction of the original interaction partners, or a partial loss of their kinetic energy. The condition required for these inelastic processes to happen is that the total relativistic mass of the source particles in the collision rest frame must exceed the rest mass of the newly created particle or particles. Often these newly formed particles are short-lived and decay into secondary particles and photons on short timescales. The γ, synchrotron and radio emissions generated in these decay cascades are often used to estimate cosmic ray populations in distant objects like clusters of galaxies.

In their interactions with thermal matter and photons, cosmic ray protons are known to mainly produce pions. Depending on the interaction partner, the required energy or momentum threshold for this process can vary strongly. In collisions with thermal protons, the cosmic ray particle energies required to obtain a rest frame mass of a pion is $\sim 0.78 \times 10^9$ eV, while for pion-creation in a reaction between a cosmic ray particle and a low-energy photon of the cosmic microwave background, the threshold energy is as high as $\sim 5 \times 10^{19}$ eV. Higher energy cosmic ray particles are susceptible to a larger range of inelastic processes, and therefore are subject to faster dissipation by means of inelastic collisions.

4.2.2.5. Coulomb losses

While moving through a gaseous medium, charged particles do not only lose energy by actual collision events, but also are subject to the influence of the electromagnetic field created by the ambient matter. They continuously exchange momentum and energy with the surrounding ions and electrons mediated by the Coulomb force. In a purely thermal plasma, this interaction is statistically balanced, i.e. particles on average gain as much energy as they lose, provided the momentum spectrum has the well-known thermal equilibrium shape.

However, particles that move with an extreme energy compared to the thermal population find themselves losing energy to the charged matter that they pass by, and gradually will have their momenta reduced to thermal levels. This effect is most efficient for cosmic ray particles at low velocities. Highly relativistic particles react slower to the thermalization process due to their shorter interaction time with individual ions of the background matter. It should be noted that not only an ionized plasma causes this kind of energy loss for cosmic ray particles. Even in a neutral gas, the negatively charged electrons can induce this effect, albeit at a largely reduced efficiency, while the positive ions are rendered ineffective due to atomic charge shielding effects.

4.2.3. A model for cosmic rays

The large range of different physical effects acting on the particles of the cosmic ray population make a detailed inclusion in simulations difficult, if not impossible. In principle, a fully general treatment would have to evolve the full momentum distribution function of cosmic ray particles for every fluid element. The high dimensionality of this problem makes this impossible in practice, given the performance of even the newest generation of supercomputers. In addition, cosmic ray particles of different type and momentum are subject to different physical dissipation processes, adding further complications for a numerical treatment of the problem.

As a result, simulation approaches to cosmic ray physics have so far been restricted to post-processing analysis of outputs produced by ordinary hydrodynamic simulations, based on empiric relations to model cosmic ray populations in a post-hoc fashion (e.g. Miniati 2001, Miniati et al. 2001). A significant disadvantage of this approach is that it cannot account for the mutual dynamical influence between thermal and relativistic gas components.

To make fully self-consistent hydrodynamic simulations possible that for the first time include the dynamical effects that a cosmic ray population may cause, we introduce a simplified model for cosmic ray physics. In this model, we represent the cosmic ray population existing in each fluid mass element of the simulation in a way that captures as many physical properties of the cosmic ray population as possible while it on the other hand induces only a moderate computational cost. We aim for a model that is accurate for the in-situ computation of gas-dynamical effects of the cosmic rays, and favor this aspect over an accurate representation of the detailed spectral distribution of the population. For this reason, we will invoke a simplified momentum distribution function of cosmic ray particles, guided by adiabatic invariants and the fundamental principles of energy and particle-number conservation.

4.2.3.1. CR population

Protons contribute the largest mass fraction to the cosmic ray population. Yet, α-particles and heavier ions make up a sizeable part of the cosmic rays, with abundances exceeding those found in thermal interstellar and intergalactic medium. However, taking the heavy ions explicitly into account in our cosmic ray model would require either a self-consistent or phenomenologically motivated enrichment model that resolves the different nuclei in the acceleration mechanisms. Also, there would be substantial additional computational cost created by the need to iterate through all particle families in every simulation step.

Instead, the model we present here restricts itself to the effects of protons and α-particles, where the information on the latter is absorbed into the proton treatment. For all processes presented, this is a reasonable approximation. In hadronic interactions, the binding energy of the α nuclei of a few MeV can be taken to be of minor importance when considering the kinetic energies of the particles on the GeV scale. On the other hand, for Coulomb cooling, due to the proportionality of the process' efficiency to the square of the ion's charge, the effect on the four nucleons of the α particle each is equal to the energy loss that an individual proton would feel.

4.2.3.2. Confinement

Cosmic ray particles do not travel freely through space. Rather, they are subject to the strong Lorenz force of the magnetic field. It keeps cosmic ray particles of energies less than $\sim 3 \times 10^{18}$ eV tightly bound in our Galaxy. In fact, the magnetic field that is frozen into a hot plasma can strongly couple the cosmic ray population to the baryonic gas, such that the two fluids effectively move together. In the following, we picture the cosmic ray population to be confined to its Lagrangian fluid element by a magnetic field, even though the latter is not explicitly included in the simulation formalism. Note that we also neglect the energy density and pressure that is in principle associated with the magnetic field component.

Irregularities in the magnetic field can scatter CR particles such that they escape from their field lines. The magnetic confinement is hence not perfect. To account for this effect, we include a formalism for diffusive transport of cosmic ray particles between adjacent gas mass elements.

4.2.3.3. Fixed spectral shape

In our Galaxy, it is found that cosmic rays follow a power-law spectrum with a spectral index of $\alpha \simeq 2.75$ for particle energies below the "knee" at $\sim 4 \times 10^{15}$ eV. Most of the energy of the cosmic ray spectrum is located below that threshold, and so it is a good approximation to consider the momentum and energy spectrum of cosmic rays under the assumption that it continues further as a power-law to higher energies. For a sufficiently steep spectral index of $\alpha > 2$, the cosmic ray particles in the high-energy range are dynamically unimportant, and the total integrated energy of the population converges without a cutoff for high energies.

At the low end of the momentum spectrum, we need to introduce a cutoff parameter q to keep the cosmic ray energy finite, and to account for the increasingly short dissipation timescale at low energies, which naturally induces such a cut-off. We hence describe the characteristics of the cosmic ray population by a small set of parameters which describe the spectral index and cutoff, and the normalization. The latter directly determines the number density of cosmic ray particles in our simplified picture.

As Enßlin et al. (2006) have shown, it is in principle possible to generalize the formalism to a scheme where the spectral index α is allowed to vary in space and time, albeit at a significant increase in complexity. In this work, we restrict ourselves to the simpler version of the formalism where the slope of the cosmic ray spectrum is kept constant at all times and for all points in the simulation. Note however that we still account for the different spectral indices in various injection processes, so that we expect that this approximation should have no important influence on our results.

4.3. Modelling cosmic ray physics

In the above, we have introduced a theoretical formalism for a simplified treatment of cosmic ray physics during cosmological structure formation. A more detailed discussion of the physical background and the relative importance of various physical source and sink processes, and how they can be incorporated within the simplified framework is given in our paper Enßlin et al. (2006). In this section of the present study, we describe the practical implementation details of the model within the Lagrangian TreeSPH code GADGET-2, including also a concise summary of those parts of the framework of Enßlin et al. (2006) included in the code thus far.

4.3.1. The cosmic ray spectrum and its adiabatic evolution

As discussed above, we assume that the cosmic ray population of each fluid volume element is made up of relativistic protons with an isotropic momentum distribution function of the form

$$f(p) = \frac{\mathrm{d}N}{\mathrm{d}p\,\mathrm{d}V} = C p^{-\alpha}\,\theta(p-q), \tag{4.1}$$

where C is the volume normalization, q is a low momentum cut-off, and α is the power law slope. Momenta are expressed in a dimensionless form in units of $m_\mathrm{p}c$, where m_p is the proton mass. For the purposes of this study, we generally take α to be constant ($\alpha \sim 2.5 - 2.8$), which should be a reasonable first order approximation in most cases relevant to galactic structure formation. While using a variable spectral index α as suggested in Enßlin et al. (2006) could yield more detailed information from the

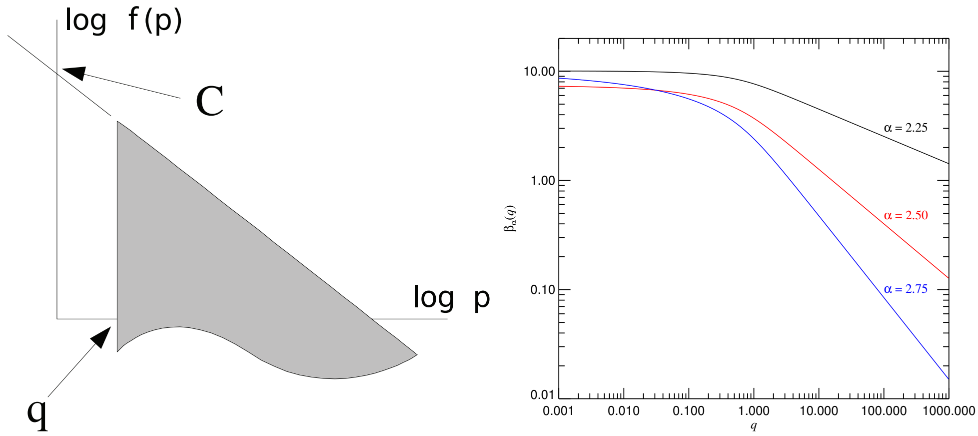

Figure 4.2.: Left panel: Schematic illustration of the cosmic ray momentum spectrum in our two parameter model. We adopt a simple power-law description, where the slope of the cosmic ray spectrum is given by a spectral index α, kept constant throughout our simulation. The normalization of the spectrum is given by the variable C, and the low-momentum cut-off is expressed in terms of a dimensionless variable q, in units of m_pc where m_p is the proton rest mass. **Right Panel:**The function $\beta_\alpha(q)$ introduced in equation (4.5), for several different values of the spectral slope α.

simulations, it would come at a price of substantially increased computational cost and complexity of the implementation, hence we consider the simpler model to be the preferrable approach for this first study.

The pressure of the cosmic ray population in this parameterized model is

$$P_{\rm CR} = \frac{C\, m_{\rm p} c^2}{6}\, \mathcal{B}_{\frac{1}{1+q^2}}\left(\frac{\alpha-2}{2}, \frac{3-\alpha}{2}\right), \tag{4.2}$$

while the number density is $n_{\rm CR} = C\, q^{1-\alpha}/(\alpha-1)$. Here

$$\mathcal{B}_n(a,b) \equiv \int_0^n x^{a-1}(1-x)^{b-1}\,{\rm d}x \tag{4.3}$$

denotes incomplete Beta functions. To describe the kinetic energy per cosmic ray particle for such a power-law population we define the function

$$T_{\rm CR}(\alpha,q) \equiv \left[\frac{1}{2} q^{\alpha-1}\beta_\alpha(q) + \sqrt{1+q^2} - 1\right] m_{\rm p} c^2, \tag{4.4}$$

which will be of later use. The quantity

$$\beta_\alpha(q) \equiv \mathcal{B}_{\frac{1}{1+q^2}}\left(\frac{\alpha-2}{2}, \frac{3-\alpha}{2}\right). \tag{4.5}$$

is here introduced as a convenient abbreviation for the incomplete Beta function. We show $\beta_\alpha(q)$ as a function of q for a few values of α in the right panel of Figure 4.2.

We implement the cosmic ray model in a Lagrangian simulation code, where the advection of the cosmic ray population can be conveniently described simply in terms of the motion of gas particles. In this approach, the normalization of the spectrum should be expressed in terms of a quantity normalized to mass, instead of the volume-normalized quantity C, with the translation between the two being simply given by the local gas density ρ. In our case, it is convenient to absorb the proton mass into a redefinition of the amplitude, so we define

$$\tilde{C} = C\frac{m_\mathrm{p}}{\rho} \tag{4.6}$$

as Lagrangian amplitude of the spectrum. Adiabatic changes of the gas density, affect the normalization of the spectrum according to

$$\tilde{C}(\rho) = \left(\frac{\rho}{\rho_0}\right)^{\frac{\alpha-1}{3}} \tilde{C}_0, \tag{4.7}$$

while the momentum cut-off shifts as

$$q(\rho) = \left(\frac{\rho}{\rho_0}\right)^{\frac{1}{3}} q_0. \tag{4.8}$$

Here, we introduce a reference density ρ_0 (for example set equal to the mean cosmic density, or to unity in code internal, comoving units) and a corresponding normalization $\tilde{C}_0$ and cut-off q_0 at this density. In our numerical implementation, we only have to follow the evolution of the adiabatic invariants $\tilde{C}_0$ and q_0 caused by non-trivial physical source and sink processes, relieving us from the task of computing adiabatic changes of the normalization and cut-off explicitly. Rather, they are accounted for by equations (4.7) and (4.8).

The number density n_CR of relativistic CR protons can also be conveniently expressed in terms of the total baryon density *, yielding

$$\tilde{n} = n_\mathrm{CR}\frac{m_p}{\rho} = \tilde{C}\frac{q^{1-\alpha}}{\alpha-1} = \tilde{C}_0\frac{q_0^{1-\alpha}}{\alpha-1}. \tag{4.9}$$

We can thus interpret $\tilde{n}$ as something like a "cosmic ray to baryon ratio". This quantity is an adiabatic invariant which can be followed accurately in dynamical simulations with our Lagrangian approach.

Note that in our model we do not explicitely remove baryons from the reservoir of ordinary thermal matter when they are accelerated to become relativistic cosmic ray particles. This is a valid approximation, provided we have $\tilde{n} \ll 1$, which is always expected in our applications. In the simulaitons we have performed so far, the fraction of baryons contained in the relativistic phase typically remains far below a maximum value of $\tilde{n} \approx 10^{-4}$. The latter already is an exceptionally large value which we encounter only in our most extreme tests, but it is still small enough to justify our negligence of the reduction of the number density of thermal particles. We note that cosmic ray confinement by magnetic fields only holds in ideal magneto-hydrodynamics (MHD) when the mass fraction in relativistic particles is small.

*We here loosely call ρ/m_p the proton density. In our cosmological applications, we of course use the mean particle mass where appropriate to account for the presence of heavier elements and the ionization state of the gas.

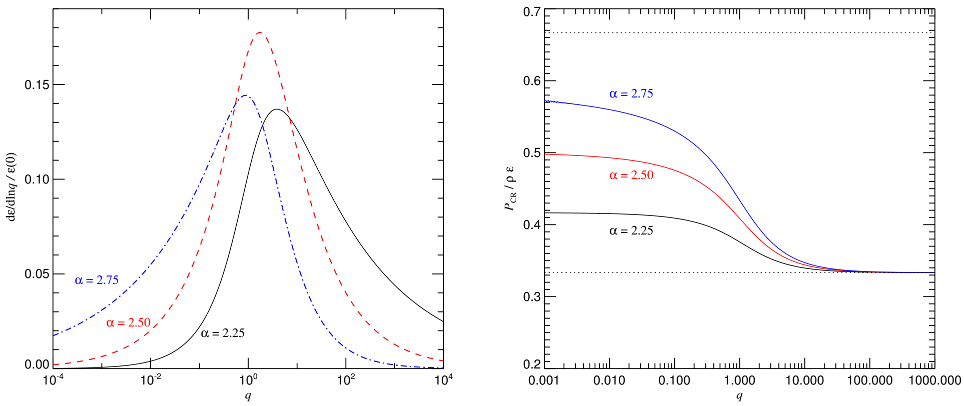

Figure 4.3.: Left panel: The distribution of cosmic ray energy per unit logarithmic interval of proton momentum, for several different values of the spectral slope α. The distributions have been normalized to $\tilde{\varepsilon}(0)$ in each case. **Right panel:** Cosmic ray pressure in units of the cosmic ray energy density, as a function of the spectral cut-off q. Except in the transition region from non-relativistic to relativistic behaviour, the cosmic ray pressure depends only weakly on q. In the ultra-relativistic regime, the ratio approaches $P_{\rm CR}/(\rho\,\tilde{\varepsilon}) \simeq (4/3-1)$, which is shown as the lower dotted line. The upper dotted line gives the expected value of $(5/3-1)$ for an ideal gas. For the same energy content, cosmic rays always contribute less pressure than thermal gas.

In a Lagrangian code, it is natural to express the cosmic ray energy content in terms of energy per unit gas mass, $\tilde{\varepsilon}$, which is given by

$$\tilde{\varepsilon} = c^2 \frac{\tilde{C}}{\alpha - 1}\left[\frac{1}{2}\beta_\alpha(q) + q^{1-\alpha}\left(\sqrt{1+q^2} - 1\right)\right], \tag{4.10}$$

Note that $\tilde{\varepsilon}$ refers to the energy normalized by the total gas mass, not by the mass of the cosmic ray particles alone. The specific energy content can also be expressed as

$$\tilde{\varepsilon} = \frac{T_{\rm CR}\, n_{\rm CR}}{\rho} = \frac{T_{\rm CR}\, \tilde{n}}{m_{\rm p}}. \tag{4.11}$$

In the left panel of figure 4.3, we show the distribution $\mathrm{d}\tilde{\varepsilon}/\mathrm{d}\ln q$ of energy per logarithmic momentum interval, normalized to a spectrum with vanishingly small cut-off. For spectral indices in the range $2 < \alpha < 3$, most of the energy is typically contained around $q \simeq 1$, unless the cut-off of the actual spectrum is larger than that, in which case the particles just above the cut-off will dominate the total energy. The assumption of the momentum distribution extending as a power-law to infinity, restrains the spectral index to $\alpha > 2$, for otherwise the energy would diverge at large momenta. For $\alpha < 3$, the energy remains finite also for an arbitrarily low spectral cut-off.

In the present numerical scheme, every baryonic SPH particle carries the adiabatic invariants q_0 and $\tilde{C}_0$ as internal degrees of freedom for the description of cosmic ray physics. These variables are then used to derive the physical properties of the cosmic ray population, as required for the force evaluations. For the gas dynamics, we are primarily interested in the effective pressure term due to the relativistic particles, which are confined by the ambient magnetic field. In our set of variables, this is compactly given as

$$P_{\rm CR} = \frac{\tilde{C}\rho\, c^2}{6}\beta_\alpha(q). \tag{4.12}$$

In the calculation of the hydrodynamic accelerations with the Euler equation, this partial pressure caused by CRs adds to the ordinary pressure of thermal origin (see Enßlin et al. 2006,for further discussion). This allows for the interface with the ordinary hydrodynamical code to be conveniently small and well localized, requiring only a small number of changes in well defined places.

A quantity of interest when tracing the evolution of gas volume elements is the adiabatic index of the cosmic ray component of a compound gas, which accounts for the non-constant behaviour of the CR population that originates from its semi-relativistic nature. The effective adiabatic index of the cosmic ray pressure component upon local isentropic density changes is

$$\gamma_{\rm CR} \equiv \frac{\partial \log P_{\rm CR}}{\partial \log \rho} = \frac{\alpha+2}{3} - \frac{2}{3}\frac{q^{3-\alpha}}{\beta_\alpha(q)\sqrt{1+q^2}}. \tag{4.13}$$

On the other hand, when the pressure is expressed in terms of the cosmic ray energy density, we obtain

$$\frac{P_{\rm CR}}{\rho\,\tilde{\varepsilon}} = \frac{(\alpha-1)\,\beta_\alpha(q)}{3\beta_\alpha(q) + 6\,q^{1-\alpha}(\sqrt{1+q^2}-1)}. \tag{4.14}$$

The right panel of figure 4.3 visualizes the dependence of the right-hand-side of equation (4.14) on the spectral cut-off q, for different values of the slope α. For large values of q we find $P_{\rm CR}/(\rho\,\tilde{\varepsilon}) \simeq (4/3-1)$, as expected for particles in the ultra-relativistic regime, while for low values of q the ratio is still significantly below the value of $(5/3-1)$ expected for an ideal gas. However, it is clear that for a *given* cosmic ray energy density, the pressure exerted by the CR component depends but weakly on the spectral cut-off; the value of $\tilde{\varepsilon}$ is hence of significantly higher importance to the dynamics than the value of α.

4.3.2. Including non-adiabatic CR processes

The adiabatic behaviour of cosmic rays that are locally locked into the fluid by magnetic fields can be well traced with the above prescriptions. However, there is a multitude of physical processes that affect the CR spectrum of a gas mass element in a non-adiabatic fashion. For instance, particles can be accelerated to relativistic momenta in strong shock waves and thereby become cosmic rays. This process of diffusive shock acceleration should be particularly effective in accretion shocks of high Mach number as found during cosmological structure formation, which can be traced by the hydrodynamical solver of our simulation code. Further, on sub-resolution scales, violent shocks as caused by supernova explosions associated with stellar evolution may inject cosmic rays as well. Other potential astrophysical sources include the ejection of high-energy particles in a jet from an accreting black hole.

In contrast, the cosmic ray population also suffers from a number of loss processes which act to diminish the abundance over time if there is no new supply of freshly injected or accelerated protons. In the present work, we only consider the most prominent loss processes in the form of Coloumb losses that thermalize cosmic ray energy, catastrophic losses that lead to the irradiation of cosmic ray energy as gamma radiation, and diffusion which washes out cosmic ray pressure gradients.

As discussed above and in Enßlin et al. (2006), the present cosmic ray model requires three parameters to describe the state of the relativistic particle component of the gas. One parameter is the spectral index α, which is set to a constant value throughout the simulation volume, specified at the start of the simulation with a value motivated by the typically observed CR spectral index in galactic systems. However, we do not restrict the range of non-adiabatic processes we consider to those with a similar injection index. Rather, we translate the injected cosmic ray properties into changes of amplitude and momentum cut-off within the framework of the simplified, fixed-slope model for the cosmic ray spectrum. This translation is based on basic principles of mass and energy conservation. Despite of this considerable simplification, it is clear that the thermodynamic state of CR gas is considerably more complex than that of an ideal gas, which essentially is determined by the specific entropy alone.

Given some changes of the cosmic ray specific energy ($\mathrm{d}\tilde{\varepsilon}$) and relative CR density ($\mathrm{d}\tilde{n}$) associated with a fluid element within a simulation time step, these changes can be cast into variations of the adiabatic invariants q_0 and $\tilde{C}_0$ of the cosmic ray population using a Jacobian matrix. We find that

$$\mathrm{d}\tilde{C}_0 = \left(\frac{\rho}{\rho_0}\right)^{-\frac{\alpha-1}{3}} \mathrm{d}\tilde{C} = \tilde{C}_0 \frac{m_\mathrm{p}\,\mathrm{d}\tilde{\varepsilon} - T_\mathrm{p}(q)\,\mathrm{d}\tilde{n}}{m_\mathrm{p}\tilde{\varepsilon} - T_\mathrm{p}(q)\,\tilde{n}} \tag{4.15}$$

and

$$\mathrm{d}q_0 = \left(\frac{\rho}{\rho_0}\right)^{-\frac{1}{3}} \mathrm{d}q = \frac{q_0}{\alpha - 1}\,\frac{m_\mathrm{p}\,\mathrm{d}\tilde{\varepsilon} - T_\mathrm{CR}\,\mathrm{d}\tilde{n}}{m_\mathrm{p}\tilde{\varepsilon} - T_\mathrm{p}(q)\,\tilde{n}}, \tag{4.16}$$

where the mean kinetic energy per cosmic ray particle, viz. $T_\mathrm{CR} = \tilde{\varepsilon}\, m_\mathrm{p}/\tilde{n}$, is given by equation (4.4), and

$$T_\mathrm{p}(q) = (\sqrt{1+q^2} - 1) m_\mathrm{p} c^2 \tag{4.17}$$

iss the kinetic energy of a proton with normalized momentum q. Recall that T_CR is a function of q and α only, and does not depend on the normalization of the spectrum.

However, this simple and fast translation scheme will only work for sufficiently small changes to the cosmic ray population. In the present implementation, we therefore apply equations (4.15) and (4.16) only if the relative changes in cosmic ray energy and number density are below a few percent. Otherwise, new cosmic ray spectral parameters in terms of $\tilde{C}_0$ and q_0 are computed by explicitly solving equations (4.9) and (4.10), after applying the principles of energy and particle conservation. While (4.9) can be easily solved for either q_0 or $\tilde{C}_0$, equation (4.10) for the specific energy needs to be inverted (analytically), but this can be done efficiently numerically (see also the discussion in section 4.5.1, and in Enßlin et al. 2006).

It is still important to note, however, that a naive application of energy and particle conservation when adding a newly injected CR component to the current spectrum can cause unphysical results if the spectral cut-offs involved differ substantially. This is due to the strong dependence of the cosmic ray loss processes on particle momentum, in combination with our simplified spectral representation. The lifetime of cosmic ray particles strictly increases with particle momentum. The dependence is particularly steep in the non-relativistic regime ($\tau_{\rm losses}(p) \sim p^3$), but becomes much shallower and eventually nearly flat for particles of the mildly relativistic and strongly relativistic regimes. Simply Adding a CR component with very low cut-off to one with high cut-off while simply enforcing total energy and CR particle number conservation as depicted above results in a new composite spectrum with many of the original CR particles represented as lower momentum particles. Consequently, their cooling times are artificially reduced. Ultimately, this problem arises because the number density of the injected particles is dominated by low momenta, and these have cooling times much shorter than any relevant dynamical timescale. If this is the case, then it would be more reasonable to never inject this population to begin with, and to rather thermalize it instantly, avoiding the unphysical distortion of the composite spectrum.

The two injection processes we consider in this work (shocks and supernova) both supply power-law distributions of cosmic ray particles which start at very low thermal momenta. For those, we define an injection cut-off $q_{\rm inj}$ so only particles and energy above this cut-off are injected, while the rest of the energy is instantly thermalized and added to the thermal reservoir. This cutoff is chosen at a value at which the energy injection rate equals the rate of energy loss for particles in a spectrum with this cutoff, this way ensuring that the population formed could physically exist in the face of the given energy input and cooling rates, i.e.

$$\tau_{\rm losses}(q_{\rm inj}) = \tau_{\rm inj}(\tilde{\varepsilon}, q_{\rm inj}) \tag{4.18}$$

where $\tau_{\rm losses}(q)$ is the cooling timescale

$$\tau_{\rm losses}(q) \equiv \frac{\tilde{\varepsilon}}{|{\rm d}\tilde{\varepsilon}/{\rm d}t|_{\rm losses}} \tag{4.19}$$

due to cosmic ray loss processes for a spectrum with cut-off at q and spectral slope α. This timescale is independent of the normalization of the spectrum, and inversely proportional to the density, provided the weak density-dependence of the Coulomb logarithm in the Coulomb loss-rate is neglected. Given the present cosmic ray energy content $\tilde{\varepsilon}$, the timescale

$$\tau_{\rm inj}(\tilde{\varepsilon}, q_{\rm inj}) \equiv \frac{\tilde{\varepsilon}}{f_{\alpha_{\rm inj}}(q_0, q_{\rm inj})\,({\rm d}\tilde{\varepsilon}/{\rm d}t)_{\rm inj}} \tag{4.20}$$

defines a current heating time corresponding to the injection source, assuming that only the fraction $f(q_0, q_{\rm inj})$ above $q_{\rm inj}$ of the raw energy input rate $({\rm d}\tilde{\varepsilon}/{\rm d}t)_{\rm inj}$ efficiently contributes to the build up of the cosmic ray population. Here q_0 is the intrinsic injection cut-off of the source, which typically lies at very small thermal momenta, and $\alpha_{\rm inj}$ is the slope of the source process. The factor $f_{\alpha_{\rm inj}}(q_0, q_{\rm inj})$ is

$$f_{\alpha_{\rm inj}}(q_0, q_{\rm inj}) = \left(\frac{q_{\rm inj}}{q_0}\right)^{1-\alpha_{\rm inj}} \frac{T_{\rm CR}(\alpha_{\rm inj}, q_{\rm inj})}{T_{\rm CR}(\alpha_{\rm inj}, q_0)} \tag{4.21}$$

for $q_{\rm inj} \geq q_0$, otherwise set to unity.

As mentioned, equation (4.18) states that only cosmic ray particles at momenta where a spectral component *could* grow, are injected given the rate of energy injection. It would be unphysical to assume a spectrum to develop extending as a power-law to momenta lower than $q_{\rm inj}$. The addition of this injection rule is necessary to ensure the present simple model with a fixed spectral shape is physically well-behaved.

Equation (4.18) will typically have two solutions, or may not have any solution at all if the current energy $\tilde{\varepsilon}$ in cosmic rays is high enough. In the former case, the physical solution is the smaller one of the two, at $q_{\rm inj} \le q_{\rm max}$, where $q_{\rm max}$ is the place where the expression $\tau_{\rm losses}(q_{\rm inj}) f(q_0, q_{\rm inj})$ attains its maximum, i.e.

$$\frac{\mathrm{d}}{\mathrm{d}q} \left[\tau_{\rm losses}(q) f(q_0, q)\right]\Big|_{q=q_{\rm max}} = 0\,. \tag{4.22}$$

In the latter case, $q_{\rm inj} = q_{\rm max}$ is chosen, resulting in a solution closest to solving equation (4.18) and naturally corresponding to the point where the largest amount of cosmic ray energy can be contained in a population modeled as a power-law with a balance between loss and source processes.

4.3.3. Shock acceleration

In the present model, we consider two primary sources for cosmic rays, diffusive shock acceleration and supernovae. In the former, a small fraction of the particles streaming through a shock front is assumed to diffuse back and forth through the shock interface, experiencing multiple acceleration cycles. This can only happen to particles in the high-energy tail of the energy distribution, resulting in a power-law momentum distribution function for the accelerated particles.

In the linear regime of CR acceleration, particles above a threshold momentum $q_{\rm inj}$ can be accelerated. They are redistributed into a power-law distribution in momentum that smoothly joins the Maxwell-Boltzmann distribution of the thermal post-shock gas. The slope of the injected CR spectrum is given by

$$\alpha_{\rm inj} = \frac{r+2}{r-1}, \tag{4.23}$$

where $r = \rho_2/\rho_1$ is the density compression ratio at the shock (Bell 1978a,b). If the shock is dominated by thermal pressure, the spectral index can be expressed through the Mach number M as

$$\alpha_{\rm inj} = \frac{4 - M^2 + 3\gamma M^2}{2(M^2 - 1)}. \tag{4.24}$$

The stronger the shock, the flatter the spectrum of the accelerated CR particle population, and the more high-energy particles are produced. Weak shocks on the other hand bring about only rather steep spectra wherein most of the particles are subject to near-instantaneous thermalization.

Due to the continuity between the power law and the thermal spectrum, the injected cosmic ray spectrum is completely specified by the injection threshold q_0, provided the shock strength is known. We assume that q_0 is at a fixed multitude $x_{\rm inj}$ of the average thermal post-shock momentum, $p_{\rm th}$ =

$\sqrt{2kT_2/(m_p c^2)}$, i.e. $q_0 = x_{\rm inj} p_{\rm th}$. In this case, the fraction of particles that experience shock acceleration does not depend on the post-shock temperature T_2, and is

$$\Delta\tilde{n}_{\rm lin} = \frac{4}{\sqrt{\pi}} \frac{x_{\rm inj}^3}{\alpha_{\rm inj} - 1} {\rm e}^{-x_{\rm inj}^2}. \tag{4.25}$$

We typically adopt a fixed value of $x_{\rm inj} \simeq 3.5$, motivated by theoretical studies of shocks in galactic supernova remnants (e.g. Drury et al. 1989). Here, the fraction of injected supernovae particles in strong shocks is then a few times 10^{-4} (Drury et al. 1989, Jones & Kang 1993, Kang & Jones 1995).

In the linear regime of CR acceleration, the specific energy per unit gas mass in the injected cosmic ray population is

$$\Delta\tilde{\varepsilon}_{\rm lin} = \frac{T_{\rm CR}(\alpha_{\rm inj}, q_{\rm inj})\, \Delta\tilde{n}_{\rm lin}}{m_p}\,. \tag{4.26}$$

We use this value to define a shock injection efficiency for CRs by relating the injected energy to the dissipated energy per unit mass at the shock front. The latter appears as extra thermal energy above the adiabatic compression at the shock and is given by $\Delta u_{\rm diss} = u_2 - u_1 r^{\gamma-1}$, where u_1 and u_2 are the thermal energies per unit mass before and after the shock, respectively. The injection efficiency of linear theory is

$$\zeta_{\rm lin} \equiv \frac{\Delta\tilde{\varepsilon}_{\rm lin}}{\Delta u_{\rm diss}}. \tag{4.27}$$

It should be noted that, however, the shock acceleration effect experiences saturation when the dynamical CR pressure grows to be comparable to the upstream ram pressure $\rho_1 v_1^2$ of the flow. We account for this by adopting the limiter suggested by Enßlin et al. (2006), and define a final acceleration efficiency of

$$\zeta_{\rm inj} = \left[1 - \exp\left(-\frac{\zeta_{\rm lin}}{\zeta_{\rm max}}\right)\right] \zeta_{\rm max}. \tag{4.28}$$

We adopt $\zeta_{\rm max} = 0.5$ for the results of this study. Thus, we take the injected energy to be

$$\Delta\tilde{\varepsilon}_{\rm inj} = \zeta_{\rm inj} \Delta u_{\rm diss}, \tag{4.29}$$

and correspondingly, the injected particle number is set to be

$$\Delta\tilde{n}_{\rm inj} = \frac{m_p\, \Delta\tilde{\varepsilon}_{\rm inj}}{T_{\rm CR}(\alpha_{\rm inj}, q_0)}, \tag{4.30}$$

where $T_{\rm CR}(\alpha_{\rm inj}, q_0)$ is the mean kinetic energy of the accelerated cosmic ray particles. In practice, both $\Delta\tilde{\varepsilon}_{\rm inj}$ and $\Delta\tilde{n}_{\rm inj}$ is lowered when we shift the actual injection point from q_0 to $q_{\rm inj}$, as determined by equation (4.18), with the difference of the energies fed to the thermal reservoir directly.

It is clear that the efficiency of CR particle acceleration strongly depends on the compression ratio, or equivalently on the Mach number of shocks. Interestingly, accretion shocks during cosmological structure formation can be particularly strong. Hence, we expect potentially interesting effects both for the forming intragroup and intracluster media, as well as for the intergalactic medium. However, in order to accurately account for the cosmic ray injection generated in structure formation shocks, we need to be able to estimate shock strengths in SPH simulations. SPH captures shocks using an artificial viscosity instead of an explicit shock detection scheme however, making this a non-trivial problem.

In Pfrommer et al. (2006), we propose a practical solution to this problem and have developed a novel method for measuring the Mach number of shocks on the fly during cosmological SPH calculation. The method is based on the entropy formulation for SPH by Springel & Hernquist (2002), as briefly introduced in section 2.2.2 of this work, and uses the current rate of entropy injection caused by the viscosity, combined with an approximation for the numerical shock transit time, to estimate the shock Mach number. This scheme works better than may have been expected, and it is in fact capable of producing quite accurate Mach number estimates, even for the case of composite gas with thermal and cosmic ray pressure components. In cosmological simulations, the method gathers Mach number statistics which are in good agreement results obtained from hydrodynamical mesh codes using explicit Riemann solvers (Ryu et al. 2003, Pfrommer et al. 2006).

Having a reliable Mach number estimator solves an important problem when trying to account for cosmic ray injection by shocks in SPH. Yet another complication is posed by the shock broadening inherent in SPH, however, which implies a finite shock transit time for particles, i.e. an SPH particle may require several timesteps before it has passed through a shock and received the full dissipative heating. The number of these steps depends on the timestep criterion employed, and can in principle be very large for a sufficiently conservative choice of the Courant coefficient. Unlike assumed in the above treatment of diffusive shock acceleration, we hence are not dealing with a discrete injection event, but rather need to formulate the cosmic ray acceleration in a 'continuous fashion', in parallel to the thermal dissipation, such that the final result does not depend on how many timesteps are taken to resolve the transit through a broadened shock front.

Fortunately, the above treatment can be easily adjusted to these conditions. We insert the dissipated energy in the *current timestep* for $\Delta u_{\rm diss}$ in equation (4.29). This quantity is computed in the existing SPH formalism already, and in fact, we know that SPH will integrate $\Delta u_{\rm diss}$ correctly through the shock profile, independent of the number of steps taken. This is because the correct pre- and post-shock state of the gas are ensured by the conservation laws, which are fulfilled by the conservative SPH code. For this, the Rankine-Hugoniot jump conditions are reproduced across the broadened shock. Note however that for computing the linear shock injection efficiency according to equation (4.27), we need to continue using an estimate for the total energy dissipated across the entire shock transit, based on the Mach number finder.

For simplified test calculation with the code, we have also implemented an option to assume a constant injection efficiency of the shock acceleration process, along with a constant spectral index and momentum cut-off parameter. Values for these parameters can then be chosen to represent the energetically most important types of shocks in the environment to be simulated. Such a simplified injection mechanism can be used get an idea about the importance of the Mach-number dependence of the shock acceleration for different environments.

4.3.4. Injection of cosmic rays by supernovae

Strong shock waves associated with supernovae explosions are believed to be one of the most important cosmic ray injection mechanisms in the interstellar medium. Similar to star formation itself, individual supernovae are far below our resolution limit in cosmological simulations where that are required to model whole galaxies, or more challenging still, sizable parts of the observable universe. We therefore resort to a subresolution treatment for star formation and its regulation by supernovae, as proposed by Springel & Hernquist (2003a). In this model, the interstellar medium is pictured as a multiphase medium composed of dense, cold clouds, embedded in a tenuous hot phase. The clouds form out of the diffuse medium by thermal instability, and are the sites of star formation. The fraction of massive stars of each formed stellar population is assumed to explode instantly, heating the hot phase, and evaporating some of the cold clouds. This way, a tight self-regulation cycle for star formation in the ISM is established.

To model the generation of cosmic rays, we assume that a certain fraction $\zeta_{\rm SN} \simeq 0.1 - 0.3$ of the supernova energy appears as a cosmic ray population (Aharonian et al. 2006, Kang & Jones 2006). The total rate of energy injection by supernovae for a given star formation rate $\dot{\rho}_\star$ depends on the IMF. Assuming a Salpeter IMF and a treshold stellar mass of $8\,{\rm M}_\odot$ above which starts near-instantaneously explode as supernova with a canonical energy release of 10^{51} ergs, we find roughly one supernova per $250\,{\rm M}_\odot$ of stellar mass formed, translating to an energy injection rate per unit volume of $\epsilon_{\rm SN}\dot{\rho}_\star$, with $\epsilon_{\rm SN} = 4\times10^{48}\,{\rm ergs\,M}_\odot^{-1}$. So, we model the CR energy injection per timestep of a gas particle as

$$\Delta\tilde{\varepsilon}_{\rm SN} = \zeta_{\rm SN}\epsilon_{\rm SN}\,\dot{m}_\star\,\Delta t, \tag{4.31}$$

where $\dot{m}_\star = \dot{\rho}_\star/\rho$ is the particle's star formation rate per unit mass. Uncertainties in the IMF are of minor importance here as we have introduced a free parameter, $\zeta_{\rm SN}$, to control the amount of energy that is fed into cosmic rays.

For the power-law of the injected cosmic ray population, we assume a plausible slope value of $\alpha_{\rm SN} = 2.4$ (Aharonian et al. 2004, 2006), and for the cut-off $q_{\rm SN}$, we adopt a thermal momentum of $q_{\rm SN} = \sqrt{kT_{\rm SN}/(m_{\rm p}c^2)}$ for a fiducial supernova temperature characteristic for the involved shock acceleration. The choice of $\alpha_{\rm SN} = 2.4$ for the injection slope is motivated by the observed slope of ~ 2.75 in the ISM, and the realization that momentum dependent diffusion in a turbulent magnetic field with a Kolmogorov-type spectrum on small scales should steepen the injected spectrum by $p^{-1/3}$ in equilibrium. The results do not depend on the particular choice for $T_{\rm SN}$, provided $q_{\rm SN} \ll 1$. The change of the particle number density can be computed with the mean kinetic energy $T_{\rm CR}(\alpha_{\rm SN}, q_{\rm SN})$ of the injected power law. Using equations (4.4) and (4.11), one finds

$$\Delta\tilde{n} = m_{\rm p}\frac{\zeta_{\rm SN}\epsilon_{\rm SN}\dot{m}_\star}{T_{\rm CR}(\alpha_{\rm SN}, q_{\rm SN})}\,\Delta t. \tag{4.32}$$

In the formalism of Springel & Hernquist (2003a), we need to reduce the supernovae energy injected into thermal feedback (and to an optional wind model if used) by the fraction $\zeta_{\rm SN}$ that we assume powers cosmic ray acceleration in order to get directly comparable results.

4.3.5. Coulomb cooling and catastrophic losses

Charged particles moving through a plasma gradually dissipate their kinetic energy and transfer it to the surrounding ions and electrons by means of Coulomb interactions. The rate of this energy loss depends both on the physical properties of the surrounding medium and on the detailed momentum spectrum of the cosmic ray population. The latter in particular complicates an accurate determination of the Coulomb loss rate.

Since particles with low momenta are affected by the Coulomb interactions most prominently, a qualitative consequence of this effect is a flattening of the spectrum; the high-momentum tail remains unchanged while the low-momentum cosmic ray particles dissipate their energy effectively to the thermal gas, and eventually drop out of the cosmic ray population altogether.

In the present model, we deliberately abandon a detailed representation of the cosmic ray spectrum of each fluid element, in favour of the high computational speed and low memory consumption that the simplified spectral model allows for. We even further opt to use a globally fixed spectral index, which means that we cannot represent a spectral flattening in detail. However, we still can account for the effect of thermalization of the low-momentum particles in a simple and efficient way. To this end, we compute the energy loss by Coulomb-cooling over the entire spectrum, and then shift the low-momentum cutoff of our spectral model such that just the right amount of energy is removed in low-momentum particles, keeping the high-momentum part unaffected.

More specifically, we follow Enßlin et al. (2006) and estimate the Coulomb loss rate of the CR population as

$$\left(\frac{\mathrm{d}\tilde{\varepsilon}}{\mathrm{d}t}\right)_{\mathrm{C}} = -\frac{2\pi\tilde{C}e^4\,n_{\mathrm{e}}}{m_{\mathrm{e}}m_{\mathrm{p}}c}\left[\ln\left(\frac{2m_{\mathrm{e}}c^2\,\langle\beta p\rangle}{\hbar\omega}\right)\times \mathcal{B}_{\frac{1}{1+q^2}}\left(\frac{\alpha-1}{2},-\frac{\alpha}{2}\right)-\frac{1}{2}\mathcal{B}_{\frac{1}{1+q^2}}\left(\frac{\alpha-1}{2},-\frac{\alpha-2}{2}\right)\right]. \tag{4.33}$$

Here, n_{e} is the electron abundance, $\omega = \sqrt{4\pi e^2 n_{\mathrm{e}}/m_{\mathrm{e}}}$ the plasma frequency, and $\langle\beta p\rangle = 3P_{\mathrm{CR}}/(\rho\tilde{n}c^2)$ is a mean value for our assumed spectrum. We also define a cooling timescale for Coulomb cooling as

$$\tau_{\mathrm{C}}(q) = \frac{\tilde{\varepsilon}}{|\mathrm{d}\tilde{\varepsilon}/\mathrm{d}t|_{\mathrm{C}}}, \tag{4.34}$$

which only depends on the spectral cut-off q, and is inversely proportional to density, modulo a very weak additional logarithmic density-dependence originating from the plasma frequency. For a given energy loss $\Delta\tilde{\varepsilon}_{\mathrm{C}}$ in a timestep based on this rate, we estimate the corresponding change in cosmic ray number density as

$$\Delta\tilde{n}_{\mathrm{C}} = \Delta\tilde{\varepsilon}_{\mathrm{C}}\,\frac{m_{\mathrm{p}}}{T_{\mathrm{p}}(q)}, \tag{4.35}$$

i.e. we assume that particles are removed at the low momentum cut-off q. From equations (4.15) and (4.16), it is obvious that this will result in a gradual rise of the spectral cutoff q leaving the normalization unchanged. The corresponding energy loss $\Delta\tilde{\varepsilon}_{\mathrm{C}}$ is added to the thermal energy in the ordinary gas

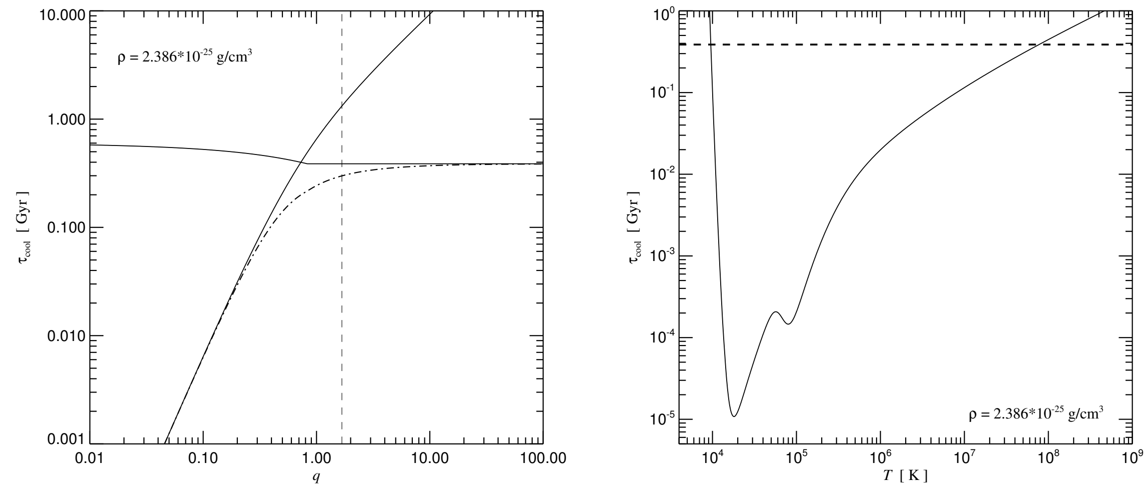

Figure 4.4.: The left panel shows the cooling times due to Coulomb losses (rising solid line) and hadronic dissipation (nearly horizontal line) as a function of the spectral cut-off. The dot-dashed line gives the total cooling time, while the vertical dashed lines marks the asymptotic equilibrium cut-off reached by the CR spectrum when no sources are present. **The right panel** shows the cooling time of ordinary thermal gas due to radiative cooling (for primordial metallicity), as a function of temperature. The horizontal dashed line marks the cooling time of CRs with a high momentum cut-off ($q \gg 1$), for comparison. In both panels, the times have been computed for a gas density of $\rho = 2.386 \times 10^{-25}\,\mathrm{g\,cm^{-3}}$, which corresponds to the density threshold for star formation that we usually adopt. Note however that the cooling times all scale as $\tau \propto 1/\rho$, i.e. for different densities, only the vertical scale would change but the relative position of the lines would remain unaltered.

component, i.e. the Coulomb cooling process leaves the total energy content of the gas unaffected. For large Coulomb cooling rates, we use an implicit solver to compute the new position of the spectral cut-off, again leaving the amplitude parameter exactly invariant. This ensures numerical stability even if the cut-off parameter is increased substantially during a single timestep.

Another class of loss processes for cosmic rays results are the losses occurring in inelastic collisions with atom nuclei in the ambient gas, resulting in hadronic production of pions, which subsequently decay into γ-rays, secondary electrons, and neutrinos. In this case, the energy is ultimately dissipated into photons which tend to escape. The net effect is a total loss of energy from the system (unless radiative energy is accounted for in some way).

These 'catastrophic losses' can only proceed for cosmic ray particles exceeding the energy threshold of $q_{\mathrm{thr}} m_{\mathrm{p}} c^2 = 0.78\,\mathrm{GeV}$ for pion production ($q_{\mathrm{thr}} = 0.83$). The total loss rate is described by (Enßlin et al. 2006) as

$$\left(\frac{\mathrm{d}\tilde{\varepsilon}}{\mathrm{d}t}\right)_{\mathrm{had}} = -\frac{c\,\rho\overline{\sigma}_{\mathrm{pp}}\,\tilde{C}\,q_\star^{1-\alpha}\,T_{\mathrm{CR}}(\alpha, q_\star)}{2(\alpha-1)\,m_{\mathrm{p}}^2}, \tag{4.36}$$

where $\overline{\sigma}_{\mathrm{pp}} \simeq 32\,\mathrm{mbarn}$ is the averaged pion production cross section, and $q_\star$ denotes $q_\star = \max\{q, q_{\mathrm{thr}}\}$. The number density of cosmic ray particles remains unchanged, however, due to conservation of baryon number in strong and electroweak interactions, i.e. $\Delta\tilde{n}_{\rm had} = 0$. This condition in turn implies that the changes of amplitude and cut-off of our spectral model due to this cooling process are related by

$$\frac{\Delta\tilde{C}}{\tilde{C}} = (\alpha - 1)\,\frac{\Delta q}{q}. \tag{4.37}$$

As before, we define a cooling timescale for catastrophic losses, as

$$\tau_{\rm had}(q) \equiv \frac{\tilde{\varepsilon}}{|{\rm d}\tilde{\varepsilon}/{\rm d}t|_{\rm had}} = \frac{2\,m_{\rm p}}{c\rho\,\overline{\sigma}_{\rm pp}}\,\frac{T_{\rm CR}(\alpha,q)}{T_{\rm CR}(\alpha,q_\star)}\left(\frac{q}{q_\star}\right)^{1-\alpha}. \tag{4.38}$$

Note that $\tau_{\rm had}$ is constant for $q \geq q_{\rm thr}$ (in this case, $q_\star = q$).

In the left panel of Figure 4.4, we show the cooling timescales for Coulomb and catastrophic losses as a function of the cut-off parameter q, at a fiducial density corresponding to the star formation threshold value, assuming a spectral index $\alpha = 2.5$. As expected, catastrophic losses dominate for high momentum cut-offs, and therefore limit the lifetime of any cosmic ray population to $\tau \sim 2\,m_{\rm p}/(c\rho\,\overline{\sigma}_{\rm pp})$, unless an injection process provides a resupply. For small cut-off values, Coulomb losses are dominant and will act to rapidly thermalize the low momentum cosmic rays. The dot-dashed line shows the total loss timescale,

$$\frac{1}{\tau_{\rm losses}(q)} = \frac{1}{\tau_{\rm C}(q)} + \frac{1}{\tau_{\rm had}(q)}\,. \tag{4.39}$$

This timescale is strictly increasing with q.

In the absence of any injection, the cosmic ray population evolves towards a distinct cut-off $q_{\rm fix}$, driven by the tendency of Coulomb cooling to increase the cut-off, while catastrophic losses tend to lower it. A balance is reached at the solution of the equation

$$1 + \frac{\tau_{\rm C}(q_{\rm fix})}{\tau_{\rm had}(q_{\rm fix})} = \frac{T_{\rm CR}(\alpha,q_{\rm fix})}{T_{\rm p}(q_{\rm fix})}, \tag{4.40}$$

which is a direct consequence of equations (4.15) and (4.16). The vertical dotted line in Figure 4.4 marks this equilibrium point at $q_{\rm fix} = 1.685$ for $\alpha = 2.5$. Once this fix-point is reached, only the spectral amplitude is affected and decreases due to the cosmic ray cooling and dissipation processes. Finally, both the Coulomb cooling and the hadronic cooling time are inversely proportional to density. Therefore, the fix-point $q_{\rm fix}$ is density independent, but whether it can be reached in the available time at low density is a another question.

It is also interesting to compare the cosmic ray loss timescale to the thermal cooling timescale of primordial gas. The latter is inversely proportional to density, as well, but in addition features a strong temperature dependence. In the right panel of Figure 4.4, we show the thermal cooling timescale as a function of temperature, at the same fiducial density used in the top panel. For comparison, we show the asymptotic cosmic ray dissipation time scale (dashed line), which is reached if the cosmic ray population is dominated by the relativistic regime. In this case, cosmic rays decay much slower than the thermal gas pressure in the intermediate temperature regime. This could be interesting for cooling flows in halos

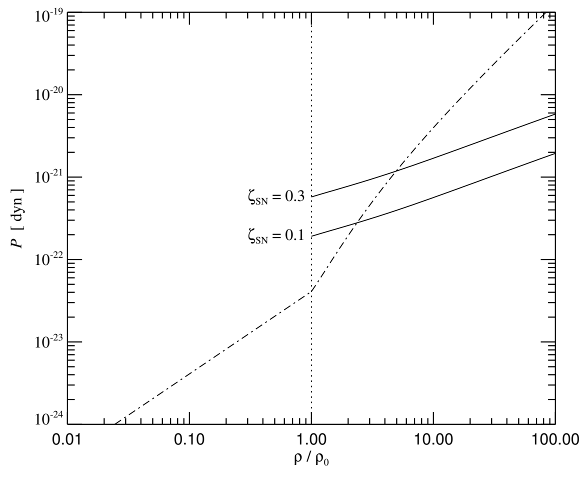

Figure 4.5.: Pressure of the cosmic ray population predicted for equilibrium between supernova injection on one hand, and Coulomb cooling and catastrophic losses on the other hand. The sold lines mark the pressure as a function of overdensity for two values of the injection efficiency $\zeta_{\rm SN}$. The assumed threshold density for star formation, $\rho_0 = 2.4 \times 10^{-25}\,{\rm g\,cm^{-3}}$, is derived from the multiphase model of Springel & Hernquist (2003a). The latter also predicts an effective equation of state for the star forming phase, shown as a dot-dashed line. The part below the threshold is an isothermal equation of state with temperature 10^4 K.

or clusters. Even a moderate cosmic ray pressure contribution in the diffuse gas in a halo of temperature $T_{\rm vir} \sim 10^5 - 10^7$ K should tend to survive longer than the thermal gas pressure, which could influence the cooling rate. We examine this question explicitly in our numerical simulations of isolated halos in a later section of this work.

4.3.6. Equilibrium between source and sink terms

The above considerations lead to an interesting question: What does the cosmic ray spectrum look like for a fluid element at a density ρ high enough to allow star formation, such that is fed at a constant rate by supernova injection? We expect that after some time, a balance is established between the supernova input on one hand and the cosmic ray losses due to Coulomb cooling and hadronic processes on the other hand. The energy content in the cosmic rays at this equilibrium point determines the CR pressure, and comparison of this pressure with the thermal pressure of the ISM reveals whether 'cosmic ray feedback' could be important in regulating star formation in galaxies.

To derive this equilibrium point, starting from the conditions $\Delta\tilde{\varepsilon}_{\rm SN} + \Delta\tilde{\varepsilon}_{\rm C} + \Delta\tilde{\varepsilon}_{\rm had} = 0$ combined with $\Delta\tilde{n}_{\rm SN} + \Delta\tilde{n}_{\rm C} = 0^{\dagger}$, it directly follows that the mean energy per injected particle due to supernovae in equilibrium must be

$$T_{\rm CR}(\alpha_{\rm SN}, q_{\rm inj}) = T_{\rm p}(q_{\rm eq})\left[1 + \frac{\tau_{\rm C}(q_{\rm eq})}{\tau_{\rm had}(q_{\rm eq})}\right]. \tag{4.41}$$

This equation relates the effective injection cut-off of the supernova feeding, and the equilibrium cut-off $q_{\rm eq}$ of the CR spectrum. In equilibrium, we know that the supernova input just balances the cooling losses for the spectrum with equilibrium cut-off $q_{\rm eq}$, yielding

$$\tilde{\varepsilon} = \tau_{\rm losses}(q_{\rm eq})\, f(q_{\rm SN}, q_{\rm inj}) \left(\frac{{\rm d}\tilde{\varepsilon}}{{\rm d}t}\right)_{\rm SN}. \tag{4.42}$$

On the other hand, the injection criterion of equation (4.18) provides $\tilde{\varepsilon} = \tau_{\rm losses}(q_{\rm inj})\, f(q_{\rm SN}, q_{\rm inj}) \left(\frac{{\rm d}\tilde{\varepsilon}}{{\rm d}t}\right)_{\rm SN}$, given a solution for equation (4.18) actually exists when the system is in the dynamic equilibrium. Assuming this for the moment, the CR loss timescales at $q_{\rm inj}$ and $q_{\rm eq}$ are equal, which in turn implies $q_{\rm inj} = q_{\rm eq}$. That is, the injection cut-off coincides with the cut-off of the equilibrium spectrum. The location of the equilibrium cut-off itself is a solution of

$$1 + \frac{\tau_{\rm C}(q_{\rm eq})}{\tau_{\rm had}(q_{\rm eq})} = \frac{T_{\rm CR}(\alpha_{\rm SN}, q_{\rm eq})}{T_{\rm p}(q_{\rm eq})}. \tag{4.43}$$

This is almost identical to equation (4.40) which describes the fix-point of the cut-off if there is no injection. What sets both equations apartis the occurrence of $\alpha_{\rm SN}$ instead of just α in the argument of the $T_{\rm CR}$ function. This results in a slight shift of the equilibrium position once the assumed spectral indices for supernova injection and the general cosmic ray population differ. For $\alpha_{\rm SN} = \alpha$, there will be no difference. It may seem surprising that the equilibrium position can be shifted from the fix-point by an *arbitrarily small* supernova injection rate. However, recall that in the injection case we have described a truly invariant spectrum with a fixed amplitude (which may take very long time to be established), while in the case without injection, the amplitude keeps decreasing on the cooling timescale.

The above assumes that the injection condition (4.18) has a solution in equilibrium. This is the case if $q_{\rm eq}$ of equation (4.43) is smaller or equal than $q_{\rm max}$ of equation (4.22). Otherwise the injection cut-off is given by $q_{\rm inj} = q_{\rm max}$, and the position of the equilibrium cut off is determined by equation (4.42). A detailed comparison of the steady-state CR spectrum with and without our approximate description is provided by Enßlin et al. (2006). It shows that dynamically important quantities like cosmic ray pressure and energy are calculated with $\sim 10\%$ accuracy by the presented formalism.

The equilibrium value of the cosmic ray energy content is of primary importance, because it directly determines the CR pressure and hence the strength of potential feedback effects on star formation. The total cosmic ray energy injection rate by supernovae is related to the star formation rate by equation (4.31).

[†]Note that we always have $\Delta\tilde{n}_{\rm had} = 0$.

Once the equilibrium cut-off is $q_{\rm eq}$ is known, the energy content in equilibrium is that of equation (4.42), so the pressure is fully specified. For example, in the case of $q_{\rm eq} \leq q_{\rm max}$, the final pressure is

$$P_{\rm CR} = \frac{(\alpha - 1)\beta_\alpha(q_{\rm eq})\,\tau_{\rm loss}(q_{\rm eq})\,f_{\alpha_{\rm SN}}(q_{\rm SN}, q_{\rm eq})}{3\beta_\alpha(q_{\rm eq}) + 6\,q_{\rm eq}^{1-\alpha}(\sqrt{1+q_{\rm eq}^2} - 1)}\,\zeta_{\rm SN}\epsilon_{\rm SN}\dot{\rho}_\star. \tag{4.44}$$

In the simulations as described in more detail further below, we combine the cosmic ray formalism with the subresolution multiphase model for the regulation of star formation by Springel & Hernquist (2003a). In the latter, the mean star formation rate is determined by the local density, and scales approximately as $\dot{\rho}_\star \propto \rho^{1.5}$ above a density threshold for the onset of star formation. A detailed discussion of the multiphase model together with the precise density dependence of the star formation rate is found in chapter 2 and in Springel & Hernquist (2003a). There, an effective equation of state for the ISM, which governs the assumed two-phase structure of the ISM, is derived.

In Figure 4.5, we show this effective pressure as a function of density, using the parameters for gas consumption timescale, initial mass function, and cloud evaporation efficiency discussed in the above-noted locations, which result in a star formation threshold of $\rho_{\rm th} = 2.4 \times 10^{-25}\,{\rm g\,cm^{-3}}$. We plot the expected cosmic ray pressure in the same diagram, for two different injection efficiencies of $\zeta_{\rm SN} = 0.1$ and $\zeta_{\rm SN} = 0.3$. Interestingly, the cosmic ray pressure exceeds the thermal pressure at the threshold density for star formation, but with the shallow density dependence of the equilibrium pressure, approximately $P_{\rm CR} \sim \rho^{0.5}$ (note that $\tau_{\rm losses} \propto \rho^{-1}$), we find that the pressure of cosmic rays only plays a sizeable role for the low density part of the ISM model. Regions with high specific star formation rates should be weakly affected at most.

For small efficiencies $\zeta_{\rm SN} \leq 0.01$, we substantially expect no significant influence on the regulation of star formation by cosmic rays from supernova whatsoever. Even for the fiducial choice of $\zeta_{\rm SN} = 1$, the influence would vanish for densities $\rho > 100\rho_{\rm th}$. Based on these findings, we expect that galaxies which form most of their stars at comparatively low densities should be potentially strongly affected by the cosmic ray feedback, while this influence should be weak or absent for vigorously star-forming galaxies with higher typical ISM densities. Our numerical results presented further below confirm this picture. The fact that CR-pressure seems to become dominating around the star formation threshold might even suggest that cosmic rays could have an active part in defining this threshold.

4.4. Cosmic ray diffusion

The presented treatment is based on the notion that the cosmic ray particles are to a large degree locked into gas fluid elemenst by locally present magnetic fields. Even weak ambient fields are able to cause the charged particle to gyrate around the field lines, thus preventing free travelling over macroscopic distances with their intrinsic velocities (close to to the speed of light). The cosmic ray particles' average positions (the centers of their gyrations) slowly move along the field lines, but their perpendicular transport is strongly suppressed.

However, occasional scattering of particles on magnetic irregularities of MHD waves can displace the gyrocentres of particles, such that a particle effectively "changes its field line", enabling it to move perpendicular to the field. Realistic magnetic field configurations are often highly tangled, or even chaotic. Therefore, transitions from one state to the next (from one magnetic field like to the next) can lead to sizable cross-field speeds of the particles. From a macroscopic point of view, the motion of the cosmic ray population can be described as a diffusion process, which is anisotropic, depending on the local magnetic field configuration. The theory of the respective diffusion coefficients is complicated, and uncertain for the case of turbulent magnetic field configurations (e.g. Rechester & Rosenbluth 1978, Duffy et al. 1995, Bieber & Matthaeus 1997, Giacalone & Jokipii 1999, Narayan & Medvedev 2001, Enßlin 2003).

In principle, one could try to simulate the magnetic field in SPH and then treat the diffusion in an anisotropic fashion. While recent advances in modelling MHD with SPH are promising (Dolag et al. 1999, Price & Monaghan 2004), these techniques still face severe numerical challenges when applied to simulations that include radiative cooling processes. Therefore, we defer such an approach to future work and model the diffusion as being isotropic in the present work. Also, since we have no direct information on the local magnetic field strength and configuration, we invoke a phenomenological approach to estimate the effective diffusion coefficient as a function of the local conditions of the gas. It will be easy to refine the spatial dependence of the diffusion coefficient once a more detailed physical scenario becomes available.

Assuming isotropicy, the diffusion in the CR distribution function $f(p, \boldsymbol{x}, t)$ can be written as

$$\frac{\partial f}{\partial t} = \boldsymbol{\nabla}(\kappa \boldsymbol{\nabla} f). \tag{4.45}$$

The diffusion coefficient κ itself depends on the particle momentum (more energetic particles diffuse faster), and on the local magnetic field configuration. For definiteness we assume that the underlying MHD is turbulent with a Kolmogorov power spectrum, in which case the momentum dependence of κ is

$$\kappa(p) = \tilde{\kappa}\, p^{\frac{1}{3}}. \tag{4.46}$$

Here, we assumed relativistic particle velocities with $v \simeq c$. Integrating the diffusion equation over particle momenta then yields

$$\left.\frac{\partial n_{\rm CR}}{\partial t}\right|_{\rm diff} = \frac{\alpha - 1}{\alpha - \frac{4}{3}}\ \boldsymbol{\nabla}\tilde{\kappa}\boldsymbol{\nabla}(q^{\frac{1}{3}} n_{\rm CR}), \tag{4.47}$$

where q is the spectral cut-off. Because more energetic particles diffuse faster, we expect the diffusion speed for the cosmic ray energy density to be a bit larger than for the number density itself. To account for this effect, we multiply the diffusion equation (4.45) with $T_{\rm p}(p)$, and integrate over the particle momenta. This results in

$$\left.\frac{\partial \varepsilon_{\rm CR}}{\partial t}\right|_{\rm diff} = \frac{\alpha - 1}{\alpha - \frac{4}{3}}\ \boldsymbol{\nabla}\tilde{\kappa}\boldsymbol{\nabla}\left(q^{\frac{1}{3}}\frac{T_{\rm CR}(\alpha - \frac{1}{3}, q)}{T_{\rm CR}(\alpha, q)}\,\varepsilon_{\rm CR}\right), \tag{4.48}$$

where $\varepsilon_{\rm CR} = \rho\tilde{\varepsilon}$ is the cosmic ray energy density per unit volume. It is obvious that the diffusion formalism of the presented model can only be applied to cosmic ray populations with a spectral index of $\alpha > 7/3$. The factor $T_{\rm CR}(\alpha - \frac{1}{3}, q)/T_{\rm CR}(\alpha, q)$ is larger than unity and encodes the fact that the diffusion in energy density proceeds faster than in particle number density. In Enßlin et al. (2006), we also give more general formulae for different power-law dependences of the diffusivity, and provide a more accurate treatment where the reduction of the diffusion rate at sub-relativistic energies is accounted for.

4.4.1. Modelling the diffusivity

Due to the lack of direct local information on the magnetic field strength in the present numerical models, we parameterize the dependence of the diffusion coefficient on local gas properties in terms of a fiducial power-law dependence on the local gas density and gas temperature. In particular, we use a parameterized form,

$$\tilde{\kappa} = \kappa_0 \left(\frac{\rho}{\rho_0}\right)^{n_\rho} \left(\frac{T}{T_0}\right)^{n_T}, \tag{4.49}$$

for the diffusion constant, specified by the overall strength κ_0 of the diffusion at a reference density and temperature, and by the power-law slopes n_ρ and n_T for the density and temperature dependence, respectively.

Clearly a schematic simplification, this parameterization is yet general enough to allow an analysis of a number of interesting cases, including models where the typical magnetic field strength has a simple density dependence, which can be a reasonable first order approximation for some systems, for example for the diffuse gas in cluster atmospheres (Dolag et al. 2004b).

For definiteness, we construct such a very simple model, which is the fiducial choice yielding the results on diffusion presented in this study. In Kolmogorov-like MHD turbulence, the dominant parallel diffusivity is expected to scale as (Enßlin 2003)

$$\tilde{\kappa} \propto {l_B}^{2/3}\, B^{-1/3}, \tag{4.50}$$

where l_B is a characteristic length scale for the magnetic field of strength B. We start out by assuming that the magnetic energy density is a fixed fraction of the thermal energy content, i.e.

$$B \propto \rho^{1/2} T^{1/2}. \tag{4.51}$$

An appropriate length scale for l_B is more difficult to estimate, as it sensitively depends on the level of local MHD turbulence, and on the build-up of the magnetic field due to structure formation processes. For simplicity, we assume that the length scale is related to the local Jeans scale. This seems to be appropriate for the conditions of a multiphase interstellar medium where local density fluctuations constantly form clouds of order a Jeans mass, which are then in part dispersed by supernova-driven turbulence, and results in a scaling like

$$l_B \propto \rho^{-1/2} T^{1/2}. \tag{4.52}$$

Combining equations (4.51) and (4.52), we obtain a model for the conductivity in the form $\tilde{\kappa} \propto T^{1/6}\rho^{-1/2}$, i.e. $n_T = 1/6$ and $n_\rho = -1/2$. We fix the overall strength by alluding to measurements in our own Galaxy (Berezinskii et al. 1990, Schlickeiser 2002), which estimate a diffusivity along the magnetic field lines in the interstellar medium of approximately

$$\kappa_{\rm ISM} \approx 3 \times 10^{27} \frac{\rm cm^2}{\rm s} \approx 10\, \frac{\rm kpc^2}{\rm Gyr} \tag{4.53}$$

Adopting typical temperature and density values of the ISM as reference values, we end up with the following model for the diffusivity

$$\tilde{\kappa} = 10 \frac{\rm kpc^2}{\rm Gyr} \left(\frac{T}{10^4 {\rm K}}\right)^{1/6} \left(\frac{\rho}{10^6 {\rm M_\odot kpc^{-3}}}\right)^{-1/2} \tag{4.54}$$

We use this parameterization in the simulations with diffusion analysed in the this study. It is clear however that this model needs to be taken with a grain of salt. The actual diffusivity is highly uncertain, and may vary widely between different parts of the Universe. Improving the physical understanding of the strength of the diffusion will therefore remain an important goal for cosmic ray physics in the future.

4.4.2. Discretizing the diffusion equation

We still have to discuss how we numerically implement diffusion in our Lagrangian SPH code. We follow a similar strategy as laid out in chapter 3 (and correspondingly in Jubelgas et al. (2004)), where a new treatment of thermal conduction in SPH is discussed and applied to simulations of clusters of galaxies. In essence, the techniques used to solve the heat diffusion equation can in a mostly identical fashion be applied to solve cosmic ray diffusion, as presented here.

For a power-law momentum dependence of

$$\kappa(p) = \tilde{\kappa}\, p^{d_p}, \tag{4.55}$$

we start from the diffusion equations in a Lagrangian form that is matched to the variables evolved in our simulation code, i.e.

$$\rho \frac{{\rm d}\tilde{\varepsilon}}{{\rm d}t} = \boldsymbol{\nabla} \tilde{\kappa} \boldsymbol{\nabla} D_\varepsilon \tag{4.56}$$

and

$$\rho \frac{{\rm d}\tilde{n}}{{\rm d}t} = \boldsymbol{\nabla} \tilde{\kappa} \boldsymbol{\nabla} D_n, \tag{4.57}$$

where we define, for clarity,

$$D_\varepsilon = \frac{\alpha - 1}{\alpha - 1 - d_p} \rho\, q^{d_p} \frac{T_{\rm CR}(\alpha - d_p, q)}{T_{\rm CR}(\alpha, q)}\, \tilde{\varepsilon} \tag{4.58}$$

and

$$D_n = \frac{\alpha - 1}{\alpha - 1 - d_p} \rho\, q^{d_p}\, \tilde{n} \tag{4.59}$$

respectively. This method for representing the equations in SPH is based on a discretisation scheme for the Laplace operator that avoids second order derivatives of the SPH kernel (Brookshaw 1985, Monaghan

1992), which makes the scheme robust against particle disorder and numerical noise. We end up with an equation of the form of

$$\frac{\mathrm{d}\tilde{\varepsilon}_i}{\mathrm{d}t} = \sum_j \frac{m_j}{\rho_i \rho_j} \frac{2\overline{\kappa}_{ij}(\overline{D}_{\varepsilon,j} - D_{\varepsilon,i})}{|\boldsymbol{x}_{ij}|^2} \boldsymbol{x}_{ij} \boldsymbol{\nabla}_i W_{ij}, \tag{4.60}$$

and mutatis mutandis for the cosmic ray number density. Here, we introduce a symmetrization of the diffusivities according to

$$\overline{\kappa}_{ij} = 2\frac{\tilde{\kappa}_i \tilde{\kappa}_j}{\tilde{\kappa}_i + \tilde{\kappa}_j}, \tag{4.61}$$

based on the suggestion by Cleary & Monaghan (1999). Furthermore, we replace one of the D_ε terms in the pairwise diffusion term with the respective kernel interpolant

$$\overline{D}_{\varepsilon,j} = \sum_k \frac{m_k D_{\varepsilon,k}}{\rho_k} W_{jk}. \tag{4.62}$$

As seen in chapter 3, such a mixed formulation between intrinsic particle variables and SPH-smoothed interpolants substantially improves the numerical stability against small-scale particle noise. The smoothing process suppresses strong small-scale gradients, while long-range variations and their diffusive evolution remain unaffected. Since we use an explicit time integration scheme, this behaviour prevents stability problems due to the typical ‘overshooting’ problem that otherwise may arise in presence of strong local gradients from local outliers.

Nevertheless, we are still required to impose a comparatively strict timestep criterion to ensure proper integration of the diffusion. For the thermal conduction problem, we employ a simple criterion that limits the relative change of thermal energy of a particle within a single timestep. Although the diffusion studied here substancially is very similar to the conduction problem, an equivalent criterion does not appear to be a preferrable choice, simply because, unlike for thermal conduction, the relevant reservoir can often be empty. In fact, we typically start simulations from initial conditions where all the cosmic ray particle densities are identical to zero.

A closer look at the Green’s function $G(\boldsymbol{x}, t) = (4\pi\kappa t)^{-3/2} \exp[-\boldsymbol{x}^2/(4\kappa t)]$ of the diffusion process shows that differences between two points with a distance of $|\boldsymbol{x}|$ are diffused away with a characteristic timescale $\boldsymbol{x}^2/\kappa$. Using the mean interparticle separation of SPH particles for this distance intrinsically suggests a definition of a diffusion timescale as

$$t_{\mathrm{diff}} = \frac{1}{\kappa}\left(\frac{m}{\rho}\right)^{2/3}. \tag{4.63}$$

We use this to constrain the maximum timestep for particles to

$$\Delta t < \varepsilon\, t_{\mathrm{diff}} = \varepsilon \frac{1}{\kappa}\left(\frac{m}{\rho}\right)^{2/3} \tag{4.64}$$

where we use a fiducial value of $\varepsilon = 0.1$ for the simulations presented in this study. This provides us with a numerically stable cosmic ray diffusion while at the same time time seps are prevented from becoming impractically small.

As an additional refinement to the scheme, we have implemented the method laid out in chapter 3 that enables us to obtain a manifestly conservative scheme for cosmic ray energy and particle number, even when using individual and adaptive timesteps. To this end, we rewrite equation (4.60) as

$$m_i \frac{\mathrm{d}\tilde{\varepsilon}_i}{\mathrm{d}t} = \sum_j \frac{\mathrm{d}E_{ij}}{\mathrm{d}t}, \tag{4.65}$$

where we define a pairwise exchange term of cosmic ray energy

$$\frac{\mathrm{d}E_{ij}}{\mathrm{d}t} = \frac{m_i m_j}{\rho_i \rho_j} \frac{2\overline{\kappa}_{ij}(\overline{D}_{\varepsilon,j} - D_{\varepsilon,i})}{|\boldsymbol{x}_{ij}|^2} \boldsymbol{x}_{ij} \boldsymbol{\nabla}_i W_{ij}. \tag{4.66}$$

In each system step, we now determine the change of the cosmic ray energy of particle i according to

$$m_i \Delta\tilde{\varepsilon}_i = \frac{1}{2} \sum_{jk} \Delta t_j (\delta_{ij} - \delta_{ik}) \frac{\mathrm{d}E_{jk}}{\mathrm{d}t}. \tag{4.67}$$

The double sum on the right can be simply evaluated by the ordinary SPH sums over the active particles, provided that for each neighbour j found for a particle i a change of $\Delta t_i \dot{E}_{ij}/2$ for i is recorded, and a change of $-\Delta t_i \dot{E}_{ij}/2$ for the particle j. We apply the accumulated changes of the cosmic ray energy (or particle number) to *all* particles at the end of the step, i.e. not only to the ones that are active on the current timestep. This way, we constitute a scheme that manifestly conserves total cosmic ray energy and number density for each diffusive step.

Finally, use a further refinement to cope with technical problems associated with a situation where isolated CR-pressurized particles are embedded in a background of particles with zero CR pressure. In the neighbourhood of such an isolated particle, the smoothed cosmic ray energy field $\overline{D}_{\varepsilon,j}$ is non-zero for particles that have themselves no CR component (yet). This can in turn cause exchange terms E_{ij} between two cosmic-ray pristine particles, leading to unphysical negative values for the energy in one of them. We find that this can be avoided by limiting the value of the interpolant $\overline{D}_{\varepsilon,i}$ to be no more than a fiducial factor $\chi \simeq 2.0$ larger than the value $D_{\varepsilon,i}$ for the particle itself. With this change, we recover numerical stability of the diffusion even in this extreme scenario.

4.5. Numerical details and tests

The numerical framework for cosmic ray physics presented above allows for very complex dynamics that interacts in non-linear and rather non-trivial manner with different aspects of ordinary hydrodynamics, and in particular with the physics of radiative cooling and star formation included in GADGET-2 to describe galaxy formation. Together with the nearly complete absence of analytic solutions, this makes a direct validation of the numerical implementation of cosmic ray physics in the simulation code particularly hard.

However, there are a few areas where the careful checks of individual subroutines of the code that we carried out can be augmented with tests of problems with known analytical solutions. One such area are hydrodynamical shock waves that involve a cosmic ray pressure component. Comparison of numerical results with the analytic solution provides a test the most interesting dynamical aspects of cosmic ray physics; the introduction of a variable adiabatic index γ. Note that the pressure of such a 'hybrid' or 'compound gas' with a thermal and a cosmic ray energy density can no longer be suitably described with the simple parameterizations used for a polytropic gas. In particular, both the relative contribution of the cosmic ray pressure and the adiabatic index of the CR pressure component itself will change during an adiabatic compression. While more complex than for an ideal gas, the Riemann problem for a shocks in such a composite gas can be solved analytically (Pfrommer et al. 2006), and we use this as a test case for our numerical scheme.

Another aspect which can be tested with simple toy set-ups is the diffusion of cosmic rays. To this end we consider a geometrically simple initial cosmic ray distribution, with gas particles being forced to be at rest (such effectively constituting a solid body). This enables us to test the correctness of diffusion speed, and the conservative properties of the diffusion process.

4.5.1. Implementation issues

The treatment of a new physical process in SPH often requires an adaption of the timestep criterion to ensure proper time integration of the added physics. In the case of cosmic ray driven dynamics, it turns out that an additional limit on the timestep is not really required though, because the Courant criterion for hydrodynamics is already general enough and automatically adjusts timesteps where required by the cosmic ray dynamics, as the latter then induces a larger sound speed due to extra cosmic ray pressure. The non-adiabatic source and sink terms on the other hand are essentially encapsulated in subresolution models, and threare therefore not particularly demanding with respect to the integration timestep.

As seen in equations (4.10) and (4.12), calculating physical properties like pressure and specific energy of the cosmic ray component involves the evaluation of incomplete beta functions, which can be rather expensive numerically. In the individual timestep scheme of GADGET-2, which is essential for simulations with a large dynamic range, the pressure data for all SPH particles need to be updated with every system step, even if a particle is 'passive' and does not require a force computation itself in the current step. Clearly, a costly evaluation of special functions for the pressure would therefore imply a significant burden in terms of processor time. We have therefore implemented a series of look-up tables discretized in $\log q$ that allow for a fast evaluation of terms involving costly incomplete beta functions. Interpolating from these tables allows for a rapid and accurate computation of all cosmic ray related quantities without special function evaluations during the simulation.

The same technique is also used to numerically invert the specific energy $T_{\rm CR}$ of equation (4.10) for q, a task that arises when the mean CR energy is updated. Again, we resort to a pre-computed look-up table in which we locate the new mean CR energy, and interpolate in the table to determine the spectral cutoff q. Once the spectral cutoff and injected CR-to-baryon fraction is found, the new spectral normalization

$\tilde{C}$ can be computed from equation (4.9). As a final step, we update the effective hydrodynamic pressure due to cosmic rays of the particle in question.

For treating Coulomb losses in an accurate and robust way, we use an implicit scheme because of the very sensitive dependence of the cooling rate on the spectral cut-off q. In fact, in order to ensure that this cooling process leaves the normalization of the spectrum constant and only increases the amplitude q, we solve the following implicit equation

$$\tilde{\varepsilon}(q', \tilde{C}) = \tilde{\varepsilon}(q, \tilde{C}) - \frac{\tilde{\varepsilon}(q', \tilde{C})}{\tau_{\rm C}(q')}\Delta t \tag{4.68}$$

for a new spectral cut-off q' when the cooling lasts for a time interval Δt. This scheme is robust even in cases where Δt exceeds $\tau_{\rm C}(q)$. Unlike the Coulomb losses, the timescale of hadronic losses is comparatively long and varies little with the spectral cut-off, as seen in Figure 4.4. It therefore is easier to integrate accurately and not necessary to resort to an implicit solver.

4.5.2. Shocks in cosmic ray pressurized gas

In the following, we show the results of a series of three-dimensional test simulations that trace a shock wave in a rectangular slab of gas, elongated along one spatial dimension. Periodic boundary conditions in the directions perpendicular to this axis are used to make sure that no boundary-effects occur. This allows the simulation a planar shock in 3D to be compared with a corresponding one-dimensional analytic solution. The initial conditions of our shock-tube tests were set-up with relaxed 'glass' structures of particles initially at rest, and by giving the two halves of the slab different temperatures and cosmic ray pressures. The particle mass was constant and chosen such that the mean particle spacing was 1 length unit in the high-density regime. While a reduction of the particle mass in the low-density region would have resulted in an increased spatial resolution there, our constant particle mass set-up is more appropriate for the conditions encountered in cosmological simulations.

In Figure 4.6, we show the state of the system after a time of $t = 0.3$, for an initial density contrast of 5, a total pressure ratio of 35.674, a homogeneous mixture of $1/3$ cosmic ray pressure and $2/3$ thermal pressure contribution on the left-hand side, and pressure equilibrium between CRs and thermal gas on the right-hand side. A shock with Mach number $M = 3$ travelling to the right, a rarefaction wave to the left, and a contact discontinuity in between develop for these initial conditions. The analytically predicted shock front position and density distribution are matched nicely by the simulation. Due to the smooth nature of SPH simulations, the density jump at the shock at $x \simeq 430$ is not a sharp discontinuity, but rather spans over a length corresponding to a small number of mean interparticle spacings. The contact discontinuity at $x \simeq 375$ is reproduced well, with only a small 'blib' seen in both the density and the pressure profile, which is characteristic for SPH simulations in shock tube tests. Note that cosmic ray pressure dominates over thermal pressure on the left side of the contact discontinuity due to adiabatic rarefaction of the initially already CR-dominated state on the left-hand side, while this ratio of contributions is substantially reversed on the other side because CRs are adiabatically compressed at the shock while the thermal gas experiences entropy injection. The rarefaction wave traveling to

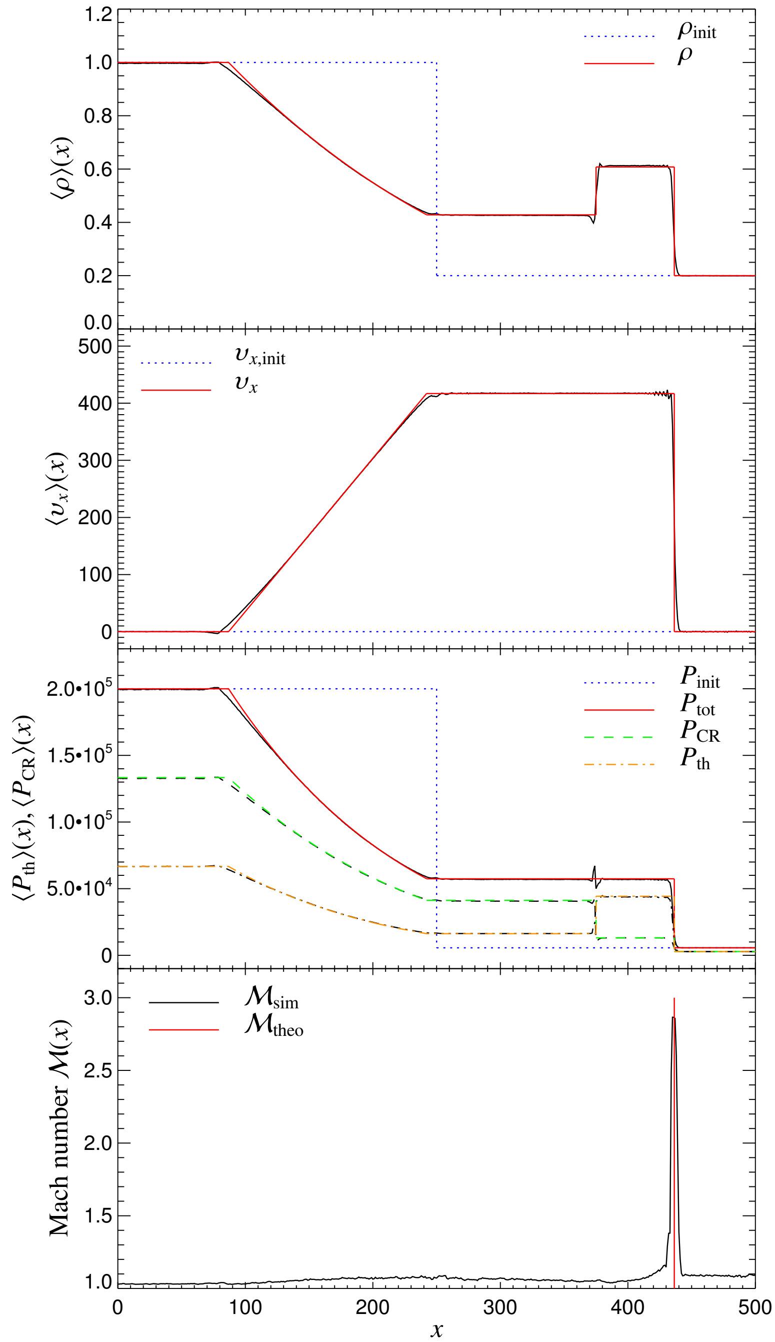

Figure 4.6.: Shock-tube test for a gas with thermal and cosmic ray pressure components. The simulation is carried out in a three-dimensional periodic box which is longer in the x-direction than in the other two dimensions. Initially, the relative CR pressure is $X_{\rm CR} = P_{\rm CR}/P_{\rm th} = 2$ in the left half-space ($x < 250$), while we assume pressure equilibrium between CRs and thermal gas for $x > 250$. The evolution then produces a Mach number $\mathcal{M} = 3$ shock wave. The numerical result of the volume averaged hydrodynamical quantities $\langle\rho(x)\rangle$, $\langle P(x)\rangle$, $\langle v_x(x)\rangle$, and $\langle\mathcal{M}(x)\rangle$ within bins with a spacing equal to the interparticle separation of the denser medium is shown in black and compared with the analytic result shown in colour.

the left shows the expected behaviour over most of its extent, only featuring small differences between numerical and analytical solutions in the leftmost parts at $x \simeq 100$. However, the overall agreement is very reassuring, despite the fact that here a shock in a composite gas was simulated.

The simulation code is able to correctly follow rapid compressions and rarefactions in a gas with substantial cosmic ray pressure support, including shocks that feed their dissipated energy into the thermal component. In cosmological simulations where diffusive shock acceleration of cosmic rays is included, some of the dissipated energy instead is fed into the cosmic ray reservoir, so that there the resulting shock behaviours can be yet more complicated. The employed shock detection technique (Pfrommer et al. 2006) is able to correctly identify the shock location on-the-fly during the simulation, and provides the right Mach number in the peak of the shock profile, where most of the energy is dissipated. We use this to accurately describe the Mach-number dependent shock-injection efficiency of cosmic rays in shocks.

4.5.3. Cosmic ray diffusion

In order to test the diffusion part of the code in a clean way, we employ a system of gas particles that are forced to be at rest, avoiding complications caused to the motions of particles. We achieve this by setting all particle accelerations to zero, such that the gas in fact behaves essentially like a solid body. As a side effect, the densities remain constant over time, such that all variations in the distribution of cosmic rays must plausibly be results of diffusive transport (we also disabled Coloumb and catastrophic losses for this test). For this idealized situation, analytic solutions for the diffusion problem can be derived and readily compared with numerical results.

For definiteness, we set up a periodic slab of matter with density $1 \times 10^{10} \mathrm{M}_{\odot} \mathrm{kpc}^{-3}$, spanning a basic volume of $10 \times 10 \times 100$kpc. The periodicity across the short dimensions ensures the absence of boundary effects, such that we can compare the numerical results to effectively one-dimensional analytic solutions. The cosmic ray distribution was initialized such that the energy density due to relativistic particles has a sharp step. The spectral cutoff at both sides of the step was equally set to $q = 0.3$ in the present test, but similar results are also obtained for different choices. Again, we use an irregular glass-like configuration as initial particle distribution in order to more realistically model the noise properties in density fields encountered in cosmological applications. As mentioned in the above, small-scale numerical noise can cause problems in the treatment of diffusion, so the inclusion of numerical noise in the initial conditions is an important aspect for testing the robustness of the scheme.

In real physical applications, the diffusion implementation has to cope with spatially varying diffusion coefficients. In particular, steep gradients in the diffusivity are found at phase transitions between the cold, dense gas and the hot, yet thin ambient intergalactic and intra-cluster medium in clusters of galaxies. It is therefore advisable to verify that the implemented numerical scheme for the diffusion is well behaved at sharp jumps of the diffusivity. We incorporate this aspect into the test scenario by setting up a fiducial temperature-dependent cosmic ray diffusivity of

$$\tilde{\kappa} = 1.0 \frac{\mathrm{kpc}^2}{\mathrm{Gyr}} \left(\frac{T}{1000\mathrm{K}} \right) \tag{4.69}$$

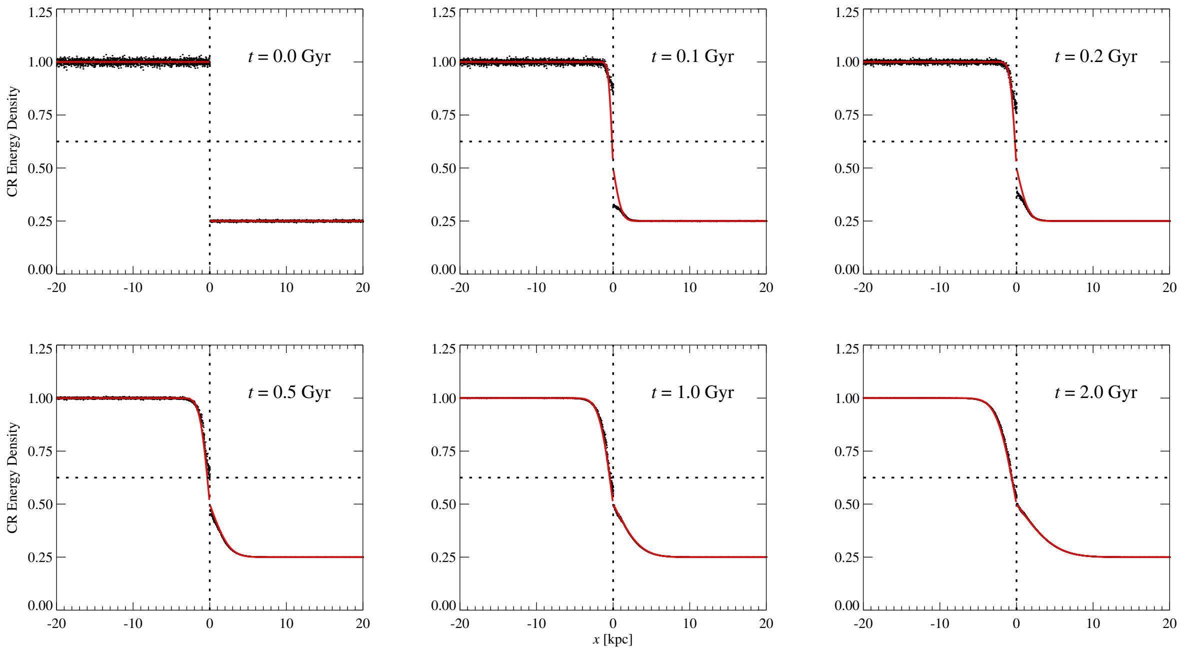

Figure 4.7.: Time evolution of a step function in cosmic ray energy density due to diffusion (the spectral cut-off and slope of the cosmic rays are constant throughout the volume). The population of SPH particles is kept at rest. The times shown in the different panels are (from top left to bottom right): $t = 0$, 0.1, 0.2, 0.5, 1.0 and 2.0 Gyr. Black dots give particle values at the corresponding time, while the red line shows the analytical solution. The diffusivity $\tilde{\kappa}$ is constant at 1 kpc^2 Gyr^{-1} on the left hand side, and four times higher on the right hand side.

and varying the gas temperature from 1000K in the left half of the matter slab to 4000K in the right, causing an increase of the diffusivity by a factor of 4 across the $x = 0$ plane. Of course, this particular choice of diffusivity is arbitrary, but the chosen values are not too dissimilar compared with what we will encounter in cosmological simulations later on. We further assume a momentum independent diffusivity ($\kappa(p) = \tilde{\kappa}$) to allow for a comparison of the implementation results with an analytic solution, in analogy to those for thermal conduction as found e.g. in Cleary & Monaghan (1999).

In Figure 4.7, we present the time evolution for diffusion of an initial step function. The simulation was run over a time span of 2 Gyr, and for a number of times in between, we compare the spatial distribution of the cosmic ray energy density obtained numerically with the analytical solution for the problem (shown in red). The match of the numerical result and the analytic solution is very good, especially at late times. In fact, after $t = 1$ Gyr, we no longer see any significant deviation between the numerical solution and the analytical one. The code reliably traces the flattening of the cosmic energy density jump over time. The largest differences occur in the very early phases of the evolution, at around the initial discontinuity, as expected. Due to the smoothing inherent in SPH and our diffusion formulation, sharp gradients on very small-scales are washed out only with some delay, but these errors tend to not propagate to larger scales, such that the diffusion speed of large-scale gradients is approximately correct.

Note that small-scale noise present in the initial cosmic ray energy distribution is damped out with different speeds in the left and right parts of the slab. This is due to the different conductivities in the low- and high-energy regimes, which give rise to characteristic diffusion timescales of $t_{\rm diff} = 1\,$Gyr and $t_{\rm diff} = 0.25\,$Gyr, respectively, for the mean interparticle separation of 1 kpc, consistent with Eqn. (4.63). We note that we have verified the good accuracy of the diffusion results for a wide range of matter densities and diffusivities, also including cases with stronger spatial variations in diffusivity. We are hence confident that the presented numerical implementation scheme produces accurate and robust results in full cosmological simulations, where the diffusivity can show non-trivial spatial dependencies.

4.6. Simulations of isolated galaxies and halos

Let us turn to a discussion of the effects of our cosmic ray model on the galaxy formation process. Due to the complexity of the involved physics, which couples radiative cooling, star formation, supernova feedback, cosmic ray physics, self-gravity, and ordinary hydrodynamics, it is clear that our analysis cannot be fully exhaustive in this methodology study. Instead, our strategy is to provide a first exploration of the most important effects using a set of simulations with idealized initial conditions, and a restricted set of full cosmological simulations. This may then guide further in-depth studies of the individual effects.

One of the possible effects of cosmic ray physics is that to the regulation of star formation by feedback due to the injection of CRs from supernovae may. This could alter the regulation of star formation by feedback, which may directly translate into observable differences in forming galaxies. CR-pressurized gas has a different equation of state than ordinary thermal gas, so it may even begin to rise buoyantly from star-forming regions, which could help to produce outflows from galactic halos. Also, because energy stored in cosmic rays is subject to different dissipative losses than thermal gas, we expect that the radiative cooling of galaxies could be altered. Of special importance is also whether the strength of any of these effects shows a dependence on halo mass, because a change of the efficiency of galaxy formation as a function of halo mass is expected to modify the shape of the resulting galaxy luminosity function.

Another intriguing possibility is that the total baryonic fraction ending up in galactic halos could be modified by the additional pressure component provided by the relativistic particle population. In particular, the softer equation of state of the cosmic-ray gas component (its adiabatic index varies in the range $4/3 < \gamma_{\rm CR} < 5/3$) could increase the concentration of baryonic matter in dark matter potential wells, because the pressure increases less strongly when the composite CR/thermal gas is compressed. On the other hand, a partial cosmic ray pressure support might reduce the overall cooling efficiency of gas in halos, causing a reduction of the condensated phase of cold gas in the centres.

To examine the non-linear interplay of all these effects, we study them in a number of different scenarios. We first use isolated galaxy models which allow for a precise control over the initial conditions and an easy analysis and interpretation of the results. Next, we use non-radiative cosmological simulations to investigate the efficiency of CR production at structure formation shock waves. In the further, we use high-resolution cosmological simulations that include radiative cooling and star formation to study the formation of dwarf galaxies, aiming to see whether the identified mass trends are also present in the full cosmological setting. We further use these simulations to investigate whether CRs influence the absorption properties of the intergalactic medium at high redshift. Finally, we use high-resolution 'zoomed' simulations of the formation of clusters of galaxies to study how CR injection by accretion shocks and supernovae modifies the thermodynamic properties of the gas within halos.

4.6.1. Formation of disk galaxies in isolation

As a simple model for the effects of cosmic ray feedback on disk galaxy formation, we consider the time evolution of the gas atmospheres inside isolated dark matter halos. The initial conditions consist of a dark matter potential with a structure motivated from cosmological simulations, combined with a hydrostatic gas distribution initially in equilibrium within the halo. We consider the evolution of this system under radiative cooling, star formation and cosmic ray production by supernovae. We expect the gas in the centre to lose its pressure support by cooling, and to collapse into a rotationally supported disk that forms inside-out (Fall & Efstathiou 1980).

It is obvious that this is a highly idealized model for disk galaxy formation, which glosses over the fact that in a more realistic cosmological setting galaxies originate in a hierarchical process from the gravitational amplification of density fluctuation in the primordial mass distribution, gradually growing by accretion and merging with other halos into larger objects. However, the simplified should still be able to capture some of the basic processes affecting this hierarchy in a particular clean way that enables us to identify trends due with galaxy mass due to cosmic rays.

We model the dark matter and baryonic content contained in the isolated halos as NFW density profiles (Navarro, Frenk & White 1996), slightly softened at the centre to introduce a core into the gas density, with a maximum density value lying below the threshold for star formation, and allow for a 'quiet' start of the simulations. The velocity dispersion of the dark matter and the temperature of the gas were chosen in a way as to ensure that the halos are in equilibrium initially, i.e. when evolved without radiative cooling, the model halos are perfectly stable for times of order the Hubble time. We also impart angular momentum onto the halo with a distribution inside the halo that is consistent with results obtained from full cosmological simulations (Bullock et al. 2001).

We simulated a series of host halos with masses, systematically varying from $10^9\,\mathrm{M_\odot} h^{-1}$ to $10^{12}\,\mathrm{M_\odot} h^{-1}$. In all cases, we adopt a baryon fraction of $\Omega_\mathrm{b}/\Omega_\mathrm{m} = 0.133$, and a matter density of $\Omega_\mathrm{m} = 0.3$. We typically represent the gas with 10^5 particles and the dark matter with twice as many. In some of our simulations, we also replaced the live dark halo with an equivalent static dark matter potential to speed up the calculations. In this case, the contraction of the dark matter due to baryonic infall is not accounted for, but this has a negligible influence on our results. We have kept the concentration of the NFW halos fixed at a value of $c = 12$ along the mass sequence, such that the initial conditions are scaled versions of each other which would evolve in a self-similar way if only gravity and ideal hydrodynamics were considered. However, this scale-invariance is broken by the physics of cooling, star formation and cosmic rays.

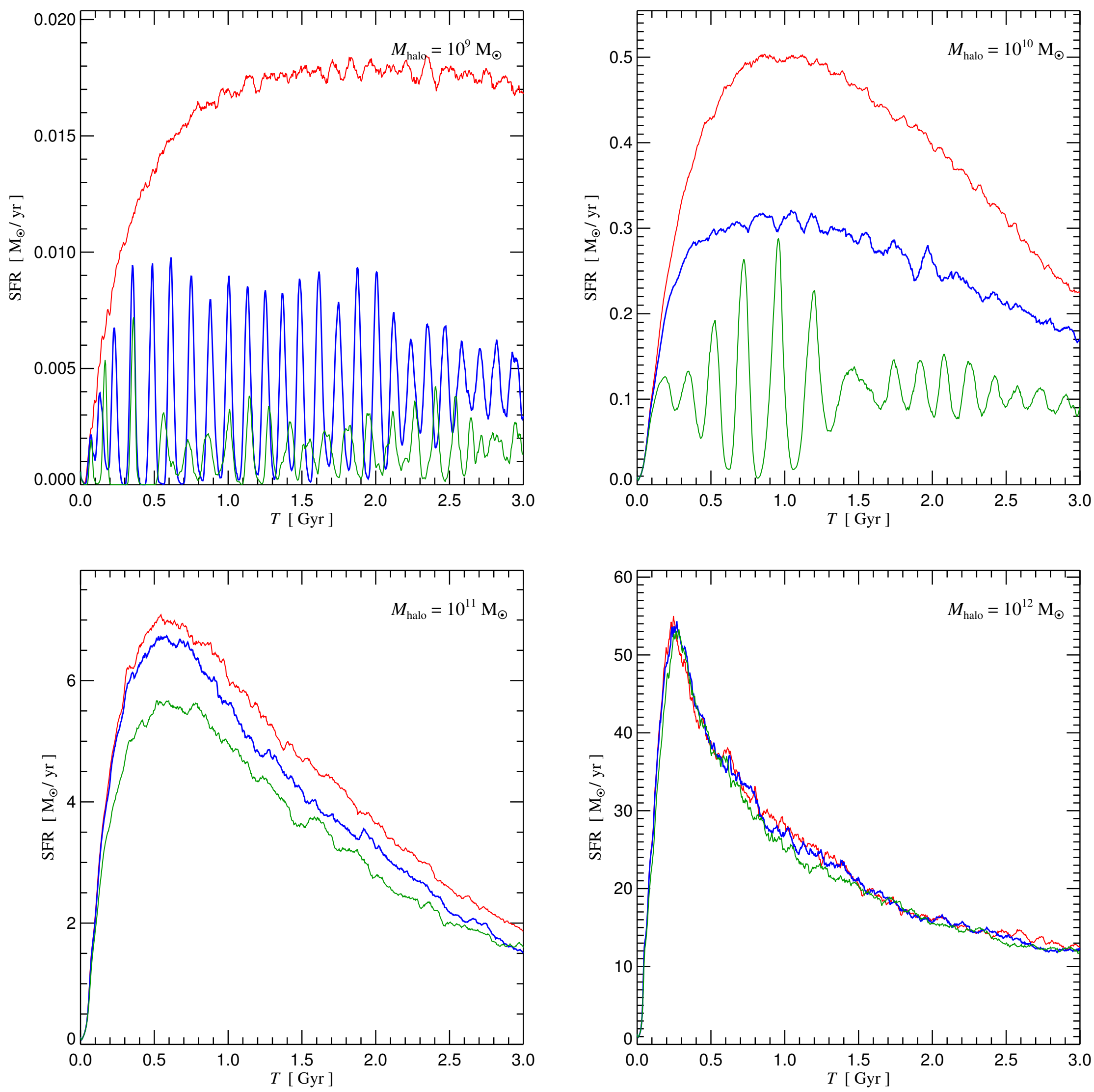

Figure 4.8.: Time evolution of the star formation rate in isolated halos of different mass which are initially in virial equilibrium. In each panel, we compare the star formation rate in simulations without cosmic ray physics (solid red line) to two runs with different injection efficiency of cosmic rays by supernovae, $\zeta_{SN} = 0.1$ (blue lines) and $\zeta_{SN} = 0.3$ (green lines), respectively. From top left to bottom right, results for halos of virial mass $10^9\,M_\odot h^{-1}$ to $10^{12}\,M_\odot h^{-1}$ are shown, as indicated in the panels. Efficient production of cosmic rays can significantly reduce the star formation rate in very small galaxies, but it has no effect in massive systems.

When evolved forward in time, radiative cooling leads to a pressure loss of the gas in the centres of the halos, which then collapses and settles into a rotationally supported cold disks. In these disks, the gas is compressed by self-gravity to sufficiently high densities for star formation to ensue. Unfortunately, the physics of star formation is not understood in detail yet, and we also lack the huge dynamic range in resolution that would be necessary do directly follow the formation and fragmentation of individual star-forming molecular clouds in simulations of whole galaxies. Therefore, in this study, we invoke the sub-resolution treatment for star formation and feedback processes, as described in chater 2.

In the presented new cosmic ray model, a fraction of the deposited supernova energy is invested into the acceleration of relativistic protons, and hence is lost to the ordinary feedback cycle. While this energy no longer directly influences the star formation rate, it has an indirect effect on the star-forming gas by providing a pressure component that is not subject to the usual radiative cooling. If this pressure component prevails sufficiently long, it can cause the gas to expand and to lower its density, thus leading to a reduction of the star formation rate.

Figure 4.8 shows the time evolution of the star formation rate for four different halos masses, ranging from $10^9\,h^{-1}\mathrm{M}_\odot$ to $10^{12}\,h^{-1}\mathrm{M}_\odot$, and each comparing three different cases respectively, a reference simulation using the ordinary model as laid out above without any cosmic rays dynamics whatsoever, and two simulations including cosmic ray production in supernova explosions (without allowing for diffusion), the latter two differing only in the assumed efficiency of $\zeta_{\mathrm{SN}} = 0.1$ and $\zeta_{\mathrm{SN}} = 0.3$ for this process, respectively. Interestingly, the simulations with cosmic rays show a substantial reduction of the star formation rate for the two small mass systems, but for the $10^{11}\,h^{-1}\mathrm{M}_\odot$ halo the effects already gets small in relation, and for the massive halo of mass $10^{12}\,h^{-1}\mathrm{M}_\odot$, no significant differences between the three simulans can be detected. Evidently, the ability of cosmic ray feedback to counteract star formation shows a strong mass dependence, with small systems being affected most prominently. Higher efficiencies ζ_{SN} of CR-production by supernovae, as could be expected, lead to stronger reduction of the star formation rate.

Figure 4.9 provides an explanation for this result, and also elucidates the origin of the oscillatory behaviour of the SFR in the CR-suppressed cases. In the figure, we show phase-space diagrams of the gas particles of the $10^9\,h^{-1}\mathrm{M}_\odot$ and $10^{12}\,h^{-1}\mathrm{M}_\odot$ halos, respectively, in a plane of effective temperature versus density. We plot the thermal pressure and the cosmic ray pressure separately. In order to cleanly show whether a dynamical effect of cosmic rays can be expected, we here use a fiducial simulation where the cosmic ray pressure is ignored for the evaluation of the equations of motion, but in all other aspects is computed with the full dynamical model. Figure 4.9 demonstrates the bulk of the star-forming gas in the massive halo residing at much larger densities and effective pressures than in the low mass halo. Because the cosmic ray pressure exceeds the effective thermal pressure of the multi-phase ISM only for moderate overdensities (relative to the star formation threshold), most of the gas in the $10^{12}\,h^{-1}\mathrm{M}_\odot$ halo is too dense to be affected by the cosmic ray pressure. The relative contributions of the two pressure components are consistent with the analytic expectations shown in Figure 4.5. In fact, these expectations are replicated as dashed lines in Figure 4.9 and are traced well by the bulk of the particles. Because the shallower potential wells in low-mass halos are unable to compress the gas to comparably high overdensities as in

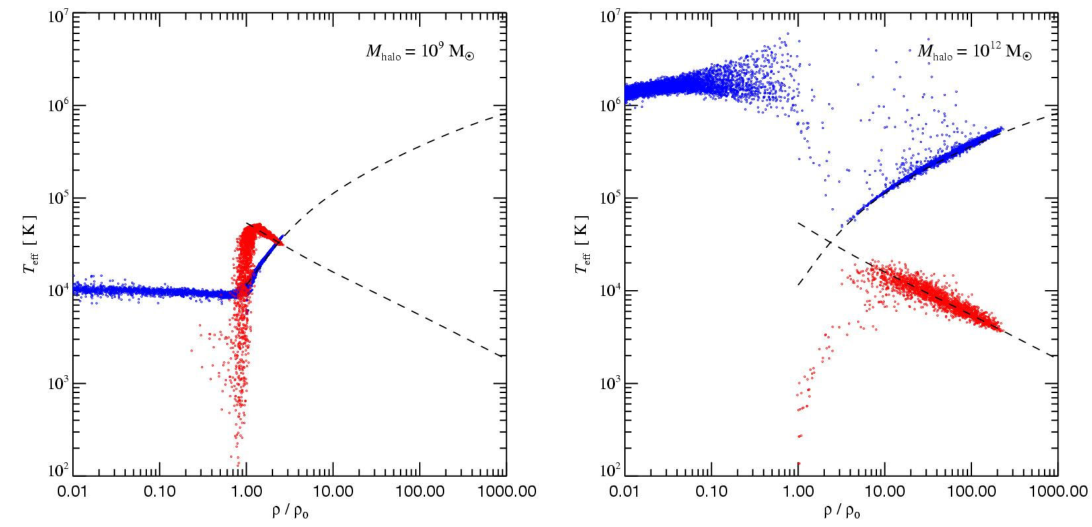

Figure 4.9.: Phase-space diagram of the star-forming phase in two simulations with halos of different mass. In these fiducial simulations, we included cosmic ray physics but ignored the cosmic ray pressure in the equations of motion, i.e. there is no dynamical feedback by cosmic rays. However, a comparison of the cosmic ray pressure and the thermal pressure allows us to clearly identify regions where the cosmic rays should have had an effect. For graphical clarity, we plot the pressures in terms of a corresponding effective temperature, $T_{\rm eff} = (\mu/k)P/\rho$. Above the star formation threshold, the small galaxy of mass $10^9\,{\rm M}_\odot h^{-1}$ shown in the left panel has a lot of gas in the low-density arm of the effective equation of state, shown by the curved dashed line. On the other hand, the massive $10^{12}\,{\rm M}_\odot h^{-1}$ galaxy shown on the right has characteristically higher densities in the ISM. As a result, the cosmic ray pressure is insufficient to affect this galaxy significantly. Note that the falling dashed line marks the expected location where cosmic ray loss processes balance the production of cosmic rays by supernovae. We show the systems at time $t = 2.0$ Gyr after the start of the evolution.

high-mass halos against the effective pressure of the ISM, it is not surprising that the cosmic ray pressure becomes dynamically important only in small systems.

Figure 4.9 clearly shows that in the regime where cosmic ray pressure may dominate we cannot expect a dynamically stable quasi-equilibrium state with a quiescent evolution of the star formation rate. This is due to the decline of the effective cosmic ray pressure with increasing density of the ISM, a situation which cannot result in a stable equilibrium configuration where self-gravity is balanced by the cosmic ray pressure. Instead, the system should be intrinsically instable in this regime. When some gas becomes dense enough to start star formation, it at first has no cosmic ray pressure support but it is stabilized against collapse by the thermal pressure of the ISM that is quickly established by supernova feedback. After some time, the ongoing star formation builds up a cosmic ray pressure component, which eventually starts to dominate, at which point the gas is driven to lower density. As a result, the star formation rate declines strongly. When finally the CR pressure is dissipated, the gas collapses again. Star formation restarts and the ‘cycle’ starts its next iteration. This scenario schematically describes the origin of the

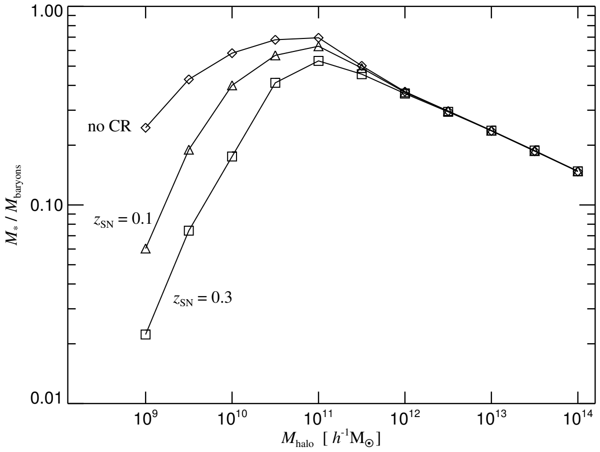

Figure 4.10.: Efficiency of star formation as a function of halo mass in our isolated disk formation simulations. We show the ratio of the stellar mass formed to the total baryonic mass in each halo, at time $t = 3.0$ Gyr after the start of the simulations, and for two different efficiencies of cosmic ray production by supernovae. Comparison with the case without cosmic ray physics shows that star formation is strongly suppressed in small halos, by up to a factor $\sim 10 - 20$, but large systems are essentially unaffected.

oscillations in the star formation rate seen in the results for the $10^9\,h^{-1}\mathrm{M}_\odot$ and $10^{10}\,h^{-1}\mathrm{M}_\odot$ halos when cosmic rays are included.

Another view of the halo mass dependence of the effects of cosmic ray feedback on star formation is provided in Figure 4.10. There, we show the integrated stellar mass formed up to time $t = 3$ Gyr, normalized by the total baryonic mass. Again, we compare two different injection efficiencies ($\zeta_{\rm SN} = 0.1$ and $\zeta_{\rm SN} = 0.3$) with a reference case where there is no cosmic ray physics included. In general, star formation is found to be most efficient at intermediate mass scales of $\sim 10^{11}\mathrm{M}_\odot$ in these simulations. However, the simulations with cosmic ray production show a clear reduction of their integrated star formation rate for halos with mass below a few times $10^{11}h^{-1}\mathrm{M}_\odot$, an effect that becomes *progressively stronger* for lower masses. For the $10^9\,h^{-1}\mathrm{M}_\odot$ halo, the suppression reaches more than an order of magnitude for $\zeta_{\rm SN} = 0.3$.

In Figures 4.11 and 4.12, we take a closer look at the spatial distribution of the cosmic ray pressure in the different cases, and the profiles of the stellar disks that form. To this end, we show the projected gas density distribution in an edge-on projection at time $t = 2.0$ Gyr, comparing the case without cosmic rays (left column) to the case with cosmic rays (middle column), for a range of halo masses from $10^9\,\mathrm{M}_\odot h^{-1}$ to $10^{12}\,\mathrm{M}_\odot h^{-1}$. For the simulation with cosmic rays, we overlay contours for the relative contribution of the projected cosmic ray energy to the total projected energy density. This illustrates, in particular, the spatial extent the cosmic ray pressure reaches relative to the star-forming region. Finally, the panels on the right compare surface density profiles of the stellar mass that has formed up to this time.

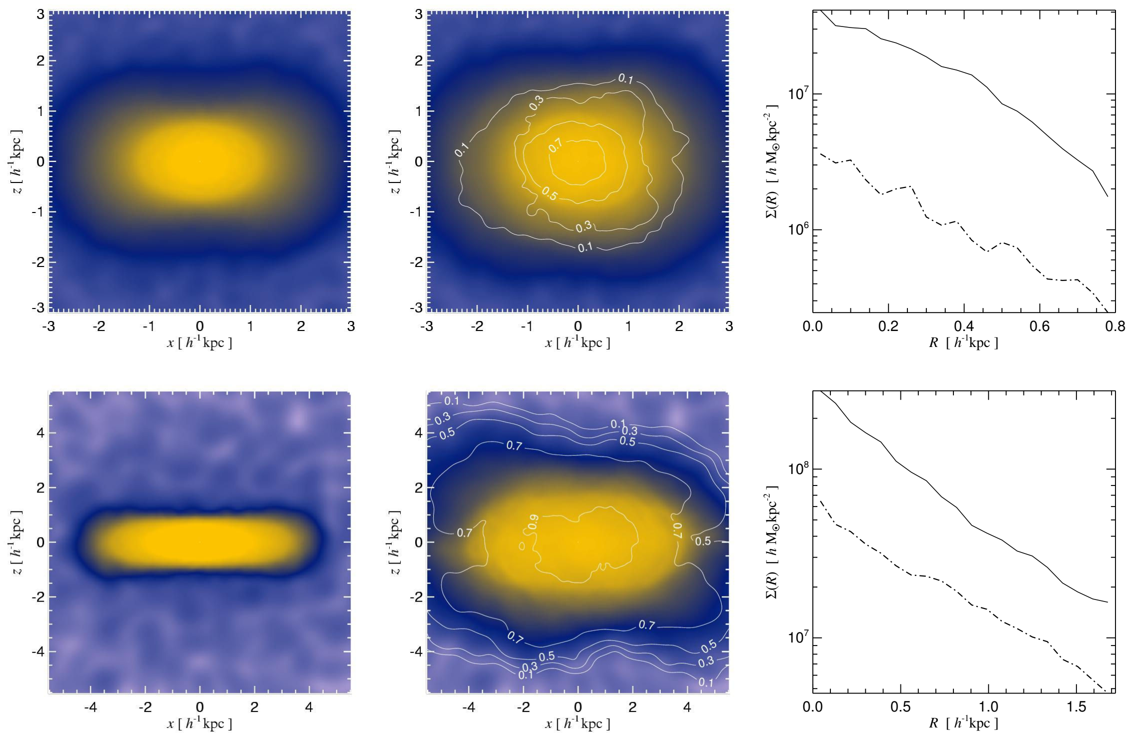

Figure 4.11.: Effect of cosmic ray feedback on star formation in simulations of isolated disk galaxy formation. Each row shows results for a different halo mass, for $M_{\rm halo} = 10^9$, 10^{10}, 10^{11} and $10^{12}\,{\rm M}_{\odot}h^{-1}$ from top to bottom. We compare the projected gas density fields at time $t = 2.0\,$Gyr of runs without cosmic ray feedback (left column) to that of runs with cosmic ray production by supernovae (middle column). The gas density field is colour-coded on a logarithmic scale. For the simulation with cosmic rays, we overplot contours that show the contribution of the projected cosmic ray energy density to the total projected energy density (i.e. thermal plus cosmic rays), with contour levels as indicated in the panels. Finally, the right column compares the azimuthally averaged stellar surface density profiles at time $t = 2.0\,$Gyr for these runs. Results for simulations without cosmic ray physics are shown with a solid line, those for simulations with CR feedback with a dot-dashed line.

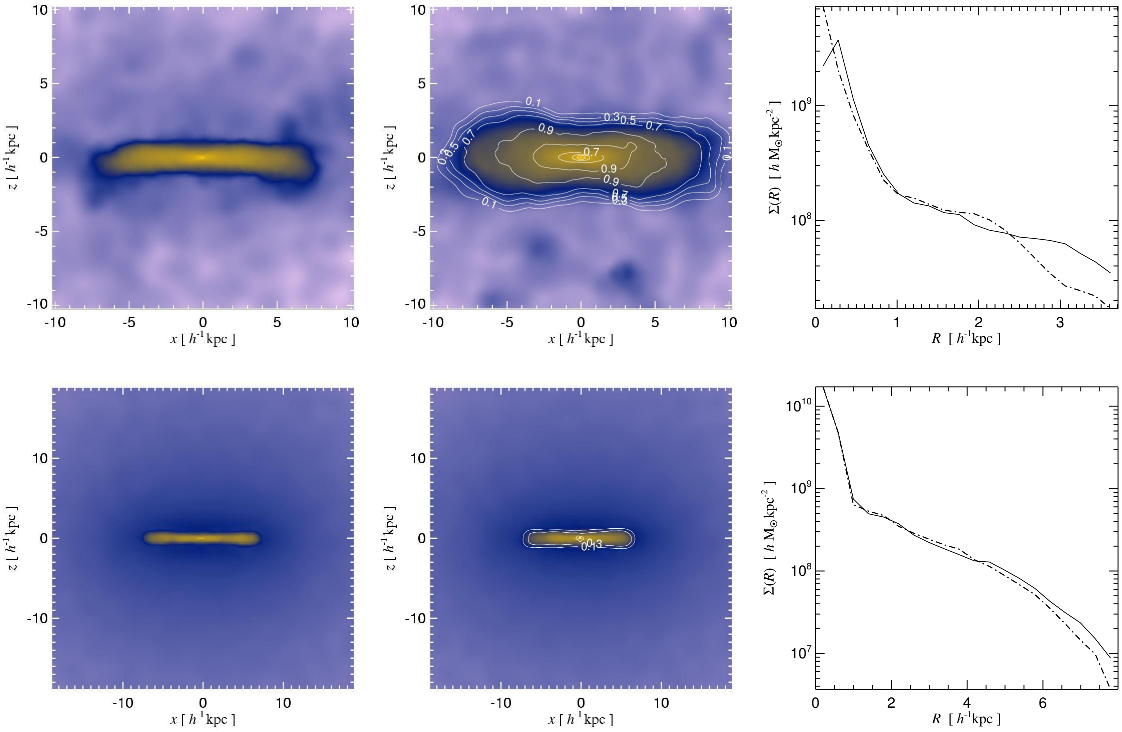

Figure 4.12.: Effect of cosmic ray feedback on star formation in simulations of isolated disk galaxy formation, as shown in figure 4.11. The rows shown here indicate the results for halo masses of $M_{\rm halo}$ = 10^{11} and 10^{12} $\rm M_{\odot}\mathit{h}^{-1}$ respectively from top to bottom.

Consistently with our earlier results, the stellar density profiles of the low mass halos show a significant suppression when cosmic rays are included, while they are essentially unaffected in the high mass range. We see the gaseous disks in the low mass halos being "puffed up" by the additional pressure of the cosmic rays. It is remarkable that in the two low-mass systems there is substantial CR pressure found at significant distance above the star-forming regions, at densities much below the star formation threshold. This is despite the fact the acceleration of relativistic particles only occurs in star-forming regions of high density within the galactic disk in these simulations. Presumably, some of the CR-pressurized gas buoyantly rises from the star-forming disk into the halo, a process that is suppressed by the stronger gravitational field in the high mass systems.

As a final analysis of our isolated disk simulations, we examine how well our simulation methodology for cosmic ray feedback converges when the numerical resolution is varied. We repeat one of the simulations with cosmic ray feedback ($\zeta_{\rm SN}$ = 0.1) of the 10^{11} $\rm M_{\odot}\mathit{h}^{-1}$ halo using a higher number of gas particles, namely 4×10^5 and 1.6×10^6, respectively. In Figure 4.13, we compare the resulting star formation rates. While there are some small fluctuations along with a variation of resulution, there is no clear systematic trend with resolution, and the results appear to be quite robust. In particular, the star formation rates for the simulations with 10^5 and 1.6×10^6 particles are in very good agreement with each other despite a variation of the mass resolution by a factor of 16. The oscillations are reproduced

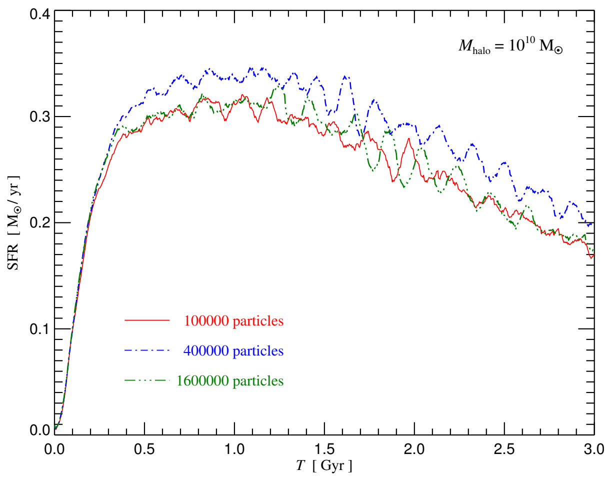

Figure 4.13.: Resolution study of the star formation rate during the formation of a galactic disk in a halo of mass 10^{10} M$_\odot h^{-1}$, including production of CRs with an efficiency of $\zeta_{SN} = 0.1$. We compare results computed with 10^5, 4×10^5, and 1.6×10^6 gas particles, respectively.

by all three resolutions, but they are not exactly in phase. Overall, the results of this resolution test are very promising and suggest that the numerical model is well posed and can be applied to cosmological simulations where the first generation of galaxies is typically only poorly resolved. We can still expect meaningful results under these conditions.

4.6.2. Cooling in isolated halos

The comparison of the maximum cosmic ray cooling timescale with the thermal cooling time in the right panel of Figure 4.4 shows that for a relatively wide temperature range, the lifetime of CRs is larger than the thermal cooling time. In a composite gas with a substantial cosmic ray pressure component, this could potentially help to stabilize the gas temporarily and reduce the rate of gas cooling and accumulating at the bottom of the potential well of a halo. Models have been conjectured where the temperature structure of the intracluster medium, with its characteristic observed minimum of one-third of the ambient cluster temperature, could be explained by a strong CR component in the intracluster medium Cen (2005).

In the following, we want to get an idea about the potential strength of this effect, and examine to this end a small set of toy simulations. We consider a series of self-similar dark matter halos with a gas component that is initially in hydrostatic equilibrium, just as before in Section 4.6.1. In fact, we use the same initial conditions as before, only replacing a fraction of the initial thermal pressure with cosmic ray pressure, while keeping the total pressure unchanged. We choose a spectral cut-off of $q = 1.685$ and a spectral index $\alpha = 2.5$ for the initial CR population and evolve the halos in time, including radiative cooling processes for the thermal gas as well as cosmic ray loss processes, while disregarding any sources of new cosmic ray populations. This way, we can find whether and how the cooling flows that develop

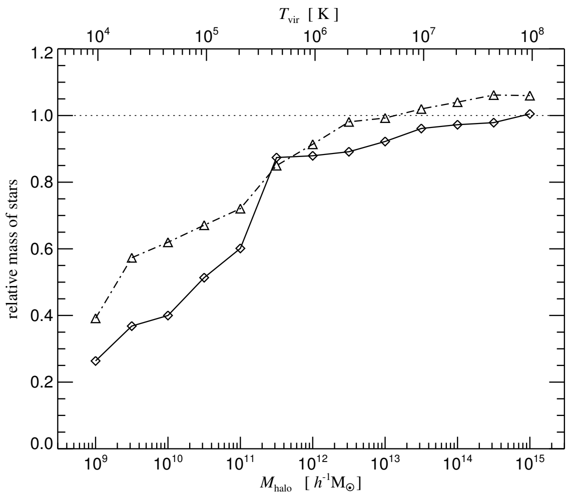

Figure 4.14.: Relative suppression of star formation in simulations of isolated halos when a fraction of 0.3 of the initial thermal pressure is replaced by a CR component of equal pressure. We show results as a function of halo virial mass for two different times after the simulations were started, for $t = 1.0\,$Gyr (solid line), and for $t = 3.0\,$Gyr (dot-dashed). For halos of low mass, the cosmic ray pressure contribution can delay the cooling in the halos.

in these halos are changed by the presence of the cosmic rays. Some studies have predicted cosmic ray pressure contributions of up to $\sim$ 50 per cent in clusters of galaxies (Miniati et al. 2001, Ryu et al. 2003). The fiducial test simulations presented here give a first indication of the size of the change of the cooling rates if these claims are indeed realistic.

In Figure 4.14, we show the results of the simulations as a function of halo mass, plotting the integrated star formation rate relative to an equivalent simulation without initial CR population. The cumulative star formation activity can be used as a proxy for the integrated strength of the cooling flow in the halo. It is seen that the total star formation for cluster halos of mass $10^{15}\,\mathrm{M}_{\odot}h^{-1}$ is essentially unchanged in the first $1-2\,$Gyr of evolution, while at late times, it is even slightly increased. For systems of significantly lower mass, the star formation rates are reduced in the CR case, by up to $\sim$ 40 per cent. This can be qualitatively understood based on a comparison of the thermal radiative cooling time with the CR dissipative cooling time. As the right panel of Fig. 4.4 shows, the timescales are comparable at the virial temperature corresponding to the $10^{15}\,\mathrm{M}_{\odot}h^{-1}$ halo, but are quite different for temperatures lower than that, where the radiative cooling is significantly faster. In fact, a naive comparison of these timescales might suggest an even stronger suppression of the cooling efficiency in systems of intermediate mass. Actually, the effect turns out to be a lot more moderate. This can be understood based on the softer equation of state of the CR component, combined with the fact that its cooling timescale typically declines faster than that of thermal gas when the composite gas is compressed. Hence, the ability of a CR pressure component to delay thermal collapse for a long time is quite limited, unless potential sources for the injection of new populations of CR particles are present.

4.7. Cosmological simulations

Previous simulation work on the effects of cosmic rays on structure formation has not accounted for the dynamical effects due to cosmic ray pressure, i.e. the effectiveness of cosmic ray production has only been estimated passively. Interestingly though, these works suggest that the cosmic ray production may be quite efficient, with up to $\sim$ 50% of the pressure being due to CRs (Miniati et al. 2001, Ryu et al. 2003, Ryu & Kang 2003, 2004). In the present work, se show the first self-consistent cosmological simulations of CR production that also account for the dynamical effects of cosmic rays. We study the global efficiency of cosmic ray production at structure formation shocks. Further, we investigate the influence of cosmic ray feedback on star formation in cosmological simulations, and on possible modifications of the Lyman-α forest, and finally the modification of the thermodynamic properties of the intracluster medium in high-resolution simulations of the formation of a cluster of galaxies.

4.7.1. Cosmic ray production in structure formation shocks

In this subsection, we examine the efficiency of cosmic ray production at structure formation shock waves. We use simulations that include cosmic ray injection at shocks and the cosmic ray loss processes (i.e. Coulomb cooling and hadronic losses), but disregard radiative cooling and star formation. The cosmological model we simulate is a concordance ΛCDM model with parameters ΛCDM model, with parameters $\Omega_0 = 0.3$, $\sigma_8 = 0.84$, baryon density $\Omega_b = 0.04$. We have picked a comoving box of side-length $L = 100\,h^{-1}$Mpc, and simulate each of our models at two resolutions, with 2×128^3 and 2×256^3 particles, respectively. The results of the two resolutions are in good agreement with each other, so we restrict ourselves to reporting the results of the higher resolution runs with 2×256^3 particles in the following.

We compare three simulations that differ in the treatment of the cosmic ray physics. In the 'full model', we account for shock injection self-consistently, i.e. we use the Mach number estimator of our companion study (Pfrommer et al. 2006) to determine the energy content and the slope of the proton populations accelerated at each shock front. This simulation hence represents our best estimate for the overall efficiency of the CR production process due to structure formation shocks. We contrast this simulation with a model where the CR injection has been artificially maximized by adopting a fixed efficiency $\zeta_{\rm inj} = 0.5$ and a fixed injection slope $\alpha = 2.5$ for *all shocks*. This high efficiency is normally only reached as limiting case for high Mach number shocks, so that this model also allows us to assess the importance of the dependence of the shock injection efficiency on Mach number. Finally, we compare these two models with a reference simulation where there is no cosmic ray physics included. This reference simulation is hence a standard non-radiative calculation where only shock-heating is included and the gas behaves adiabatically otherwise.

In Figure 4.15, we compare the time evolution of the mean mass-weighted temperature of the full cosmic ray model to that in the ordinary non-radiative simulation. We include a measurement of the mean energy in cosmic rays, converted to a fiducial temperature using the same factor that converts thermal energy per unit mass to temperature. Interestingly, at high redshift the cosmic ray energy content evolves

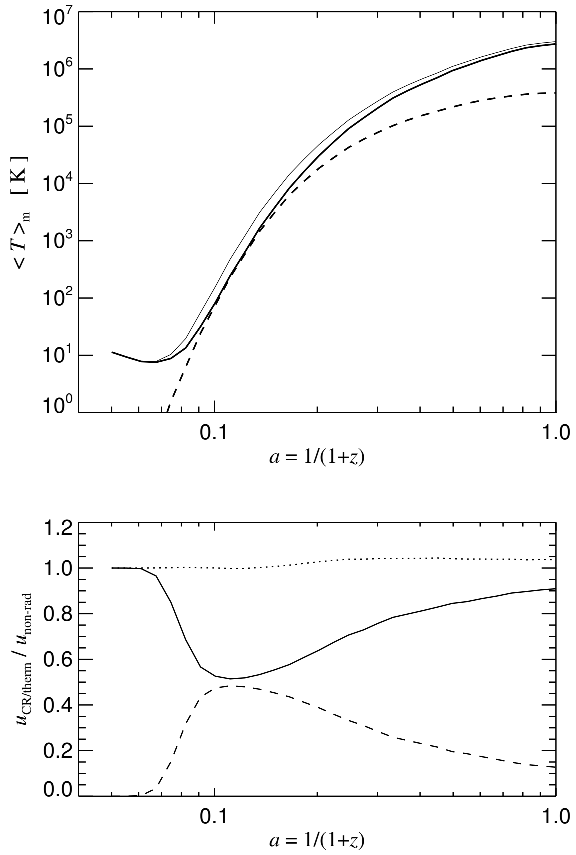

Figure 4.15.: Time evolution of the mean thermal energy and the cosmic ray energy content of the gas in non-radiative cosmological simulations. In the top panel, the solid thick line shows the mass-weighted temperature for a simulation where the efficiency of cosmic ray production at structure formation shocks is treated self-consistently based on our on-the-fly Mach number estimator. The dashed line is the corresponding mean cosmic ray energy, which we here converted to a fiducial mean temperature by applying the same factor that converts thermal energy per unit mass to temperature. For comparison, the thin solid line shows the evolution of the mean mass-weighted temperature in an ordinary non-radiative simulation without cosmic ray physics. In the bottom panel, we show the ratio of the mean thermal energy in the cosmic ray case relative to the energy in the simulation without cosmic rays (solid line), while the dashed line is the corresponding ratio for the cosmic ray component. Finally, the dotted line gives the total energy in the cosmic ray simulation relative to the ordinary simulation without cosmic rays.

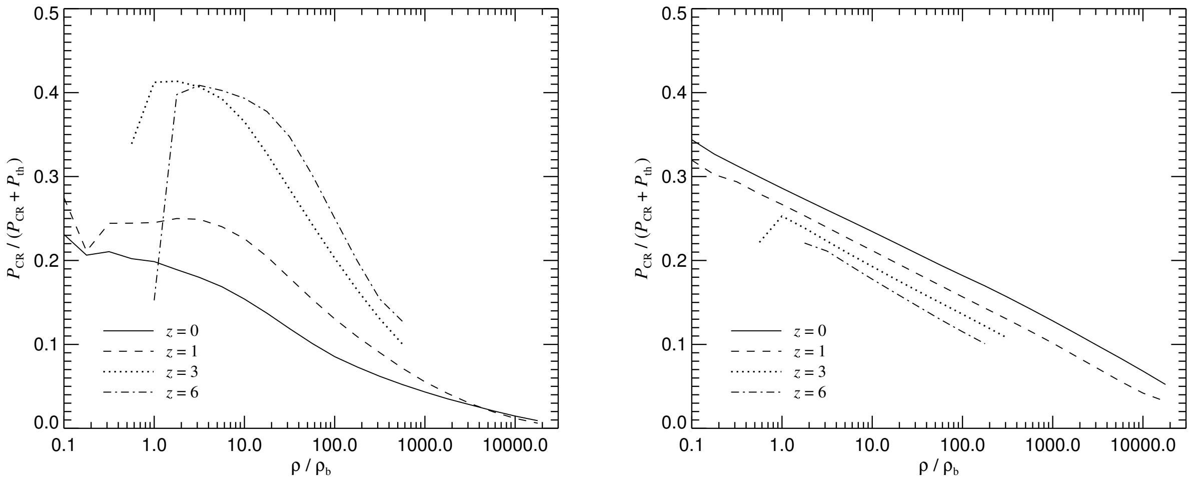

Figure 4.16.: Mean relative contribution of the cosmic ray pressure to the total pressure, as a function of gas overdensity in non-radiative cosmological simulations. We show measurements at epochs $z = 0$, 1, 3, and 6. The panel on the left gives our result for a simulation where the injection efficiency and slope of the injected cosmic ray spectrum are determined based on our on-the-fly Mach number estimation scheme. For comparison, the panel on the right shows the result for a simulation with a fixed injection efficiency $\zeta_{\rm lin} = 0.5$ and a soft spectral injection index of $\alpha_{\rm inj} = 2.9$. Clearly, the relative contribution of cosmic ray pressure becomes progressively smaller towards high densities. It is interesting that the trends with redshift are reversed in the two cases.

nearly in parallel to the thermal energy, and both are roughly half what is obtained in the simulation without cosmic rays. Apparently, the thermalization of gas is dominated by strong shocks which reach the asymptotic injection efficiency of 50 percent. At late times, however, the CR energy falls behind the thermal energy content, and the thermal energy in the CR simulation comes closer to the thermal energy in the original simulation without cosmic ray physics.

These trends become more explicit when the energy content in CRs and in the thermal reservoir of the full CR simulation is normalized to the thermal energy content of the reference simulation, as shown in the bottom panel of Figure 4.15. Around redshifts $z \sim 6 - 10$, the CR energy content nearly reaches the same value as the thermal energy in the full CR-model, and in addition, they are essentially equal to the thermal energy in the simulation without cosmic rays. With time passing, the relative importance of the cosmic rays declines, however, and the thermal energy in the full CR model slowly climbs back to the value obtained in the non-radiative reference simulation. At the same time, the sum of cosmic ray and thermal energy obtained in the full model grows to be a few percent higher at the end than that in the simulation without cosmic rays, despite the fact that in the CR simulation, some energy is lost to radiation via the hadronic decay channels. Apparently, the simulation with cosmic rays extracts slightly more energy from the gravitational potential wells of the dark matter. An explanation for this behaviour could be based on the fact that more energy needs to be invested into CRs to reach the same pressure in comparison to the thermal-only gas. This should allow the gas in CR simulations to sink deeper into

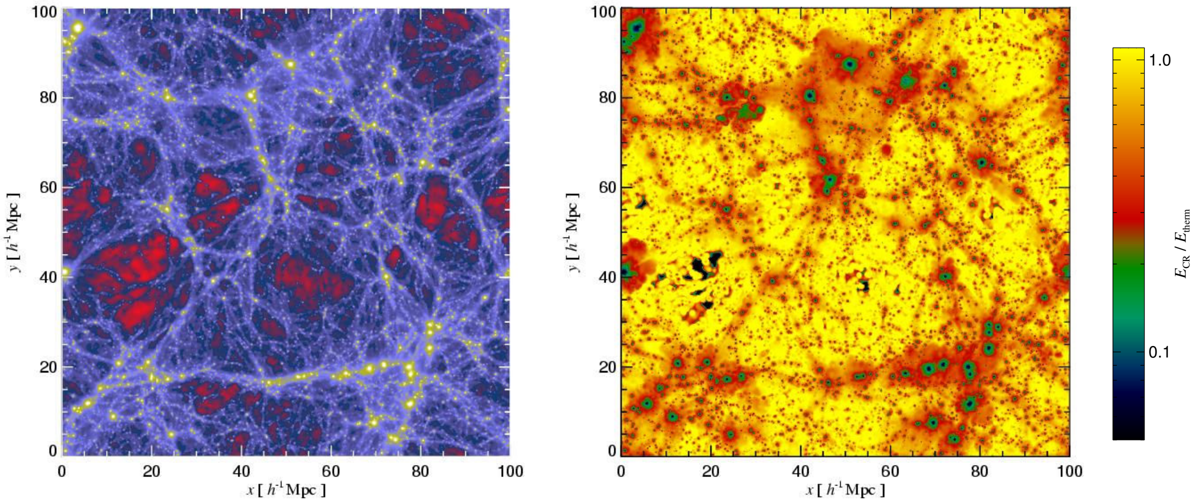

Figure 4.17.: Projected gas density field (left panel) in a slice of thickness 20 h^{-1}Mpc through a non-radiative cosmological simulation at $z = 0$. The simulation includes cosmic ray production at structure formation shocks using self-consistent efficiencies based on an on-the-fly Mach number estimation scheme. The panel on the right shows the ratio of the projected cosmic ray energy density to the projected thermal energy density. We clearly see that the local contribution of cosmic rays is largest in voids. It is also still large in the accretion regions around halos and filaments, but is lower deep inside virialized objects.

gravitational potential wells before stopped by shocks and pressure forces, such that more gravitational energy is liberated overall.

An interesting question arising is as to how the relative importance of cosmic rays depends on gas density. This is addressed by Figure 4.16, where we show the relative contribution of cosmic rays to the total gas pressure, as a function of baryonic overdensity, separately for different redshifts. We indicate results both for the simulation with self-consistent shock injection (left panel), and for the one using a constant injection efficiency (right panel). In general, the importance of cosmic rays is largest for densities in the regime of the mean cosmic density, and declines towards higher densities. This is consistent with expectations that the strongest shocks occur at low to moderate overdensities in the accretion regions around halos and filaments (Kang et al. 1996, Quilis et al. 1998, Miniati 2002, Ryu et al. 2003, Pfrommer et al. 2006), and also with the growing importance of cosmic ray loss processes at high densities. Another interesting trend found in our self-consistent simulation (the ‘full model) is that cosmic rays are particularly important at high redshift, with a gradual decline towards lower redshift, suggesting that the mean Mach number of shocks becomes lower at later times, as is indeed confirmed by studies of the cosmic Mach number distribution (Ryu et al. 2003, Pfrommer et al. 2006). This trend is reversed in our fiducial simulation with a fixed shock injection efficiency, where at all overdensities the relative importance of CRs grows with cosmic time. This emphasizes that a correct accounting of the shock strengths is highly important even at a qualitative level to correctly model the evolution of the cosmic ray pressure distribution. An implicit assumption we made in the above analysis is that weak magnetic fields are ubiquitous in the universe, even at low density. Whether they really exist and where they ultimately come from is left an open question however.

In Figure 4.17, we show the projected gas density field in a slice cut through the simulation box at $z = 0$. To highlight the relative importance of cosmic rays, the panel on the right shows the ratio of the projected cosmic ray energy density to the projected thermal energy density. The relative importance of CRs is clearly seen to be highest in the volume-filling gas at low density. In the accretion regions around halos and filaments, the CR contribution is still comparatively large, but the high-density regions inside massive halos are omitted, in agreement with the results of Figure 4.16. This raises the interesting question whether cosmic rays may perhaps modify the state of the intergalactic medium to the extent that the properties of Lyman-α absorption systems are modified. The latter arise primarily in gas that is largely unshocked, so that the effects might be weak even though the CR pressure contributions are predicted to be large on average at overdensities of a few. We shall pick up this question in Section 4.7.3.

Another interesting question is whether the bulk properties of halos are modified by the CR production at large-scale structure shocks. For example, we are interested in the question whether the concentration of gas in halos changes, which could manifest itself in a modification of the mean gas mass inside dark matter halos. To examine this question we compile halo catalogues for our simulations using a well-known Friends-of-Friends (FOF) algorithm with a standard linking-length of 0.2, and measure the virial radii and masses by means of the spherical overdensity algorithm. In Figure 4.18, we show the mean baryonic mass fraction in halos as a function of halo mass for the simulation with self-consistent CR injection and for the run without cosmic ray physics. In both cases, the baryonic fraction within the virial radius lies slightly below the universal baryon fraction, reaching $\sim 0.91 - 0.94$ of it, and for poorly resolved halos it drops a bit further. Such a depression of the universal baryon fraction is generally found in non-radiative SPH simulations (e.g Frenk et al. 1999). However, a comparison of the two simulations shows that the halos in the run featuring CRs show a systematic increase in their baryonic fraction, albeit by only about 1-2 per cent of the universal baryon fraction. This is consistent with expectations based on the higher compressibility of a composite gas containing thermal and CR components.

Using the group catalogues, we can further measure the mean cosmic ray energy content inside the virial radius of halos. In Figure 4.19, we show the ratio of cosmic ray to thermal energy as a function of halo mass. For the simulation with a constant fiducial shock injection efficiency of $\zeta_{\rm inj} = 0.5$ at *all shocks*, the ratio we find is ~ 0.2, independent of halo mass. Loss processes in the CR population and the shallower adiabatic index of the CR component reduce this value stronger than expected in this case for the post-shock region of a single shock where one would expect ~ 0.5. In the simulation featuring a self-consistent shock-strength dependent injection of CRs, we find an interesting mass dependence where the ratio of CR-to-thermal energy drops from about 0.2 for $10^{12}\,{\rm M}_\odot h^{-1}$ halos to ~ 0.05 for $10^{15}\,{\rm M}_\odot h^{-1}$ halos. Apparently, weaker shocks and adiabatic compression are comparatively more important for building up the thermal energy of clusters of galaxies than for galaxy-sized halos. We note that the value of $\sim 5 - 10\%$ we predict for the CR energy content due to structure formation shocks in clusters of galaxies is considerably lower than previous estimates Miniati et al. (2001). However, it is in good agreement with CR constraints from gamma ray and radio observations (Pfrommer & Enßlin 2003, 2004).

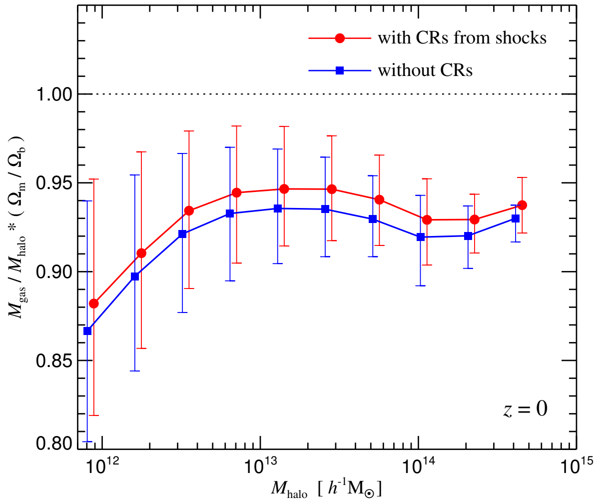

Figure 4.18.: Mean baryon fraction within the virial radius as a function of halo mass, normalized by the universal baryon fraction. We compare results for two non-radiative simulations, one with cosmic ray production by shocks, the other without cosmic ray physics. The bars show the 1σ scatter among the halos in each bin. When cosmic rays are included, the compressibility of the gas in halos becomes larger, leading to a slight increase of the enclosed baryon fraction.

4.7.2. Dwarf galaxy formation

We turn to studying the effects of cosmic ray feedback on galaxy formation in cosmological simulations. We have already found that small galaxies should be affected most. We expect small dwarf galaxies to be most susceptible to sizable effects of CR feedback from star formation. To obtain a reasonably good mass resolution, we simulate periodic boxes of side-length $10\,h^{-1}$Mpc, using 2×256^3 particles. This yields a mass resolution of $6.62 \times 10^5\,h^{-1}\mathrm{M}_\odot$ and $4.30 \times 10^6\,h^{-1}\mathrm{M}_\odot$ in the gas and dark matter, respectively. We limit ourselves to evolving the simulations to a redshift of $z = 3$, because at lower redshift the fundamental mode of the small simulation volume would start to evolve non-linearly, at which point the simulation as a whole could not be taken as representative for the universe any more. We are hence restricted to studying the high-redshift regime, but we expect that our results are indicative for the trends that would be seen in the dwarf galaxy population at lower redshifts as well, provided sufficiently well resolved simulations are available.

From identical initial conditions, we provide three sets of simulations, varying the scope and type of cosmic ray physics included. The first simulation is a reference run including only radiative cooling and star formation but no cosmic ray physics whatsoever. The second simulation is a model also considering cosmic ray production by the supernovae associated with star formation, at a constant efficiency of $\zeta_{\rm SN} = 0.35$. Finally, our third simulation is a model where we additionally included cosmic ray production by structure formation shocks, using the self-consistent efficiencies derived from our on-the-fly Mach

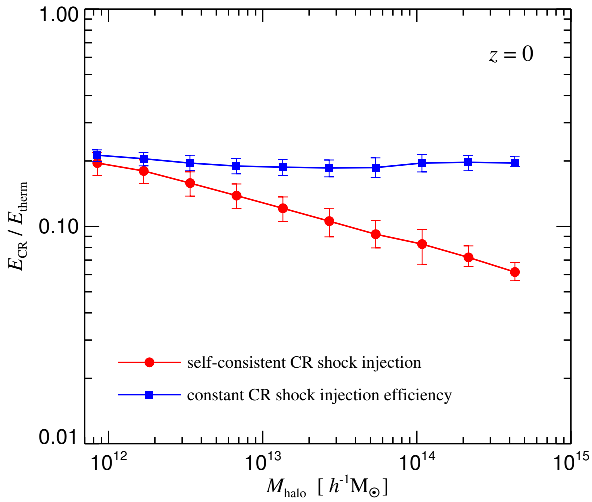

Figure 4.19.: Ratio of energy in cosmic rays to thermal energy within the virialized region of halos, shown as a function of halo mass. We compare results for two different non-radiative simulations, one treating the production of cosmic ray at shocks fronts using a self-consistent Mach number estimator, the other invoking a constant injection efficiency. The bars give the 1σ scatter among the halos in each bin. Interestingly, the self-consistent injection scheme predicts a lower CR energy content in more massive systems. In contrast, a constant shock injection efficiency produced no significant trend of the CR energy content with halo mass.

number estimation scheme. The latter simulation hence represents our best estimate for the total effect of cosmic rays on dwarf galaxy formation.

Figure 4.20 compares the cosmic star formation histories of the three simulations up to a redshift of $z \sim 2.9$. The inclusion of cosmic ray injection by supernovae leads to a significant reduction of the high redshift star formation activity, but the overall shape of the star formation history, in particular its exponential rise, is not changed to any significant degree. At high redshifts, the star formation rate is dominated by that occurring in small halos which are strongly affected by CR feedback, so this result is not unexpected given our previous findings. If CR production by structure formation shocks is included as well, the star formation is reduced further, although by a small factor only. This indicates that the cosmic ray pressure component injected into forming halos indeed tends to slightly reduce the cooling rates, consistently with the results we found for isolated halos. Towards redshift $z \sim 3$, the differences in the star formation rates gets noticeably smaller however, suggesting that the low redshift star formation histories differ at most by a small amount. Since the bulk of star formation shifts to that taking place in halos of ever larger mass scales at low redshift (Springel & Hernquist 2003b), this can be easily understood in terms of the smaller influence of CR feedback on large halos.

In order to make the effects of CR feedback on small halos more explicit, we again compile halo catalogues in the simulations using the mentioned group finder. Here, we are especially interested in how the efficiency of star formation changes by the inclusion of cosmic rays as a function of halo mass. In

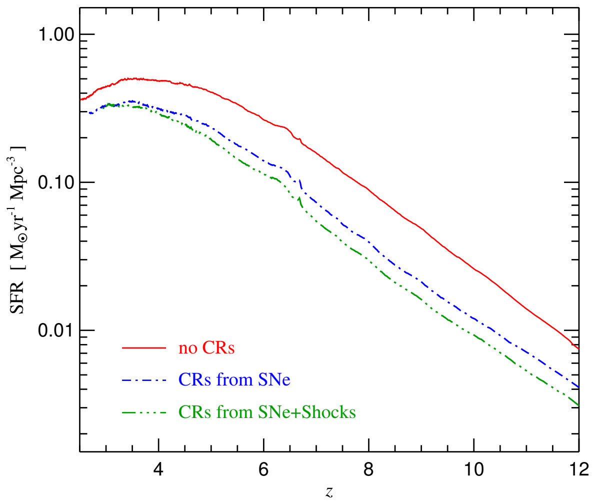

Figure 4.20.: Evolution of the cosmic star formation rate density in simulations of galaxy formation at high redshift. We compare results for three simulations that include different physics, a reference simulation without cosmic ray physics, a simulation with CR production by supernovae, and a third simulation which in addition accounts for CR acceleration at structure formation shocks with an efficiency that depends on the local Mach number.

the left panel of figure 4.21, we show the total-to-stellar mass ratios of these groups as a function of halo mass, both for the simulation with CR production by supernovae, and for the simulation without cosmic ray feedback. The simulation also featuring CR production by shocks shows quite similar behavior on this plot as the simulation that only accounts for CR from supernovae, and is therefore not shown. The symbols indicate the mean total-to-stellar mass ratio in small logarithmic mass bins, while the bars indicate the scatter by marking the central 68% percentile of the distribution of individual halos. The results show clearly that CRs signifficantly reduce star formation in low-mass halos, by factors of up to ≈ 10 for host halo masses of $\sim 10^{10}\mathrm{M}_{\odot}h^{-1}$ and below. In contrast, the amount of stars produced in massive halos is hardly changed at all. It is particularly interesting that the effect of CRs manifests itself in a gradual increase of the total-to-stellar mass ratio towards lower masses. This can be interpreted as a prediction for a steeply rising 'mass-to-light' ratio towards small halo masses, which is exactly what appears to be required to explain the observed luminosity function of galaxies in the ΛCDM concordance model. Here, we face the problem of the halo mass function increasing steeply towards low mass scales. For a near-constant mass-to-light ratio for low masses, as found in most simulations so far, this leads to a steeply rising faint end of the galaxy luminosity function, in conflict with observations. However, a steeply rising mean mass-to-light ratio for low mass halos could resolve this problem and provide a suitable 'translation' between the halo mass function and the galaxy luminosity function.

Conditional luminosity function analysis of the 2 Degree Field Galaxy Redshift Survey (2dFGRS) has shown (van den Bosch et al. 2003) that there appears to be a minimum in the observed mass-to-light ratio of galaxies around a halo mass of $\approx 3{\times}10^{11}\,\mathrm{M}_{\odot}h^{-1}$. This feature is reproduced surprisingly well in our

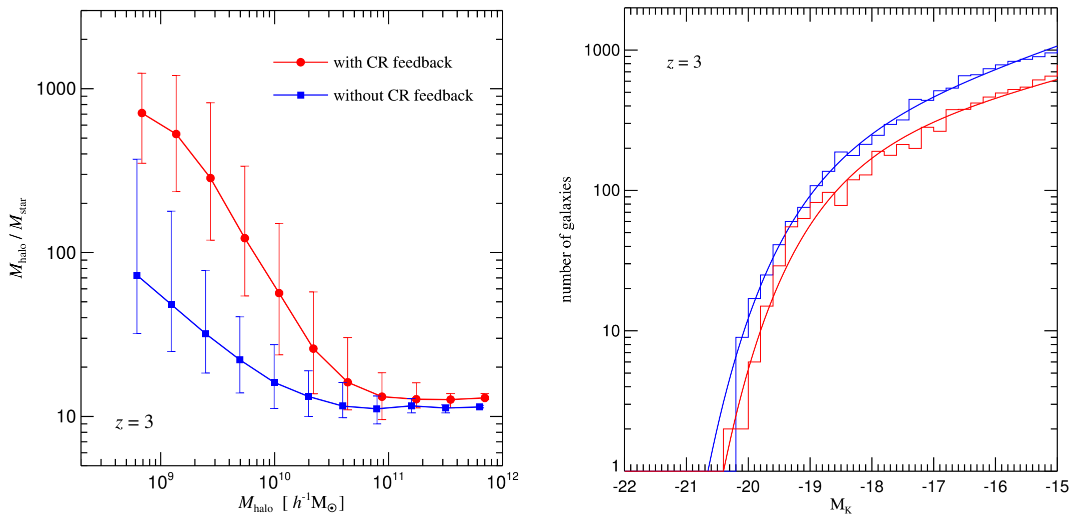

Figure 4.21.: Left panel: Comparison of the averaged total mass-to-light-ratio within the virial radius of halos formed in two high-resolution cosmological simulations up to $z = 3$. Both simulations follow radiative cooling and star formation, but one also includes CR-feedback in the form of cosmic production by supernovae, with an efficiency of $\zeta_{\rm SN} = 0.35$ and an injection slope of $\alpha_{\rm SN} = 2.4$. The bars indicate the scatter among halos in the logarithmic mass bins (68% of the objects lie within the range marked by the bars). Clearly, for halo masses below 10^{11} M$_\odot h^{-1}$, CR feedback progressively reduces the overall star formation efficiency in the halos. **Right panel:** The K-band galaxy luminosity functions at $z = 3$ in two high-resolution cosmological simulations. One of the simulations follows ordinary radiative cooling and star formation only (blue), the other additionally includes cosmic ray production by supernovae (red). The latter reduces the faint-end slope of the Schechter function fit (solid lines) to the data measured from the simulations (histograms). It is reduced from −1.15 to −1.10 in this case.

simulations, although even with CR feedback included, the rise of the stellar mass to light ratio towards low masses does not appear to be as sharp as their analysis would require.

However, one needs to keep in mind that the results as shown in the left panel of fig. 4.21 cannot be naively translated into changes of the faint-end slope of the luminosity function, as seen when directly comparing the K-band luminosity functions at $z = 3$. To determine those, we need to identify individual groups of stars as galaxies using a modification of the SUBFIND algorithm (Springel et al. 2001) for detecting bound substructures in halos. For each of the galaxies, we estimate magnitudes in standard observational band based on Bruzual & Charlot (2003) population synthesis models. In the right panel of figure 4.21, we compare the resulting restframe K-band luminosity functions at $z = 3$ for the simulations with CR feedback by supernovae and the simulation without any cosmic ray physics. We find that both luminosity functions are fit well by Schechter functions, with faint-end slopes of $\alpha = 1.15$ and $\alpha = 1.10$, respectively, for the cases without and with CR feedback. CRs only mildly reduce the faint-end slope despite their differential reduction of the star formation efficiency towards low mass scales. This result needs to be taken with a grain of salt though, as the faint-end slope could still be influenced by resolution effects in these simulations. A final assessment of the importance of CR feedback in the shaping the

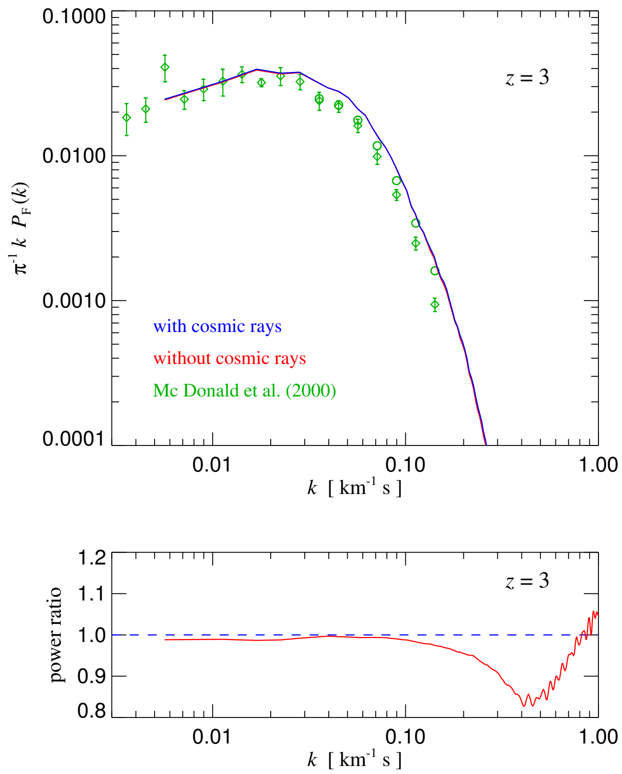

Figure 4.22.: Ly-α flux power spectrum (top) at $z = 3$ in simulations with and without cosmic ray production in structure formation shocks. The results lie essentially on top of each other, and only by plotting their ratio (bottom panel), it is revealed that there are small differences. In the simulation with cosmic rays, the power is suppressed by up to $\sim$ 15% on scales $0.1\,\mathrm{km}^{-1}\,\mathrm{s} < k < 0.7\,\mathrm{km}^{-1}\,\mathrm{s}$, while there is an excess on still smaller scales. However, on large scales $k < 0.1\,\mathrm{km}^{-1}\,\mathrm{s}$, which are the most relevant for determinations of the matter power spectrum from the Ly-α forest, the power spectrum is not changed by including CR physics. For comparison, we have also included observational data from McDonald et al. (2000) in the top panel (the open symbols are corrected by removing metal lines). A slightly warmer IGM in the simulations could account for the steeper thermal cut-off observed in the data.

faint-end of the galaxy luminosity function therefore will require future simulations with substantially increased resolution.

4.7.3. Cosmic ray effects on the intergalactic medium

As the Mach number distribution is dominated by strong shocks at high redshift, we expect that cosmic ray production is particularly efficient at early epochs and at the comparatively low densities where the strongest shocks occur, provided sufficient magnetization of the IGM existed to allow CR acceleration to operate. The thermalization time scales of cosmic rays are quite large at these low densities. Figure 4.16 shows that the mean energy content of cosmic rays can reach a sizable fraction of the thermal energy content at around redshift $z \sim 3$, suggesting a potentially important influence on the intergalactic medium at this epoch. Note however that in computing the results of Figure 4.16 we had neglected cosmic reionization, which will boost the thermal energy relative to the cosmic ray content. Also, large parts of the IGM at $z = 3$, particularly those responsible for the absorption seen in the Lyman-α forest, consist largely of unshocked material. Whether the Lyman-α forest might show any trace of the influence of cosmic rays is therefore an interesting and open question.

To investigate this question further, we have computed Ly-α absorption spectra for the cosmological simulations with $10\,h^{-1}$Mpc boxes analysed in the previous section. The two simulations we have picked both include radiative cooling, star formation, and heating by a spatially uniform UV background bases on a slightly modified Haardt & Madau (1996) model, with reionization at redshift $z = 6$. While one of the simulations does not account for any cosmic ray physics, the other one includes cosmic ray production by large-scale structure shocks and supernovae, as well as dissipative loss processes to the CR population.

For both simulations, we computed Lyman-α absorption spectra for 2048 lines of sight, in random directions parallel to the principal axes of the simulation boxes. By slightly adjusting the UV intensity, we have renormalized the spectra to the same mean transmission of $\langle\tau\rangle = 0.68$. A direct comparison of the spectra along the same lines-of-sight through the two simulations shows overall a perfect agreement, with very small residuals. This already indicates that any systematic difference between the simulations must be quite subtle, if present. To objectively quantify this, we have computed the average 1-d flux power spectra for the two cases and compare them in Figure 4.22. The top panel compares the two flux spectra directly with each other, and to observational data of McDonald et al. (2000). The results for the two simulations reside substantially on top of each other in this representation. The agreement with observational data is good, apart from a small excess of power on small scales, which can however be understood as a consequence of the too cool temperature of the IGM in our simulations compared with observations.

More interesting is perhaps an examination of the ratio of the flux power spectrum with cosmic rays to that without cosmic rays, as shown in the bottom panel of Figure 4.22. While for large-scale modes with $k < 0.1\,\mathrm{km^{-1}s}$, no noticeable differences are seen, there is a 5-15% reduction of power in the wave-length range $0.1\,\mathrm{km^{-1}s} < k < 0.7\,\mathrm{km^{-1}s}$, and at still smaller scales, the difference changes sign and turns into a growing excess of power in the CR simulation. These effects of CRs on the Ly-α therefore lie in a regime that is normally not used to constrain the matter power spectrum with Lyman-α forest data, at least in conservative treatments that focus on $k < 0.03\,\mathrm{km^{-1}s}$ (Viel et al. 2004). In general we find that the effects on the Lyman-α forest are very small and subtle; the forest goes through CR injection by large-scale structure shocks essentially unaltered, even though CRs contribute a sizable fraction to the mean energy content of the gas due to shock dissipation at densities at and around the mean density of the universe. Note that our simulations did not allow for a possible diffusion of CRs, but it seems unlikely that including this effect could change this conclusion.

4.7.4. Formation of clusters of galaxies

In this section, we study the influence of cosmic rays on individual halos formed in cosmological simulations in more detail. We focus on high-resolution ‘zoom’ simulations of the formation of a massive cluster of galaxies. These ‘zoom’ simulations are resimulations of an object identified within a cosmological structure in a simulation of structure formation simulation with large box-size. Once the object of interest has been selected, its particles are traced back through time to their originating location in the unperturbed initial conditions. The Lagrangian region of the cluster thus identified is then populated with an increased number of lower-mass particles particles, improving the local resolution somewhat, while in regions further away from the region of interest, the resolution is progressively degraded by using ever fewer, more massive particles to sample the cosmic matter content. This way, the computational effort can be concentrated to the object of interest, while at the same time the cosmological environment is still accounted for with satisfactory accurary during its formation.

We provide 6 resimulations of an individual cluster of galaxies, using different models for the physics of radiative cooling, star formation, and cosmic rays. The cluster is selected from a set of zoomed cosmological initial conditions originally constructed by Dolag et al. (2004a) and has a virial mass of $\approx 10^{14}\,\mathrm{M}_{\odot} h^{-1}$ at redshift $z = 0$. The gas particle mass is $1.6\times 10^{8}\,\mathrm{M}_{\odot} h^{-1}$ in the high resolution region, so the cluster is resolved with roughly 300000 gas and 300000 dark matter particles within its virial radius. The gravitational softening length for the simulations is constant in comoving units at redshifts $z \geq 5$, and after that held constant in physical units at a value of $5\,h^{-1}$kpc at lower redshifts.

The 6 simulations divide up into two groups of 3 simulations each. Those of the first group, do not include radiative cooling processes and star formation. Here a non-radiative (‘adiabatic’) simulation is used as a reference run, and compared to two simulations that both include cosmic ray production at large-scale structure formation shocks, one of them using the self-consistent Mach-number dependent injection efficiency, while the other assumes a fixed efficiency of $\zeta_{\mathrm{inj}} = 0.5$ with $\alpha_{\mathrm{inj}} = 2.5$ for all shocks. In essence, this set parallels the types of simulations analyzed in section 4.7.1. The second set of 3 simulations does incluse radiative cooling and star formation. Again, we consider one reference simulation without any cosmic ray physics whatsoever, and compare it to two simulations including cosmic rays. The latter two consist of one run with cosmic rays injected by supernovae associated with star formation alone (using $\zeta_{\mathrm{SN}} = 0.35$, and $\alpha_{\mathrm{SN}} = 2.4$), and another one accounting for cosmic rays produced at shock waves, as well. This second set of simulations corresponds to the types of simulations analyzed in section 4.7.2. In all simulations with cosmic rays, we assume a spectral index $\alpha = 2.5$ and include Coulomb cooling and hadronic losses for the CR populations.

Figure 4.23 compares spherically averaged radial profiles of pressure, temperature, and gas density for the three non-radiative simulations. For the pressure it shows the thermal pressure as well as that caused by cosmic rays for the two runs including cosmic ray physics. Interestingly, the contribution of the cosmic ray pressure component is substantially lower than that of the thermal one, even for the fiducial case of a constant shock injection efficiency of $\zeta_{\mathrm{inj}} = 0.5$ for all shocks. However, in this latter case thermal pressure is substantially elevated in comparison to the run omitting cosmic ray physics. This goes along with an increase of the gas density in the center regions, and a reduction of the thermal

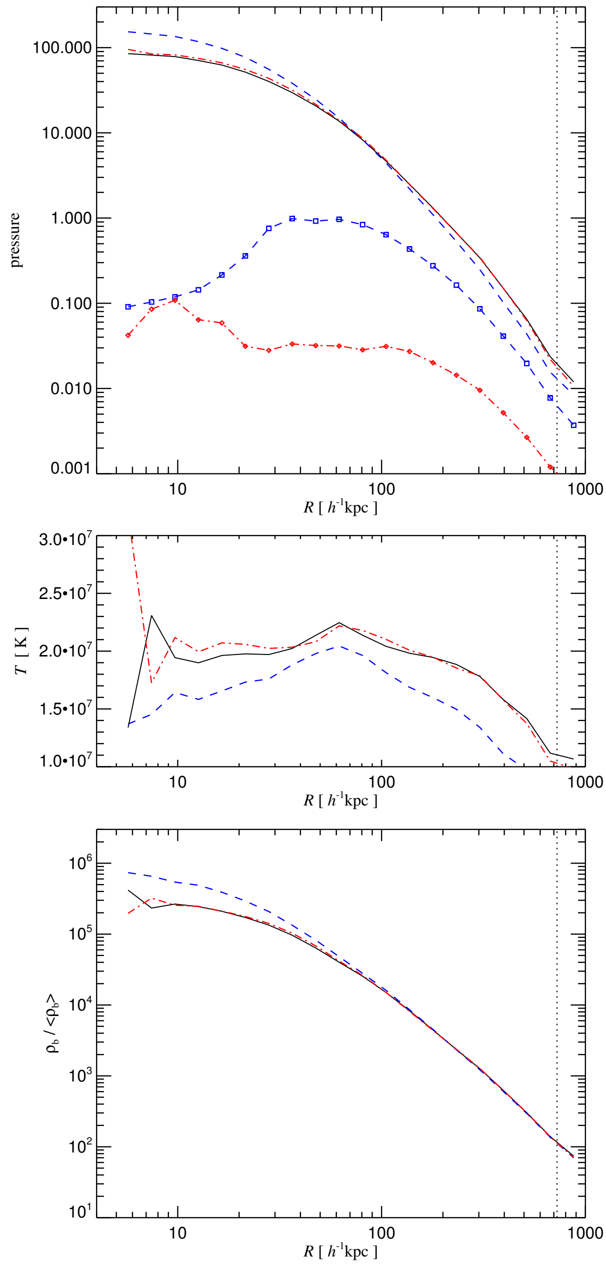

Figure 4.23.: Spherically averaged radial profiles of thermodynamic gas properties in three re-simulations of the same cluster of galaxies. All three simulations were not following radiative cooling and star formation, and the reference simulation shown with a solid line does not include any CR physics. However, the simulation shown with a dashed line accounted for CR production at structure formation shocks with a fixed efficiency ($\zeta_{\rm inj} = 0.5$, $\alpha_{\rm inj} = 2.9$) while for the simulation shown with dot-dashed lines, the shock injection efficiency was determined self-consistently based on our Mach number estimation scheme. The panel on top compares the thermal pressure in the three simulations. For the two simulations with cosmic rays, we additionally plot the CR-pressure, marked with symbols. The panel in the middle compares the gas temperature, while the panel on the bottom shows the radial run of the gas density. The vertical dotted line marks the virial radius of the cluster.

temperature throughout the entire volume of the cluster. This is the expected behaviour based on the higher compressibility of the gas in this case.

However, the cosmic ray pressure in the simulation featuring a self-consistent injection efficiency is substantially lower, and even at the virial radius it accounts for $\sim$ 10 percent of the thermal pressure at most, while in large portions of the center regions, $r \leq 100\,h^{-1}$kpc, the cosmic ray pressure contribution drops to the percent level and below. Obviously, cosmic ray injection by shocks is not efficient enough to fill much of the ICM with a dynamically significant cosmic ray pressure component, consistently with the results of Figure 4.19. In consequence, we find that in this case the profiles of gas density, temperature and thermal pressure are very similar to corresponding results for the simulation without cosmic ray physics.

Figure 4.24 shows the equivalent results for the radial profiles for the 3 simulations that include radiative cooling and star formation. Compared to the non-radiative calculations, the ICM has a markedly different structure. Due to the presence of a strong cooling flow, the temperature profile rises towards the centre, eventually droping sharply at around 20 kpc due to the onset of efficient cooling. The gas density gets significantly lower in the bulk of the cluster volume due to the large amount of cooled out gas, correspondingly, the total pressure dropping in large portions of the cluster volume. There are further interesting differences in the simulations with and without cosmic rays. Recall that both simulations include cosmic ray production by supernovae feedback, while only one of them accounted for cosmic ray injection by structure formation shocks. The contribution of CR pressure in both simulations is quite similar through most of the cluster, at a level of a few percent of the thermal pressure. In the very inner portions, where the gas drops out through cooling, the cosmic ray pressure rises sharply, even reaching and exceeding the thermal pressure. In this small region, thermal pressure is dissipated more rapidly than cosmic ray pressure.

Finally, in Figure 4.25 we compare the cumulative stellar profile of the cluster resulting from the three simulations that include radiative cooling and star formation. While the total mass of stars formed within the virial radius is reduced by the inclusion of cosmic ray feedback, the stellar mass in the central cluster galaxy is actually increased. The cluster cooling flow therefore slightly increases in strength, consistent with the results we find for isolated halos of this mass range. In contrast, the luminosity of the smaller galaxies orbiting the central structure of the cluster drops, in line with our finding that small galaxies experience a reduction of their star formation activity due to the CR feedback mechanisms. It seems clear however that our results do not suggest cosmic rays as a solution to the cooling flow problem in clusters of galaxies, at least not with the CR sources we have considered here. This conclusion could potentially change in interesting ways when CR production by AGN in clusters of galaxies is included as well (Churazov et al. 2001, Enßlin & Vogt 2006).

4.7.5. The influence of cosmic ray diffusion

In all of our previous results, we have ignored the effects of cosmic ray diffusion, largely because of the uncertainty involved in constraining an appropriate diffusivity. However, diffusion could potentially be

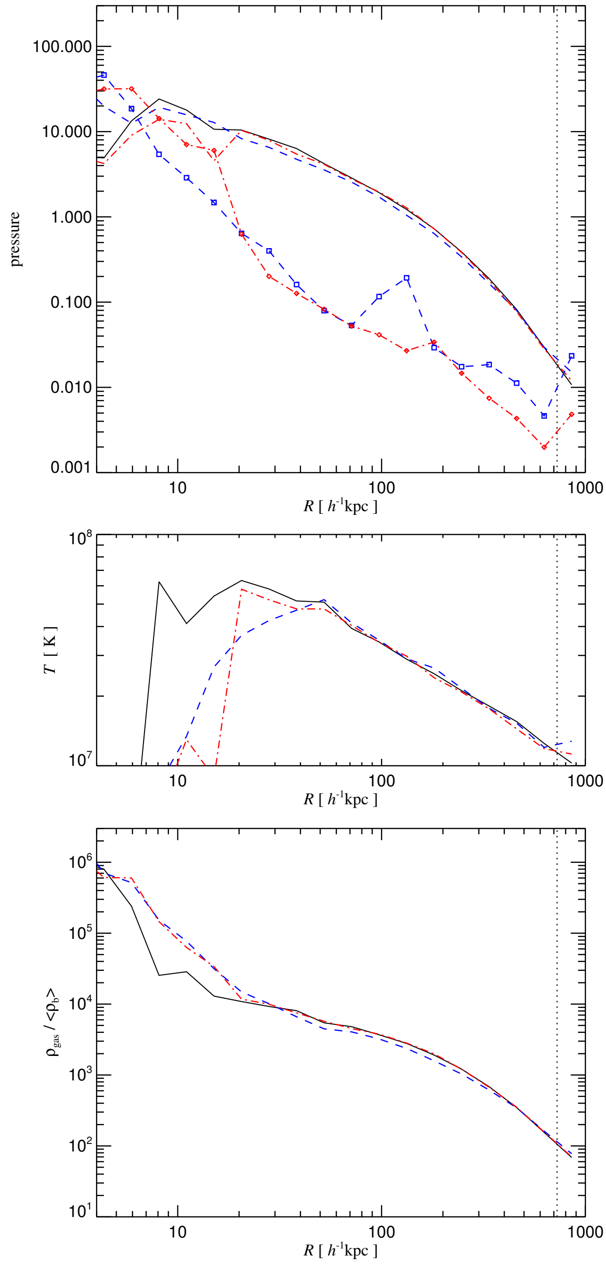

Figure 4.24.: Spherically averaged radial profiles of thermodynamic gas properties in three re-simulations of the same cluster of galaxies. All three simulations included radiative cooling of the gas, star formation and supernova feedback. The solid lines show the results of a reference simulation which did not include any cosmic ray physics. The other two simulations included CR production by supernovae, and the one shown with dot-dashed lines in addition accounted for CR injection at structure formation shocks, using self-consistent efficiencies based on our Mach number estimation scheme. The panel on top compares the thermal pressure in the three simulations. For the two simulations with cosmic rays, we additionally plot the CR-pressure marked with symbols. The panel in the middle compares the gas temperature for the three cases, and the panel on the bottom shows the radial run of the gas density.

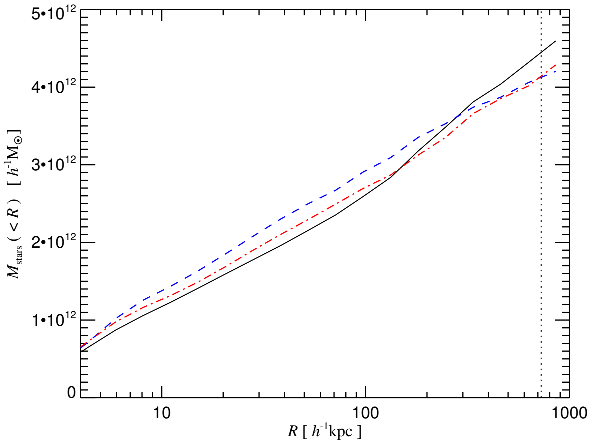

Figure 4.25.: Cumulative radial stellar mass profile in three re-simulations of the same cluster of galaxies. The simulations are the same ones also shown in Figure 4.24. The solid line gives the result for a reference simulation without CR physics, the dashed line includes CR production by supernovae, and the dot-dashed line additionally accounts for CR injection at structure formation shocks. The vertical dotted line marks the virial radius of the cluster.

important in several environments, depending of course on the details of the magnetic field structure and the strength of the resulting diffusivity. The present formalism implemented in the simulation code is capable of dealing with isotropic diffusion, yet in reality the diffusion is likely to be anisotropic, governed by the local magnetic field configuration. In principle, cosmological structure formation calculations with SPH are capable of following magneto-hydrodynamics (Dolag et al. 1999, 2005, Price & Monaghan 2004, 2005), although this is presently still fraught with numerical and physical difficulties. We therefore postpone a detailed analysis of the influence of cosmic ray diffusion to future work. Instead, we investigate a rather simple example, that shall give a first illustration of the effects to be expected from CR diffusion and imperfect containment of CRs in gas volume elements.

To this end, we repeat our simulations of isolated disk galaxy formation with CR injection by supernovae, but this time with diffusion included. A parameterized diffusivity as described in section 4.4 is employed, setting the values of the density and temperature scaling exponents to $n_T = 1/6$ and $n_\rho = -1/2$, respectively, with a baseline diffusivity of $\sim 10\,\mathrm{kpc^2 Gyr^{-1}}$ at the threshold for star formation, i.e. our diffusivity model is given by equation (4.54). The simulations to be re-evaluated are the ones considered in Section 4.6.1 with an injection efficiency of $\zeta_{\rm SN} = 0.3$ for the production of CRs by supernovae.

In Figure 4.26, we compare resulting star formation rates for halos of mass $10^9\,\mathrm{M_\odot} h^{-1}$ and $10^{10}\,\mathrm{M_\odot} h^{-1}$ as a function of time with the corresponding results of section 4.6.1 that did not account for diffusion effects. Interestingly, the oscillations due to the unstable dynamics of a cosmic ray dominated ISM are substantially suppressed when diffusion is included. This effect is quite prominent in the results for the $10^9\,\mathrm{M_\odot} h^{-1}$ halo, where now a nearly constant, quiescent star formation rate is observed. For the $10^{10}\,\mathrm{M_\odot} h^{-1}$ halo, the oscillations are only partially washed out and happen less frequently, but if they occur, they are stronger. Here the star formation rate of the galaxy develops a 'bursty' character.

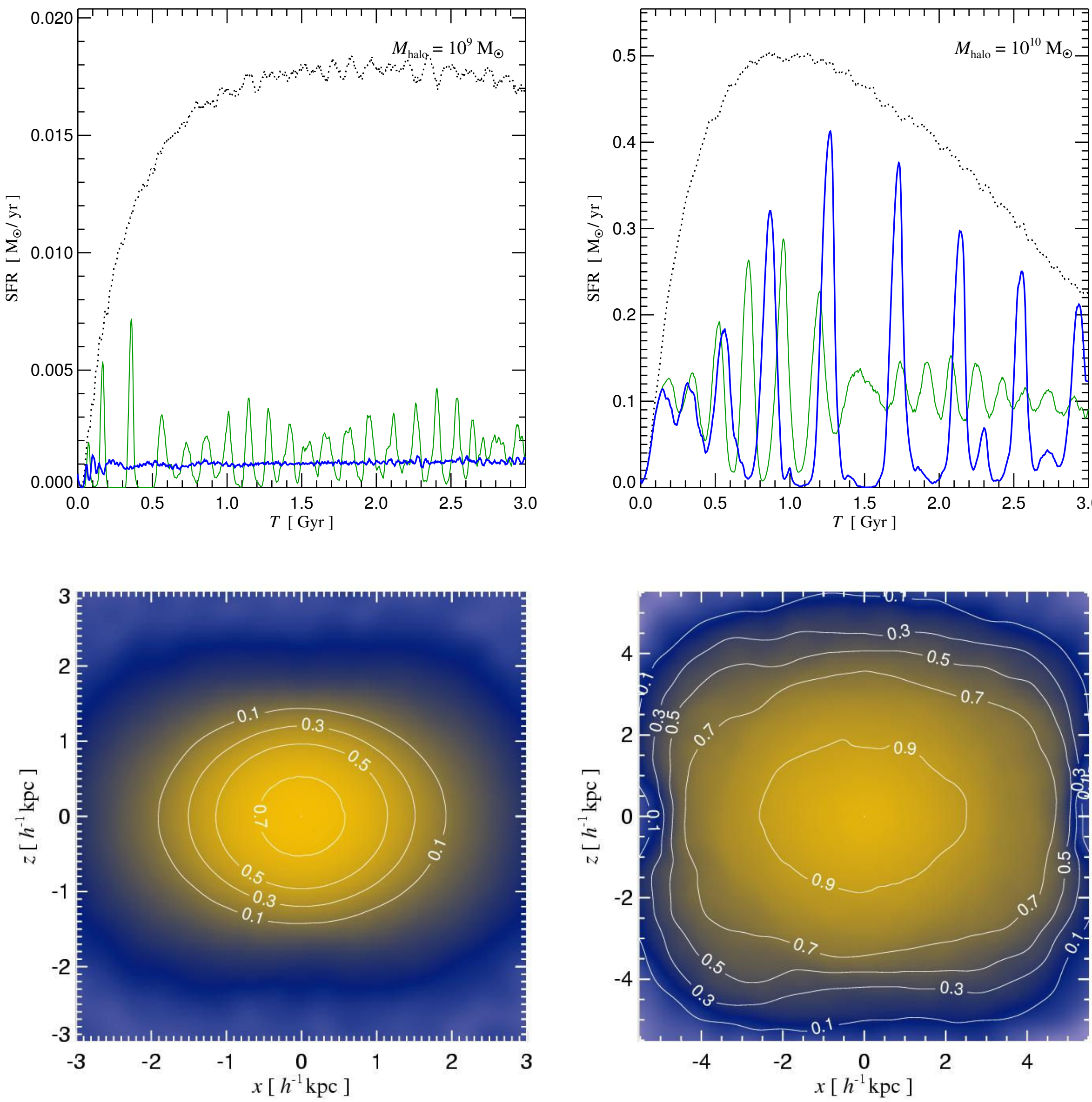

Figure 4.26.: Effects of cosmic ray diffusion on the star formation and the pressure distribution in isolated halos of mass $10^9\,M_\odot h^{-1}$ and $10^{10}\,M_\odot h^{-1}$. The panels on top compare the star formation rate when CR diffusion is included (thick blue line) to the case where it is neglected (thin green line). The dotted lines show the result when CR-production by supernovae is not included. In the bottom panels, we show projected gas density fields through the halos at time $t = 2.0\,$Gyr, with contours overlaid that give the fractional contribution of the projected CR energy to the total projected energy. These panels correspond directly to equivalent maps shown in Figure 4.11 for the case without CR diffusion.

Interestingly, diffusion actually reduces the integrated star formation still further; it drops by about 30% for the $10^9\,\mathrm{M}_{\odot}h^{-1}$ halo, and by 21% for the $10^{10}\,\mathrm{M}_{\odot}h^{-1}$ halo compared to the case without diffusion. Apparently, the cosmic rays that escape from the star-forming ISM into the less-dense gas in the halo are able to supply a partial pressure support that effectively reduces the rate at which gas sinks into the halo center and condenses, this way also countering the radiative cooling.

The more extended and smoother spatial distribution of cosmic rays due to diffusion can also be appreciated in the bottom panels of Figure 4.26, where we show projections of the gas density field with contours for the cosmic ray to thermal energy content overlaid. These panels directly correspond to the ones shown in Figure 4.11 for the case without diffusion. For halos of mass $10^{11}\,\mathrm{M}_{\odot}h^{-1}$ and more, diffusion with the parameters considered here has no significant impact on the dynamics. The progressively larger size of more massive systems makes it ever more difficult for diffusion to efficiently transport CR energy across the system.

4.8. Conclusions

In this chapter, we have presented the details of the first practical implementation of a simulation code capable of carrying out high-resolution simulations of cosmological structure formation with a self-consistent treatment of cosmic ray physics. In particular, the presented method takes dynamical effects of pressure forces due to cosmic rays into account and therefore allows for us to carry out studies of CR feedback in the context of galaxy formation. The underlying formalism for the treatment of cosmic rays, as discussed in more detail in (Enßlin et al. 2006) forms a compromise between the complexity of cosmic ray physics and the requirements of computational efficiency. In particular, we use a simplified spectral representation in terms of a power law for the momentum distribution with a low momentum cut-off. This allows for a rather significant simplification at the prize of a moderate loss of accuracy. As shown, the cosmic ray pressure is expected to be accurate to about 10 per cent in our model under steady state conditions. This is sufficiently accurate for our purposes given the other uncertainties and approximations involved.

The presented formalism also makes used of an on-the-fly shock detection scheme for SPH developed in a companion study (Pfrommer et al. 2006). This method allows for us to estimate Mach numbers in shocks captured during SPH simulations, such that we can use an appropriate efficiency for the CR injection at large-scale structure shock waves.

We have shown an initial analysis of principal effects of two sources of cosmic rays, namely CRs produced by supernova explosions, and by diffusive shock acceleration during structure formation. The loss processes we considered were Coloumb cooling and hadronic losses, which should be the most important ones in the described scenarios. If required, the modelling of these CR sink terms can be refined in future works within our methodology, and additional sources like cosmic rays from AGN can be added conveniently as well.

There are several noteworthy results derived from the cosmic ray treatment in this study. First of all, the simulations of galaxy formation with cosmic ray production by supernovae indicate that cosmic ray pressure can play an important role in regulating star formation in small galaxies. We find a significant reduction of the star formation rate compared to the one without CR physics, provided cosmic ray production efficiencies of several tens of percent are assumed. In small galaxies, the mean densities reached in the ISM remain sufficiently low such that the CR pressure can exceed the effective pressure produced by the thermal supernova feedback. Once this occurs, the gas of the ISM is ‘puffed up’, quenching the star formation rate. Due to the comparatively long cosmic ray dissipation timescale, the CR-pressure is retained for a sufficiently long time in these systems and has sizable impact on star formation rates. In massive galaxies, in constrast, the ISM grows to be so dense that the CR-pressure is unable to exceed the effective pressure predicted by the multi-phase model of Springel & Hernquist (2003a), so the star formation rates are not altered in these.

The effect on star formation also manifests itself in a reduction of the cosmic star formation rate density in cosmological simulations of galaxy formation. The SFR history is reduced at high redshift, where the bulk of star formation is dominated by small dwarf galaxies. As the bulk star formation shifts to the scale of more massive halos with lower redshift, the reduction fades progressively. An interesting implication of the strong effect of CR feedback on small galaxies is the reduction of the faint-end slope of the resulting galaxy luminosity function, an area that keeps posing a challenge for hydrodynamical simulations of galaxy formation within the ΛCDM scenario. We have indeed detected this flattening, although with a weak strength overall. Another tantalizing effect of cosmic rays is that they help to keep gas in small galaxies more diffuse. This should in principle help to alleviate the “angular momentum problem”; the problem of over-efficient angular momentum loss of gas to the dark matter caused by the early collapse of large amounts of gas in small halos. It is believed that it is a primary reason for present simulations to generally fail in producing large spiral galaxies at low redshift. Cosmic rays physics might help resolving this problem.

In simulations including cosmic ray injection by structure formation shocks, we find that CRs are produced efficiently at high redshifts when structure formation ensues, driven by the high Mach-number shocks found at low to moderate overdensities. At low redshifts on the other hand, most of the energy in weaker shocks where the injection efficiency is much smaller is thermalized. As a result, the mean energy content in cosmic rays can reach above 40% at redshifts of $z \simeq 5$, but drops to $\sim 10\%$ for lower redshift. The relative energy content also shows a strong density dependency. It is highest at low to moderate overdensities and declines continously with density, such that deep inside halos, only small fractions of cosmic ray energy produced by shock waves are retained. An important factor in this trend is the strong density dependence of cosmic ray loss processes, and the softer adiabatic index of CRs.

Therefore, when full cosmological simulations of the formation of galaxy clusters are considered, it is not surprising that we find that structure formation shocks build up only a rather small cosmic ray pressure contribution inside clusters. Even at the virial radius of these clusters, this contribution reaches only about 10%, but is even lower in the central portions of the clusters. When radiative cooling and cosmic ray production by supernovae are included, we find that supernovae can boost the mean CR energy density in the cluster, but the averaged contribution still remains at the percent level throughout the whole cluster volume, except for locations of rapidly cooling gas. Here, the CR pressure can temporarily dominate the pressure and delay the collapse for a short time. Nevertheless, we find that CR production by supernovae and structure formation shocks is unable to reduce central cluster cooling flows. Instead, we in fact detect a slight increase of the cooling in the simulated $10^{14}\,M_{\odot}h^{-1}$ cluster. This can be understood as a result of the higher compressibility of the cluster gas in the cosmic ray simulations, leading to an increased central concentration of gas and an elevated baryon fraction in the cluster, and hence higher overall cooling of gas in the centre. Note however that the currently discussed AGN feedback for quenching the cooling-flows is not included in the presented simulations. Still, we see the bulk of the cluster galaxies experience a reduction of their star formation rate when CR feedback is included, so the cluster galaxy luminosity function is expected to develop a shallower faint-end slope.

Overall, the presented results suggest that cosmic ray physics are unlikely to drastically modify the physics of galaxy formation in the ΛCDM model. However, cosmic rays help in areas where current model-building faces important problems, like for the faint-end slope of the galaxy luminosity function and the angular momentum problem. The presented formalism for treating CRs in cosmological simulations could therefore be very valuable for future studies on the role of cosmic rays in cosmological structure formation. In particular, it could be highly interesting to examine the effects of CRs on the metal distribution of the universe, or on the dynamics of buoyant bubbles inflated by AGN in clusters of galaxies. It will also be an important object of future work to provide an in-depth analysis of the role of cosmic ray diffusion.

The work and results presented in this chapter have been submitted to Astron. Astrophys. by M. Jubelgas, V. Springel, T. Enßlin and C. Pfrommer.

5
Conclusions

Today, we are still far from fully understanding of all the processes that lead to the formation of the galactic structures observed in the present universe. While there is a comparatively well developed picture for the gravitational clustering of dark matter and the general hierarchical structure formation scenario predicted for the leading ΛCDM cosmology, our understanding of the hydrodynamic processes relevant in galaxy formation is patchy at best. This is also reflected by today's state-of-the-art hydrodynamical simulations, which are rather limited in their ability to reproduce the observed properties of galaxies, or the thermodynamic profiles of clusters of galaxies, in detail.

These limitations originate in part from the finite numerical resolution that is imposed by the capabilities of today's computer technology. Another important restriction lies in our incomplete understanding of much of the relevant physics, which forces us to make strongly simplifying assumptions, which may not always be correct. But even as the resolution of new calculations progresses and the accuracy of physical assumptions advances, we may find that in order to really optimize the match of simulations and observations, additional physical processes that were previously neglected need to be included in the hydrodynamical simulations themselves. As the spatial and mass resolution of simulations reaches ever smaller scales, these new physical processes, which once seemed unimportant in coarse simulations, suddenly make a substantial difference in more sophisticated numerical models of galaxy formation. It is therefore an important task for theoretical work with simulations to make the simulation models more complete and faithful in the modelling of the underlying physics, allowing the construction of ever more faithful models of real galaxies on the computer.

In this work, I carried out research along these lines, trying to improve the currently available simulation methodology and to incorporate new, potentially important physical processes in it. To this end, I considered thermal conduction and cosmic ray physics, and implemented them in a modern cosmological code. I have shown that these processes do in fact have important implications for the structure and the properties of simulated galaxies and clusters of galaxies. In the following, I briefly summarize the main points of this work, and some of my principal findings.

I presented a new approach to include diffusive processes into the cosmological TreeSPH simulation code GADGET-2, focusing in particular on thermal conduction in hot astrophysical plasmas. The outlined scheme is manifestly conservative even when the time integration is done with individual and adaptive timesteps. I demonstrated the accuracy and robustness of the scheme with test calculations that involved thermal conduction in solids, and also introduced a method to reduce the impact of small-scale numerical noise on the convergence and robustness of the simulation results. Applying the thermal conduction code to models of galaxy clusters constructed with the structure of the analytical quasi-stable halo model of Zakamska & Narayan (2003), I verified the well-behaved nature of the conduction implementation in realistic scenarios and showed that halos with profiles according to the ZN model stay reasonably stable over prolonged periods, even in fully 3-dimensional numerical simulations. This shows that conduction can indeed offset a cooling flow in a cluster, provided the initial conditions have the ‘right’ structure.

I also carried out the first fully cosmological hydrodynamical simulations of cluster formation that included the effects of thermal conduction. These simulations showed that even for a conductivity as high as one third of the maximum Spitzer value, thermal conduction cannot alleviate the cooling flows in the cluster centers. Interestingly, the changes in the temperature and density profiles induced by conduction can instead even lead to an increased bolometric X-ray luminosity, implying a net increase of the total cooling rate, at least during certain periods of cluster evolution. Unlike in the specially set-up models of isolated galaxy clusters, the cosmological runs with conduction do not produce temperature profiles that induce a sizable heat flux from the cluster outskirts to the inner regions. Hence, it seems unlikely that thermal conduction will solve the disagreement between observations and current simulations with respect to cooling flows, all the more considering that magnetic fields inside clusters might well reduce the effective conductivity even more than we assumed. It is also interesting to note that in our simulations we did not find evidence for a conductive loss of energy from clusters to their surrounding intragalactic medium. However, both from the work presented here, and from the follow-up publication of Dolag et al. (2004a), it is obvious that thermal conduction still has large effects in modifying the thermodynamic state of the intracluster gas in rich clusters of galaxies, especially in the most massive systems due to the sensitive dependence of conductivity on gas temperature. In future works, the modelling of conduction should also be very interesting in simulations that try to resolve the small-scale dynamics within the star-forming interstellar medium.

In the second major part of this work, I introduced a numerical model for cosmic ray physics that for the first time allows cosmological simulations of structure formation that self-consistently account for the dynamical impact of cosmic ray pressure. To this end, in collaboration with Torsten Enßlin, Volker Springel, and Christoph Pfrommer, we developed a description of the relevant cosmic ray physics based on a simplified spectral model, which is parameterized with a prescribed power-law shape and low energy cut-off. The general formalism has been introduced by Enßlin et al. (2006), who also presented a generalized scheme that treats the spectral index of each individual gas mass element as variable as well. The implementation scheme I presented in this work is restricted to a globally fixed cosmic ray spectral index, which should provide a good approximation in the shown applications and help to reduce the complexity and computational cost of the simulation scheme.

I described the implementation of the scheme in detail, including several different CR source-, transfer-, and sink-terms, into the existing TreeSPH code framework GADGET-2. My implementation uses a number of optimizations like look-up tables and fast special-function solvers to produce good performance, while at the same its interface with the main parts of the GADGET-2 code is structured in a clear and easily extensible way.

With the new code, I surveyed the effects of cosmic-ray feedback in a number of different regimes of cosmic structure formation, and taking different CR sources into account. Perhaps the most obvious source of cosmic rays are supernova explosions that can release part of their energy as relativistic particles. Both in isolated, rotating gas clouds that collapse to form disk galaxies, and in full-blown cosmological simulations with high mass resolution, I found that in small halos with a shallow gravitational potential well the additional pressure induced by cosmic rays generated in supernova explosions effectively increases the feedback efficiency of star formation. This strongly suppresses the star formation rate in dwarf galaxies, an effect that becomes progressively weaker with growing halo mass. This is an important result, especially when considered in the cosmological context, because it suggests a profound impact on the faint-end of the galaxy luminosity function, where ordinary hydrodynamic simulations produce a substantial overabundance of low-luminosity galaxies. Cosmic ray physics may hence help to bring simulations into better agreement with observational data.

In simulations of galaxy cluster formation, I find that the CR pressure created by supernovae and structure formation shocks can lead to the build-up of a sizable population of non-thermal particles and a corresponding pressure component in the intracluster gas. When the gas cools, the CR pressure can temporarily supersede the thermal pressure and delay the collapse for a short time. However, no reduction in the strength of cluster cooling flows was observed. Actually, in one system, I even found a slight increase of the net cooling, most likely a result of the higher compressibility of a compound gas with thermal and CR components. The latter also leads to a slightly higher baryon fraction within the virial radius. Cosmic rays produced by shocks and supernovae alone seem unable to solve the "cooling flow problem". It is possible, however, that other CR source processes like AGN could still change this conclusion.

Taken together, these initial results for cosmic ray physics suggest that CRs might help to solve some important problems that current hydrodynamic simulations of structure formation face, but in general, the effects are small enough that the "big picture" of galaxy formation in the ΛCDM cosmology is not changed significantly. In the future, it will be interesting to refine the CR model by accounting for further source processes, in particular from AGN, and by extending our CR diffusion model to account for anisotropic transport in simulations that also follow magnetic fields.

I sincerely hope that the methods and results presented in this work will help in future progress in simulating galaxy formation. Despite all advances in the recent past, cosmology still offers challenges for decades to come. These unanswered questions should keep attracting further generations of scientists to this most fascinating field of physics.

Bibliography

Abadi M. G., Navarro J. F., Steinmetz M., Eke V. R., 2003, ApJ, 591, 499

Abu-Zayyad T., Belov K., Bird D. J., et al., 2001, ApJ, 557, 686

Aharonian F., Akhperjanian A. G., Bazer-Bachi A. R., et al., 2006, Nature, 439, 695

Aharonian F. A., Akhperjanian A. G., Aye K.-M., et al., 2004, Nature, 432, 75

Allen S. W., Schmidt R. W., Fabian A. C., 2001, MNRAS, 328, L37

Alpher R. A., Bethe H., Gamow G., 1948, Phys. Rev., 73, 803

Alpher R. A., Herman R. C., 1953, Ann. Rev. Nucl. Part. Sci., 2, 1

Balsara D. W., 1995, J. Comp. Phys., 121, 357

Barnes J., Hut P., 1986, Nature, 324, 446

Baugh C. M., Cole S., Frenk C. S., Lacey C. G., 1998, ApJ, 498, 504

Bell A. R., 1978a, MNRAS, 182, 147

Bell A. R., 1978b, MNRAS, 182, 443

Berezinskii V. S., Bulanov S. V., Dogiel V. A., Ptuskin V. S., 1990, Astrophysics of cosmic rays, Amsterdam: North-Holland, 1990, edited by Ginzburg, V.L.

Bieber J. W., Matthaeus W. H., 1997, ApJ, 485, 655

Black J. H., 1981, MNRAS, 197, 553

Bland-Hawthorn J., 1995, Proc. Astron. Soc. Australia, 12, 190

Blandford R. D., Ostriker J. P., 1978, Astrophys. J., 221, L29

Blanton M. R., Hogg D. W., Bahcall N. A., et al., 2003, ApJ, 592, 819

Borgani S., Murante G., Springel V., et al., 2004, MNRAS, 348, 1078

Bower R. G., Benson A. J., Lacey C. G., Baugh C. M., Cole S., Frenk C. S., 2001, MNRAS, 325, 497

Brookshaw L., 1985, Proceedings of the Astronomical Society of Australia, 6, 207

Brüggen M., 2003, ApJ, 593, 700

Bruzual G., Charlot S., 2003, MNRAS, 344, 1000

Bullock J. S., Dekel A., Kolatt T. S., et al., 2001, ApJ, 555, 240

Carilli C. L., Taylor G. B., 2002, ARA&A, 40, 319

Cen R., 1992, ApJS, 78, 341

Cen R., 2005, ApJ, 620, 191

Chandran B. D. G., Cowley S. C., 1998, Physical Review Letters, 80, 3077

Churazov E., Brüggen M., Kaiser C. R., Böhringer H., Forman W., 2001, ApJ, 554, 261

Ciardi B., Ferrara A., 2005, Space Science Reviews, 116, 625

Cleary P. W., Monaghan J. J., 1999, Journal of Computational Physics, 148, 227

Cole S., Lacey C. G., Baugh C. M., Frenk C. S., 2000, MNRAS, 319, 168

Cole S., Percival W. J., Peacock J. A., et al., 2005, MNRAS, 362, 505

Couchman H. M. P., Thomas P., Pearce F., 1995, ApJ, 452, 797

Cowie L. L., McKee C. F., 1977, ApJ, 211, 135

Cowie L. L., Songaila A., Kim T.-S., Hu E. M., 1995, AJ, 109, 1522

Croton D. J., Springel V., White S. D. M., et al., 2006, MNRAS, 365, 11

Dahlem M., Petr M. G., Lehnert M. D., Heckman T. M., Ehle M., 1997, A&A, 320, 731

Dalla Vecchia C., Bower R. G., Theuns T., Balogh M. L., Mazzotta P., Frenk C. S., 2004, MNRAS, 355, 995

Davé R., Dubinski J., Hernquist L., 1997, New Astronomy, 2, 277

Davé R., Hernquist L., Katz N., Weinberg D. H., 1999, ApJ, 511, 521

David L. P., Nulsen P. E. J., McNamara B. R., et al., 2001, ApJ, 557, 546

Di Matteo T., Springel V., Hernquist L., 2005, Nature, 433, 604

Dolag K., Bartelmann M., Lesch H., 1999, A&A, 348, 351

Dolag K., Grasso D., Springel V., Tkachev I., 2004a, Journal of Korean Astronomical Society, 37, 427

Dolag K., Grasso D., Springel V., Trachev I., 2005, in X-Ray and Radio Connections (eds. L.O. Sjouwerman and K.K Dyer) Published electronically by NRAO, http://www.aoc.nrao.edu/events/xraydio Held 3-6 February 2004 in Santa Fe, New Mexico, USA, (E8.10) 6 pages

Dolag K., Jubelgas M., Springel V., Borgani S., Rasia E., 2004b, ApJL, 606, L97

Drury L. O., Markiewicz W. J., Voelk H. J., 1989, A&A, 225, 179

Duffy P., Kirk J. G., Gallant Y. A., Dendy R. O., 1995, A&A, 302, L21+

Ellison S. L., Lewis G. F., Pettini M., Chaffee F. H., Irwin M. J., 1999, ApJ, 520, 456

Enßlin T. A., 2003, A&A, 399, 409

Enßlin T. A., Heinz S., 2001, A&A, 384, 27

Enßlin T. A., Pfrommer C., Springel V., Jubelgas M., 2006, submitted to A&A, preprint astro-ph/0603484

Enßlin T. A., Vogt C., 2006, A&A, 453, 447

Ettori S., Fabian A. C., 2000, MNRAS, 317, L57

Ettori S., Fabian A. C., Allen S. W., Johnstone R. M., 2002, MNRAS, 331, 635

Fabian A. C., 1994, ARA&A, 32, 277

Fabian A. C., Voigt L. M., Morris R. G., 2002, MNRAS, 335, L71

Fall S. M., Efstathiou G., 1980, MNRAS, 193, 189

Fermi E., 1949, Phys. Rev., 75, 1169

Fermi E., 1954, ApJ, 119, 1

Frenk C. S., White S. D. M., Bode P., et al., 1999, ApJ, 525, 554

Frenk C. S., White S. D. M., Bode P., et al., 1999, ApJ, 525, 554

Frye B., Broadhurst T., Benitez N., 2002, ApJ, 568, 558

Fujita Y., Suzuki T. K., Wada K., 2004, ApJ, 600, 650

Fukushige T., Ito T., Makino J., Ebisuzaki T., Sugimoto D., Umemura M., 1991, PASJ, 43, 841

Giacalone J., Jokipii J. R., 1999, ApJ, 520, 204

Gingold R. A., Monaghan J. J., 1977, MNRAS, 181, 375

Greisen K., 1966, Physical Review Letters, 16, 748

Haardt F., Madau P., 1996, ApJ, 461, 20

Heckman T. M., Dahlem M., Lehnert M. D., Fabbiano G., Gilmore D., Waller W. H., 1995, ApJ, 448, 98

Heckman T. M., Lehnert M. D., Strickland D. K., Armus L., 2000, ApJS, 129, 493

Heitmann K., Ricker P. M., Warren M. S., Habib S., 2005, ApJS, 160, 28

Hernquist L., 1993, ApJ, 404, 717

Hess V., 1912, Phys. Zeitschr., 13, 1084

Hubble E., 1929, Proceedings of the National Academy of Science, 15, 168

Hudson M. J., Smith R. J., Lucey J. R., Branchini E., 2004, MNRAS, 352, 61

Hut P., Makino J., 1999, Science, 283, 501

Johnstone R. M., Allen S. W., Fabian A. C., Sanders J. S., 2002, MNRAS, 336, 299

Jones T. W., Kang H., 1993, ApJ, 402, 560

Jubelgas M., Springel V., Dolag K., 2004, MNRAS, 351, 423

Kang H., Jones T. W., 1995, ApJ, 447, 944

Kang H., Jones T. W., 2006, Astroparticle Physics, 25, 246

Kang H., Ryu D., Jones T. W., 1996, ApJ, 456, 422

Katz N., Weinberg D. H., Hernquist L., 1996, ApJS, 105, 19

Kauffmann G., Colberg J. M., Diaferio A., White S. D. M., 1999, MNRAS, 303, 188

Kauffmann G., White S. D. M., Guiderdoni B., 1993, MNRAS, 264, 201

Kawai A., Fukushige T., Makino J., Taiji M., 2000, PASJ, 52, 659

Kay S. T., Pearce F. R., Frenk C. S., Jenkins A., 2002, MNRAS, 330, 113

Kennicutt R. C., 1989, ApJ, 344, 685

Kennicutt R. C., 1998, ApJ, 498, 541

Kim W., Narayan R., 2003, ApJ, 596, 889

Klypin A. A., Shandarin S. F., 1983, MNRAS, 204, 891

Lemaitre G., 1930, Bulletin of the Astronomical Institute of the Netherlands, 5, 273

Lewis G. F., Babul A., Katz N., Quinn T., Hernquist L., Weinberg D. H., 2000, ApJ, 536, 623

Lloyd-Davies E. J., Ponman T. J., Cannon D. B., 2000, MNRAS, 315, 689

Loeb A., 2002, New Astronomy, 7, 279

Loewenstein M., 2000, ApJ, 532, 17

Lucy L. B., 1977, AJ, 82, 1013

Mac Low M.-M., Ferrara A., 1999, ApJ, 513, 142

Makino J., 2000, in Dynamics of Star Clusters and the Milky Way, edited by S. Deiters, B. Fuchs, A. Just, R. Spurzem, R. Wielen, astro-ph/0007084

Makino J., Taiji M., Ebisuzaki T., Sugimoto D., 1997, ApJ, 480, 432

Malyshkin L., Kulsrud R., 2001, ApJ, 549, 402

Markevitch M., Ponman T. J., Nulsen P. E. J., et al., 2000, ApJ, 541, 542

Martin C. L., 1999, ApJ, 513, 156

McDonald P., Miralda-Escudé J., Rauch M., et al., 2000, ApJ, 543, 1

McKee C. F., Ostriker J. P., 1977, ApJ, 218, 148

Medvedev M. V., Melott A. L., Miller C., Horner D., 2003, preprint, astro-ph/0303310

Menci N., Cavaliere A., 2000, Bulletin of the American Astronomical Society, 32, 1200

Metzler C. A., Evrard A. E., 1994, ApJ, 437, 564

Miniati F., 2001, Computer Physics Communications, 141, 17

Miniati F., 2002, MNRAS, 337, 199

Miniati F., Ryu D., Kang H., Jones T. W., 2001, ApJ, 559, 59

Monaghan J. J., 1992, ARA&A, 30, 543

Monaghan J. J., 1997, J. Comp. Phys., 138/2, 298

Monaghan J. J., Gingold R. A., 1983, J. Comp. Phys., 52, 374

Monaghan J. J., Lattanzio J. C., 1985, A&A, 149, 135

Murali C., Katz N., Hernquist L., Weinberg D. H., Davé R., 2002, ApJ, 571, 1

Nagamine K., Springel V., Hernquist L., Machacek M., 2004, MNRAS, 350, 385

Nagano M., Watson A. A., 2000, Reviews of Modern Physics, 72, 689

Narayan R., Medvedev M. V., 2001, ApJL, 562, L129

Navarro J. F., Frenk C. S., White S. D. M., 1996, ApJ, 462, 563

Navarro J. F., Hayashi E., Power C., et al., 2004, MNRAS, 349, 1039

Peacock J. A., 1999, Cosmological physics, Cambridge University Press

Perlmutter S., Aldering G., Goldhaber G., et al., 1999, ApJ, 517, 565

Peters B., 1961, Nuovo Cimento, XXII, 800

Peterson J. R., Paerels F. B. S., Kaastra J. S., et al., 2001, A&A, 365, L104

Pfrommer C., Enßlin T. A., 2003, A&A, 407, L73

Pfrommer C., Enßlin T. A., 2004, A&A, 413, 17

Pfrommer C., Springel V., Enßlin T. A., Jubelgas M., 2006, MNRAS, 367, 113

Ponman T. J., Cannon D. B., Navarro J. F., 1999, Nature, 397, 135

Power C., Navarro J. F., Jenkins A., et al., 2003, MNRAS, 338, 14

Price D. J., Monaghan J. J., 2004, MNRAS, 348, 139

Price D. J., Monaghan J. J., 2005, MNRAS, 364, 384

Quilis V., Ibanez J. M. A., Saez D., 1998, ApJ, 502, 518

Rechester A., Rosenbluth M., 1978, Phys. Rev. Lett., 40, 38

Riess A. G., Filippenko A. V., Challis P., et al., 1998, AJ, 116, 1009

Rudaz S., Stecker F. W., 1988, ApJ, 325, 16

Ryu D., Kang H., 2003, Journal of Korean Astronomical Society, 36, 105

Ryu D., Kang H., 2004, Journal of Korean Astronomical Society, 37, 477

Ryu D., Kang H., Hallman E., Jones T. W., 2003, ApJ, 593, 599

Sarazin C. L., 1988, X-ray emission from clusters of galaxies, Cambridge Astrophysics Series, Cambridge: Cambridge University Press, 1988

Scannapieco E., Thacker R. J., Davis M., 2001, ApJ, 557, 605

Schlickeiser R., 2002, Cosmic ray astrophysics, Astronomy and Astrophysics Library, Springer, Berlin

Seljak U., Makarov A., McDonald P., et al., 2005, Phys. Rev. D, 71, 10, 103515

Shapiro P. R., Martel H., Villumsen J. V., Owen J. M., 1996, ApJS, 103, 269

Sijacki D., Springel V., 2006, MNRAS, 366, 397

Soker N., 2003, MNRAS, 342, 463

Somerville R. S., Primack J. R., 1999, MNRAS, 310, 1087

Spergel D. N., Bean R., Dore' O., et al., 2006, ArXiv Astrophysics e-prints

Spergel D. N., Verde L., Peiris H. V., et al., 2003, ApJS, 148, 175

Spitzer L., 1962, Physics of Fully Ionized Gases, Physics of Fully Ionized Gases, New York: Interscience (2nd edition), 1962

Springel V., 2005, MNRAS, 364, 1105

Springel V., Di Matteo T., Hernquist L., 2005a, MNRAS, 361, 776

Springel V., Hernquist L., 2002, MNRAS, 333, 649

Springel V., Hernquist L., 2003a, MNRAS, 339, 289

Springel V., Hernquist L., 2003b, MNRAS, 339, 312

Springel V., White S. D. M., Jenkins A., et al., 2005b, Nature, 435, 629

Springel V., White S. D. M., Tormen B., Kauffmann G., 2001, MNRAS, 328, 726

Springel V., Yoshida N., White S. D. M., 2001, New Astronomy, 6, 79

Stoehr F., White S. D. M., Springel V., Tormen G., Yoshida N., 2003, MNRAS, 345, 1313

Tabor G., Binney J., 1993, MNRAS, 263, 323

Tegmark M., Blanton M. R., Strauss M. A., et al., 2004, ApJ, 606, 702

Thomas P. A., Couchman H. M. P., 1992, MNRAS, 257, 11

Tormen G., Bouchet F. R., White S. D. M., 1997, MNRAS, 286, 865

Tornatore L., Borgani S., Springel V., Matteucci F., Menci N., Murante G., 2003, MNRAS, 342, 1025

Ullio P., Bergström L., Edsjö J., Lacey C., 2002, Phys. Rev. D, 66, 12, 123502

van den Bosch F. C., 2002, MNRAS, 332, 456

van den Bosch F. C., Yang X., Mo H. J., 2003, MNRAS, 340, 771

Viel M., Haehnelt M. G., Springel V., 2004, MNRAS, 354, 684

Vikhlinin A., Markevitch M., Murray S. S., 2001, ApJ, 551, 160

Vogt C., Enßlin T. A., 2003, A&A, 412, 373

Voigt L. M., Fabian A. C., 2004, MNRAS, 347, 1130

Voigt L. M., Schmidt R. W., Fabian A. C., Allen S. W., Johnstone R. M., 2002, MNRAS, 335, L7

Voit G. M., Bryan G. L., Balogh M. L., Bower R. G., 2002, ApJ, 576, 601

White S. D. M., 1996, in Cosmology and Large-Scale Structure, edited by R. Schaeffer, J. Silk, M. Spiro, J. Zinn-Justin, 395, Elsevier, Dordrecht

White S. D. M., Frenk C. S., 1991, ApJ, 379, 52

White S. D. M., Narayan R., 1987, MNRAS, 229, 103

White S. D. M., Rees M. J., 1978, MNRAS, 183, 341

Wiebel-Sooth B., Biermann P. L., 1999, Landolt-Bœrnstein, vol. VI/3c, Springer Verlag

Willick J. A., Strauss M. A., Dekel A., Kolatt T., 1997, ApJ, 486, 629

Wu K. K. S., Fabian A. C., Nulsen P. E. J., 2000, MNRAS, 318, 889

Wu X., Xue Y., 2002, ApJL, 572, L19

York D. G., et al., 2000, Astron. J., 120, 1579

Zakamska N. L., Narayan R., 2003, ApJ, 582, 162

Zatsepin G. T., Kuzmin V. A., 1966, Pis'ma Zh. Eksp. Theor. Fiz., 4, 116

Begegnet uns jemand, der uns Dank
schuldig ist, gleich fällt es uns ein.
Wie oft können wir jemandem begegnen,
dem wir Dank schuldig sind, ohne daran zu denken!

Johann Wolfgang von Goethe

Danksagungen

Vielen Dank an Simon White und Volker Springel, die es mir ermöglicht haben, meine Promotion am MPA durchzuführen und mich nach Kräften bei dieser unterstützt haben. Mit viel Einsatz, guten Ideen und richtigen Worten hat Volker unsere Projekte immer wieder voran gebracht und mich vor so mancher (numerischer) Falle bewahrt oder aus ihr gerettet. Er erklärte mir mit endloser Geduld auch die komplexesten Module unseres Simulationscodes, und lenkte mein Augenmerk auf die für meine Arbeit wichtigsten Punkte. Er war für mich und meine Nöte immer erreichbar, nicht einmal auf Seminar-Reisen gönnte er sich Ruhe vor mir.

Ich danke den Kollegen, mit denen ich an meinen Projekten arbeiten durfte, Klaus Dolag, Torsten Enßlin und Christoph Pfrommer. Die Zusammenarbeit mit ihnen war für mich ein sehr schöner Aspekt meiner Arbeit am MPA, und aus unseren gemeinsamen Planungen und Diskussionen habe ich immer Motivation und neue, interessante Denkansätze mitgenommen.

Sehr herzlich will ich mich bei all denen bedanken, die meinen Weg am MPA begleitet haben, und diesen oft durch tausend Kleinigkeiten zu einer schönen und auch spaßigen Zeit gemacht haben, und die mir mit dieser untrennbar in Erinnerung bleiben werden. Stellvertretend, aber nich ausschließlich danke ich hier Leonhard Scheck für wahre Farbzauber und gemeinsames Gedenken an die Opfer von 1705, Kate O'Shea für konsequentes Überwachen meiner korrekten Sitzhaltung, Almudena Arcones für ihre (vergeblichen) pädagogischen Anstrengungen, Björn Schäfer für seine ansteckende Euphorie für einen ganz bestimmten Rechnertyp, Maria Depner für bedingungsloses Lächeln und Max Brandl für gute Laune schon am frühen Morgen.

Norbert Grüner, Bernt Christiandl, Hans-Werner Paulsen und Manfred Reuter danke ich für ihre wertvolle Arbeit hinter den Kulissen des Instituts. Ihr Engagement und ihre freundliche Art helfen über so manche Probleme hinweg und tragen so zu der tollen Arbeitsumgebung des MPA bei. Herzlichen Dank auch an Christian Guggenberger, für seinen unermüdlichen Einsatz am Infiniband des Opteron-Clusters, durch den ich hier einen großen Teil meiner Rechnungen durchführen konnte.

Ein herzliches Dankeschön an Alex Wichert, dafür, mir die Angst vorm Schreiben zu nehmen und für viele Gespräche die ich nicht missen will. Ich hoffe, ich werde jetzt die Zeit finden, das neue Buch endlich zu lesen.

Vielen Dank auch an all diejenigen, die mich während meiner Arbeit bei Laune gehalten haben und meine Launen ertragen haben. Ob mit Science Fiction oder Doppelkopf, ob Schulstraße oder Paris. Vor allem möchte ich hier meiner Familie und meiner Lebensgefährtin Claudia Ganslmeier danken, die meine Höhen und Tiefen wohl am stärksten abbekommen und abgefedert haben. Ihre Stärke hat mich ein gutes Stück des Weges zu dieser Arbeit mitgetragen. Danke auch an Felix Stöhr, Sina Lohmann, Thomas Schmid, an Alex Hentschel und Ingo Pflanz. Mit Freunden wie ihnen ist mir für die Zukunft nicht bange.

Curriculum Vitae

Personal Data

Name:	Martin Jubelgas
Born:	December 03, 1975 in Munich
Nationality:	German

Education

1982 - 1986	Grundschule Kirchheim II
1986 - 1992	Gymnasium Kirchheim b. München
1992 - 1995	Luitpold-Gymnasium Wasserburg a. Inn
Jun. 1995	Abitur at Luitpold-Gymnasium Wasserburg a. Inn

Academic Record

Nov. 1996 - Aug. 2002	study of general ghysics at Technische Universität München (TUM)
Sept. 2001 - Aug. 2002	diploma thesis at Max-Planck-Institut für Astronomie, Garching (MPA) *Galactic Winds and the Formation of Galaxies*
Aug. 2002	diploma in physics at TUM
Sept. 2002 - Okt. 2005	PhD student at Ludwig-Maximilians-Universität München and MPA

Professional Record

Nov. 2005 - March 2006	patent attourney candidate (Müller-Bore & Partner)
since April 2006	system- and software-engineer (ESG)

Zusammenfassung der Dissertation

Cosmological Hydrodynamics: Thermal Conduction and Cosmic Rays

Martin Jubelgas

Hydrodynamische Simulationen haben sich in den letzten Jahren zu einem wichtigen Werkzeug in der Kosmologie entwickelt. Es ist Ziel dieser Arbeit, einen bestehenden Simulationscode durch weitere physikalische Effekte zu erweitern, um deren Auswirkungen in selbst-konsistenter Art und Weise untersuchen zu können. Es wird ein Formalismus vorgestellt, der die Wärmeleitung in einem heißen, diffusen Plasma nachgebildet. Ferner präsentiere ich eine neuartige Methode, kosmische Teilchenstrahlung durch ein als einfach parametrisiert angenommenes Impulsspektrum der Strahlungsteilchen in hydrodynamischen Simulationen mitsamt ihren dynamischen Effekten zu berücksichtigen und untersuchen.

Es zeigt sich in durchgeführten Simulationen, daß die Wärmeleitung, obwohl sie unter bestimmten Umständen ie Kühleffekte ausgleichen kann, in den durchgeführten kosmologischen Simulationen nicht zu einer Reduzierung der Akkretionsrate in Galaxienhaufen führte. Es zeigen sich dennoch in Temperatur- und Strahlungsprofilen der simulierten Objekte starke Auswirkungen der Wärmeleitung.

Die kosmische Teilchenstrahlung zeigt in weiteren Simulationen deutliche Auswirkungen auf die Evolution von Strukturen, insbesondere bei der Regulierung von Sternentstehung in kleinen Galaxien (solchen mit Virialgeschwindigkeiten von unter $\sim 80\mathrm{km\,s^{-1}}$). Hier führt sie zu einer staken Unterdrückung der Sternenbildung, in zunehmendem Maße für kleinere Galaxien mit einer geringeren Gesamtmasse. Durch diese Unterdrückung wird bei statistischer Betrachtung auch die Steigung der Leuchtkrafts-Verteilungfunktion von Galaxien an ihrem leuchtschwachen Ende stark beeinflußt; letztere wird deutlich flacher und bringt Simulationsergebnisse somit merklich näher an beobachtete Werte.